IFT
Instituto de Física Teórica
Universidade Estadual Paulista

TESE DE DOUTORAMENTO IFT–T.011/12

Busca por Ressonâncias de Grávitons em Modelos com Dimensões Extras no LHC

Flavia de Almeida Dias

Orientador

Sérgio Ferraz Novaes

Novembro de 2012

IFT

Instituto de Física Teórica
Universidade Estadual Paulista

TESE DE DOUTORAMENTO IFT–T.011/12

Search for Graviton Resonances of Extra Dimension Models at LHC

Flavia de Almeida Dias

Supervisor

Sérgio Ferraz Novaes

November 2012

Dedico esse trabalho aos meus pais,
Renato de Almeida Dias e
Maria Regina Candido de Almeida Dias

Acknowledgements

Agradeço aos meus pais, Regina e Renato, e a minha família, por tudo.

Agradeço ao meu orientador, Sérgio Novaes, por todo o apoio nessa jornada.

I would like to thank my CERN advisor, Maria Spiropulu, for the guidance and support.

I would like to thank Christos Leonidopoulos, for teaching me a lot of what I know about being an experimental physicist.

I would like to thank Maurizio Pierini, for all the bright ideas and help during all these years.

Agradeço ao Thiago Tomei, por ter sido amigo, colega de trabalho, e me ensinado o caminho das pedras.

I would like to thank Bryan Dahmes, for all the help and support when I freaked out.

I would like to thank Cory Fantasia and Piotr Traczyk, for giving me the pleasure of being my co-workers.

Agradeço aos professores Eduardo Gregores, Pedro Mercadante e Sandra Padula, pelos anos de apoio e ajuda em meu aprendizado.

Agradeço aos meus amigos no SPRACE, Ângelo, César, Caio, José, Sunil, e aos amigos do NCC, Allan, Cassio, Eduardo, Gabriel, Jadir, Márcio, Rogério, Sergio, por terem feito possível o meu trabalho.

Agradeço aos meus amigos Ana, Bruna, Flavio, Gustavo, Leandro, Luiza, Pedro Ivo, Tiago, por estarem ao meu lado nos bons e maus momentos.

Agradeço ao Diogo e à Fernanda, por serem minha família longe de casa.

Agradeço aos meus amigos do CERN, Alexandra, Analu, Leonardo, Luiz, Samir, Walter, pelos bons momentos e almoços em português.

I would like to thank my CERN friends, Jake, Jet, Sebastian, Stephen, William, for all the good moments around Geneva.

I would like to thank Falko Dulat for the help reviewing my thesis.

I would like to thank CMS Collaboration members for having worked so hard to make the exciting times come true.

I would like to thank CALTECH for the support.

Agradeço à FAPESP pelo apoio financeiro.

Agradeço à CAPES pelo apoio financeiro.

“Magicians and scientists are, on the face of it, poles apart. Certainly, a group of people who often dress strangely, live in a world of their own, speak a specialized language and frequently make statements that appear to be in flagrant breach of common sense have nothing in common with a group of people who often dress strangely, speak a specialized language, live in ... er ...”

Terry Pratchett, The Science of Discworld

Resumo

Apresentamos os resultados de uma busca por partículas exóticas que dão origem a um par VZ, onde V é um bóson W ou Z que decai hadronicamente em dois jatos sobrepostos enquanto o bóson Z decai em um par de elétrons ou múons. A análise usa dados de colisões próton-próton correspondentes a uma luminosidade integrada de 5 fb^{-1} coletados pelo experimento Compact Muon Solenoid no acelerador Large Hadron Collider a uma energia de centro de massa de 7 TeV em 2011. Não foram observados excessos significativos na distribuição de massa do par VZ em relação ao esperado pelos processos do Modelo Padrão. Dessa forma, limites superiores foram determinados, com 95% de confiança, para a seção de choque vezes a razão de ramificação de partículas hipotéticas decaindo no estado final VZ, em função da massa, em dois modelos de referência. Para ressonâncias de grávitons no modelo de Randall-Sundrum, com o parâmetro de acoplamento $k/\overline{M}_{Pl} = 0.05$, massas no intervalo [750, 924] GeV/c^2 são excluídas. Para bósons W' no Modelo Padrão Sequencial, massas no intervalo [700, 929] GeV/c^2 puderam ser excluídas. Esses são os primeiros resultados do LHC em buscas por ressonâncias decaindo em VZ, usando estados finais com um jato massivo de altíssimo momento transversal e um par de léptons.

Palavras Chaves: Física de Altas Energias; Física de Partículas; Colisores Hadrônicos; Dimensões Extras; Física Além do Modelo Padrão.

Áreas do conhecimento: Física; Física de Altas Energias; Física de Partículas.

Abstract

A search for new exotic particles decaying to VZ was performed, where V is either a W or a Z boson decaying hadronically into two overlapping jets and the Z decays into a pair of electrons or muons. The analysis uses a data sample of proton-proton collisions corresponding to an integrated luminosity of 5 fb^{-1} collected by the Compact Muon Solenoid experiment at the Large Hadron Collider at a center-of-mass energy of 7 TeV in 2011. No significant excess was observed in the mass distribution of the VZ candidates compared with the background expectation from Standard Model processes. Therefore, upper limits at the 95% confidence level were set on the product of the cross section times the branching fraction of hypothetical particles decaying to the VZ final state, as a function of the mass, in two benchmark models. In the Randall-Sundrum model for graviton resonances with $k/\overline{M}_{Pl} = 0.05$, masses between 750 and 924 GeV/c^2 were excluded. Sequential Standard Model W' bosons with masses between 700 and 929 GeV/c^2 were also excluded. These are the first results from the LHC on VZ searches using final states with a boosted massive jet and a lepton pair.

Contents

Chapter 1

Introduction

Particle physics or high energy physics is the branch of science that studies the particles that are the constituents of matter and their interactions. In our current understanding, particles are viewed as excitations of quantum fields that interact according to a quantum field theory called Standard Model (SM).

The Standard Model was built along the second half of the 20th century, and the history of its development shows an interplay between the theoretical predictions and the experimental discoveries that demonstrates the importance of these two aspects of physics to be intimately connected. The theory has a set of elementary particles consisting of leptons and quarks. The latter can combine to form composite states — the hadrons — accounting for hundreds of such particles. The SM is described as a quantum field theory with local gauge symmetry, referring to the strong ($\mathrm{SU}(3)_C$) and electroweak ($\mathrm{SU}(2)_L \otimes \mathrm{U}(1)_Y$) interactions.

The SM has been tested in a large variety of experiments at a vast range of energy or distance scales, and it agrees with the experimental tests performed to date. It predicted the neutral current weak interactions and the existence of the W and Z intermediate vector bosons, and shows an outstanding agreement in tests such as the total Z decay rate, lepton universality, the forward-backward asymmetries, the loop prediction of the top quark mass, to mention a few. The determination of the number of light neutrino reinforces the evidence for three fermonic families.

Nevertheless, the SM is not expected to be the final description of the fundamental interactions, as it presents outstanding issues that must be addressed: it does not accommodate a quantum theory of gravity; it does not predict any particle to explain the dark matter, a hypothetical kind of matter suggested by several results from astronomy and cosmology; and it does not explain the baryon asymmetry seen in the universe. On the theoretical side, the SM does not address the hierarchy between gravitational and electroweak forces, or the hierarchy between the fermion masses and the mixing between its different flavors; and it does not give a reason for the electric charge quantization. It is expected that a more fundamental theory awaits discovery, and that the SM would be the low–energy manifestation of a more complete description of the Universe.

One of the essential parts of the SM is the Higgs mechanism, which spontaneously breaks the electroweak symmetry and gives masses to the W and Z bosons. Fermions masses are a result of their Yukawa interaction with the Higgs field. The simplest implementation of the mechanism adds a Higgs doublet to the SU(2) $\otimes$ U(1) gauge theory. The spontaneous symmetry breaking of the underlying local symmetry triggers the conversion of the would-be Goldstone bosons to produce the mass terms for the weak gauge bosons. This mechanism leaves behind an elementary scalar particle, known as Higgs boson. The mass of the Higgs boson is a free parameter in the theory, and its search motivates particle physics experiments in the past four decades.

On 4 July 2012, the CMS and the ATLAS experimental teams at the Large Hadron Collider independently announced that they each confirmed the formal discovery of a previously unknown boson of mass around 125 GeV/c^2, whose properties measured so far has been consistent with what we would expect for the Higgs boson. Further studies of the new particle are being conducted with the new data delivered by the LHC in the second half of 2012 and will enlighten its nature.

The confirmation of the SM Higgs discovery — the last missing piece of the Standard Model — would validate the spontaneous symmetry breaking and the Higgs mechanism as the real responsible for the mass generation. However, in many extensions of the Standard Model a spontaneous breaking of the electroweak symmetry is associated with new strong dynamics appearing at the TeV scale. For instance, the origin of the new dynamics can be due to new interactions [1, 2, 3], compact extra dimensions [4, 5], composite nature of the Higgs boson [6, 7], or modified models where the Higgs have anomalous couplings [8].

In such scenarios the SM is an effective low-energy theory, valid for energies smaller than a new-physics scale Λ. In these theories, one expects the existence of new resonances coupling to pairs of vector bosons (ZZ, WZ, and WW). A minimal ultraviolet completion of this effective theory for composite models is described in Ref. [9]. Other examples include Randall–Sundrum gravitons [4, 5] coupled to ZZ and WW, or technimesons [10, 11] coupled to WZ. These scenarios could be tested at the LHC, as long as $\Lambda \sim \mathcal{O}(\text{TeV})$, as suggested by the electroweak symmetry breaking scale.

The LHC was built in the European Organization for Nuclear Research (CERN) site in the border of Switzerland and France. It was projected to deliver proton-proton collisions at 14 TeV of center of mass energy, and lead-lead collisions at 5.52 TeV. Its main purpose is to investigate the structure of the matter in the energy scales greater than 1 TeV, corresponding to length scale smaller than 10^{-18} m. The LHC have four main detectors: ATLAS and CMS are general purpose facilities, the LHCb is mainly focused on b physics and the study of the CP violation mechanisms, and ALICE was projected to look at dense nuclear matter.

The two general purpose experiments at the LHC were designed to detect events coming from almost any kind of new physics that might be relevant at the TeV scale, in such a way their data can finally elucidate the electroweak symmetry breaking mechanism. In particular, the ability to detect the Standard Model Higgs boson was the main reference requisite to evaluate the performance of the detectors' project in the begin of the 90's. The SM Higgs boson decay modes are strongly dependent on its mass, and to account for the essential need to accurately detect leptons, photons, jets and missing transverse energy, the ATLAS and CMS were projected as hermetic multilayer detectors which are able to observe almost all known particles.

The excellent detection capability of the general purpose experiments at the LHC make them adequate to also look for different beyond the Standard Model physics. The scope of the present thesis is the search for experimental evidence of new exotic resonances. In the next chapter, detailed descriptions of the LHC and the CMS experiment are presented. In Chapter 3, the Standard Model of particle physics and some of its main features are discussed. Chapter 4 describes the framework, phenomenology and experimental prospects of the warped extra dimensions theory, known as the Randall-Sundrum model. In Chapter 5, the search for heavy resonances decaying to vector boson V ($V = W, Z$) pairs is presented, with one boson being a $Z \to \ell^+\ell^-$ ($\ell = \mu,\ e$), and the other one decaying hadronically, *i.e.* $V \to q\bar{q}$, with the two outgoing quarks overlapping into a single massive jet. The signal is characterized as a peak in the invariant mass of the VZ system, and results are presented in terms of two benchmark scenarios: a RS graviton G_{KK} decaying to ZZ and the Sequential Standard Model (SSM) in which a new gauge boson W' with the same couplings as the SM W boson decays to a WZ pair. In both scenarios the search considers resonances heavier than 700 GeV/c^2, where the boosted topology becomes relevant.

The results from this analysis were scrutinized by the CMS Collaboration in several steps: internal approval, *Analysis Review Committee* (ARC) approval, after which the results became public through a *Physics Analysis Summary* (PAS). The PAS is an official public document detailing the analysis methods and results, and it was approved by the CMS Collaboration in May 2012 [12]. Further steps included a paper elaboration, which was approved by a *Collaboration Wide Review* (CWR) and the final version will be submitted to Journal of High Energy Physics for publication [13].

Chapter 2

LHC and the CMS Experiment

The prime motivation of the Large Hadron Collider is to elucidate the nature of the electroweak symmetry breaking, for which the Higgs mechanism is presumed to be responsible [14]. In the Standard Model, the Higgs mechanism is responsible for the mass generation of the weak vector bosons and the fermions that are the constituents of matter. The Higgs boson is a remnant of this mechanism, and its discovery has been the most important challenge on high energy physics for the past four decades. Although the theory does not predict its mass, there are strong indirect indications that point towards values that are accessible on LHC. Once the mass is known, all the other properties of the Higgs boson are predicted by the Standard Model. The new particle discovered by the LHC experiments this year, with mass $\sim$125 GeV/c^2, might be the Higgs boson, and shows that the accelerator and its experiments are able to accomplish the physics program which motivated their design.

Besides scrutinizing the Standard Model, the LHC experiments also aim to search for hints of new physics beyond the Standard Model. There is a large spectrum of theoretical models that predict different scenarios that can be tested at the LHC. Among them, it is worth mentioning supersymmetry (SUSY), extra dimensions (ED), technicolor, extended gauge group bosons (W', Z') models. The LHC was designed to expand the frontiers of the knowledge in high energy physics: it should be capable of revealing the behavior of matter in energy scales never yet explored.

2.1 The LHC

The Large Hadron Collider is a two-ring superconducting hadron accelerator and collider installed in the existing 26.7 km tunnel from the previous CERN experiment, the Large Electron-Positron Collider (LEP). The tunnel has eight straight sections and eight arcs and lies between 45 and 170 meters below the surface on a plane inclined at 1.4% sloping towards the *Lac Léman*. The machine was designed to operate at 14 TeV of centre of mass energy.

The LHC has two high luminosity experiments, ATLAS and CMS, both aiming at the peak luminosity of $L = 10^{34}$ cm^{-2}s^{-1} for proton collisions. The number of events per second generated is given by

$$N_{\text{event}} = L\sigma_{\text{event}} \,, \tag{2.1}$$

where σ_{event} is the cross section for the event under study and L the machine luminosity.

There are also two low-luminosity experiments: LHCb aiming to peak at $L = 10^{32}$ cm^{-2}s^{-1}, and TOTEM, for the detection of protons from elastic scattering, aiming to peak at $L = 2 \times 10^{29}$ cm^{-2}s^{-1}. In addition to the proton beams, the LHC is also operated with ion beams. ALICE is a dedicated experiment to measure heavy ion collisions, aiming at a peak luminosity of $L = 10^{27}$ cm^{-2}s^{-1} for nominal lead-lead operation. The ATLAS and CMS experiments also take data during the heavy ion runs.

The beam of the LHC is first accelerated in LINAC2, a linear accelerator, that reaches 50 MeV of energy. In the next step, the beam reaches 1.4 GeV, through a multi-ring booster synchrotron, and then the 628 m circumference Proton Synchrotron (PS) machine accelerates it up to 26 GeV. At the PS, the beam is split in bunches, with the same pattern and spacing that it ends up having at the LHC. A transfer is made to the 7 km Super Proton Synchrotron (SPS) machine, and it is further accelerated to 450 GeV. Then it is ready to be injected at the LHC. The cycle takes about 20 s to create a train of bunches with total kinetic energy of more than 2 MJ, that is about 8% of the beam needed to fill an LHC ring completely. The whole cycle is repeated 12 times per ring. Fig 2.1 shows schematically the layout of the CERN accelerator complex and the crossing points, where the four main experiments are located.

2.2 The CMS Experiment

Collider detectors consist of layers of sensible devices, located around the collision point, that exploit the different properties of the particles produced in the reaction. To be able to meet the goals of the LHC physics program, a general purpose detector has to follow some requirements:

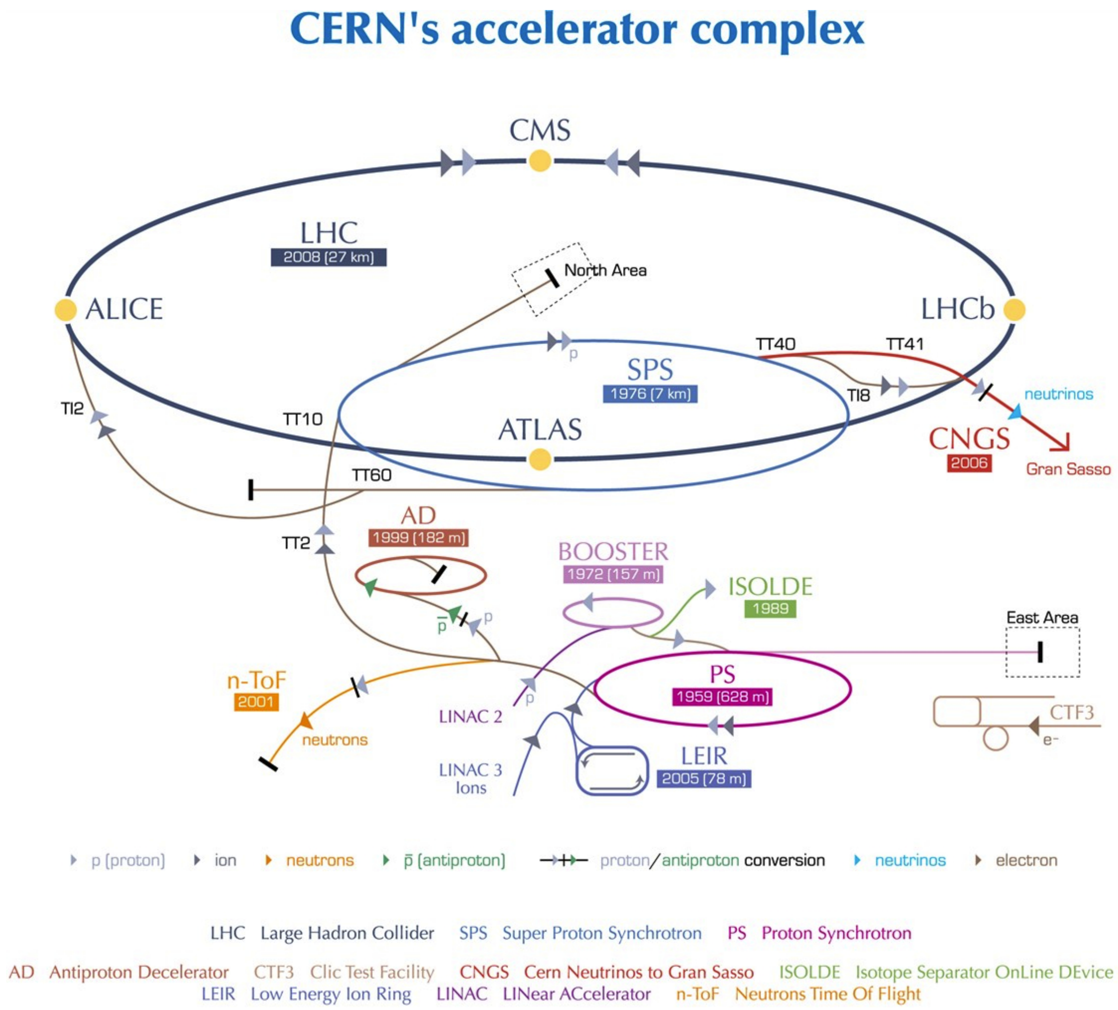

Figure 2.1: Layout of the CERN accelerator complex, including the elements of the LHC injector chain. The four intersection regions of the main LHC experiments (ALICE, ATLAS, CMS and LHCb) are also shown [15].

- Good muon momentum resolution and identification over a wide range of momenta and a large angular coverage ($|\eta| < 2.5$ [1]), good di-muon mass resolution (about 1% at 100 GeV/c^2) and the ability to unambiguously determine the charge of these particles with $p < 1$ TeV/c;
- Good reconstruction efficiency and momentum resolution of charged particles in the inner tracker. For efficient triggering and offline tagging of taus and b-jets, a pixel detector close to the interaction region is required;
- Good electromagnetic energy resolution, good di-photon and di-electron mass resolution (about 1% at 100 GeV/c^2), wide geometric coverage ($|\eta| < 3.0$), capability to measure the direction of photons and/or to determine the correct localization of the primary interaction vertex, good π^0 rejection and efficient photon and lepton isolation at high luminosities;
- Good transverse energy ($\not{E}_{\mathrm{T}}$) and di-jet mass resolution, requiring hadron calorimeters with a good geometric coverage ($|\eta| < 5$) and with fine lateral segmentation ($\Delta\eta \times \Delta\phi < 0.1 \times 0.1$).

The design of CMS meet these requirements [14], with distinguished features being the high-field solenoid, a full silicon based inner tracking system, and a fully active scintillating crystal-based electromagnetic calorimeter.

2.2.1 CMS Sub-detectors

The Compact Muon Solenoid (CMS) is a multi-purpose detector and its schematic view is shown in Fig 2.2. The CMS experiment is 21 m long, 15 m wide and 15 m high. It is constituted by layers, each one of them designed to measure a different type of particle emerging from proton-proton or heavy ion collisions.

The detector is built around a 13 m long, 5.9 m inner diameter solenoid magnet, a cylindrical coil of superconducting cable, kept at $-268.5°$C. It generates a magnetic field of 3.8 Tesla. The high magnetic field was chosen in order to achieve a good momentum resolution within a compact spectrometer. The return field is large enough to saturate 1.5 m of iron, allowing 4 muon stations to be integrated to ensure robustness and full geometric coverage. Each muon station consists of several layers of aluminum drift tubes (DT) in the barrel region and cathode strip

---

[1] The quantity η is the pseudorapidity, defined as $\eta = -\ln[\tan(\theta/2)]$.

chambers (CSC) in the end-cap region, complemented by resistive plate chambers (RPC).

The bore of the magnet coil accommodates the inner tracker and the calorimetry inside. The tracker is a cylinder of length 5.8 m and diameter 2.6 m. There are 10 layers of silicon micro-strip detectors, that gives good granularity and precision to deal with high track multiplicities. In addition, three layers of silicon pixel detectors are placed close to the interaction point, to improve measurement of the impact parameter of charged particle tracks, as well as the position of secondary vertices.

The electromagnetic calorimeter (ECAL) uses lead tungstate ($PbWO_4$) crystals with coverage in pseudorapidity up to $|\eta| = 3.0$. The scintillation light is detected by silicon avalanche photodiodes (APD) in the barrel region and vacuum phototriodes (VPT) in the end-cap region. A pre-shower system is installed in front of the end-cap ECAL for π^0 rejection. The ECAL is surrounded by a brass/scintillator sampling hadron calorimeter with coverage up to $|\eta| = 3.0$. The scintillation is converted by wavelength-shifting (WLS) fibers embedded in the scintillator tiles and channeled to photodetectors via clear fibers. This light is detected by novel photodetectors (hybrid photodiodes, or HPD) that can provide gain and operate in high axial magnetic fields. This central calorimetry is complemented by a tail-catcher in the barrel region, enduring that hadronic showers are sampled with nearly 11 hadronic interaction lengths. Coverage up to pseudorapidity of 5.0 is provided by an iron/quartz fibre calorimeter. The Cherenkov light emitted in the quartz fibers is detected by photomultipliers. The forward calorimeters ensure full geometric coverage for the measurement of the transverse energy in the event.

Within the LHC, bunches of particles collide up to 40 million times per second, so a trigger system that saves only potentially interesting events is essential. This reduces the number recorded from one billion to around 100 per second.

2.2.2 Inner Tracking System

Robust tracking and detailed vertex reconstruction are expected to play an essential role for an experiment designed to address the full range of physics which can be accessed at the LHC. The inner tracking system is the subsystem localized in the most inner part on the CMS and, consequently, subject to the highest particle flux density. This makes the choice of its constituents a delicate task, since the radiation hardness of the materials has to be considered. The CMS

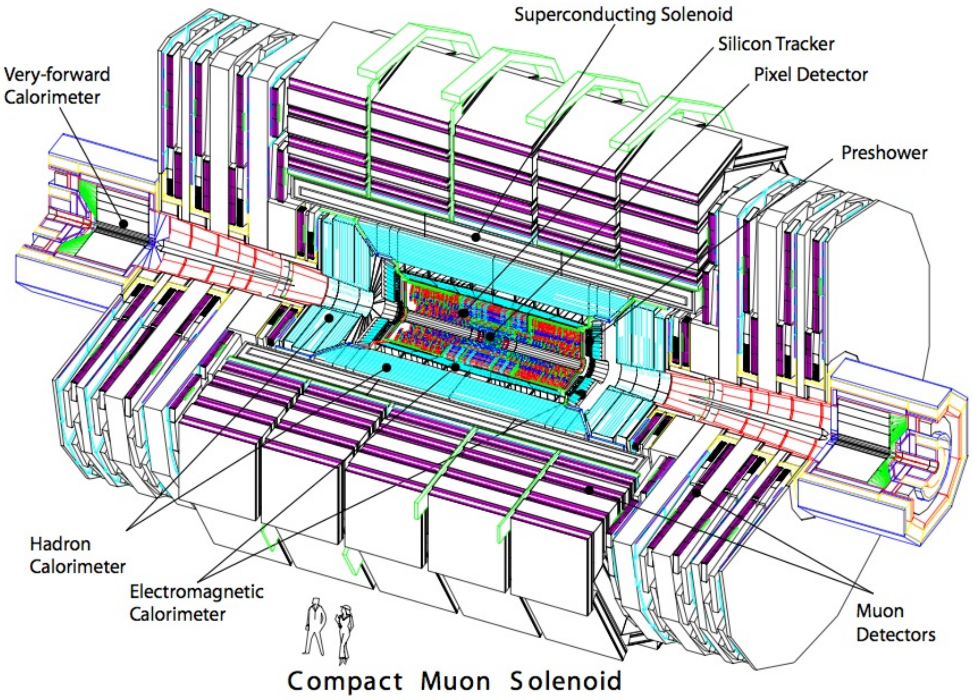

Figure 2.2: Expanded view of the CMS detector [16].

tracker records the paths taken by charged particles by finding their positions at a number of key points.

By considering the charged particle flux at various radii at high luminosity, there are three regions in the tracker that can be delineated:

- Pixel detectors: closest to the interaction vertex, where the particle flux is highest ($\approx 10^7$/s at $r \approx 10$ cm for the LHC design luminosity). The size of the pixel is $\approx 100 \times 150$ μm^2, giving an occupancy of about 10^{-4} per pixel per LHC crossing;

- Intermediate region silicon micro-strip detectors: in this region ($20 < r < 55$ cm), the particle flux is low enough to enable the use of silicon micro-strip detectors with a minimum cell size of 10 cm $\times$ 80 μm, leading to an occupancy of $\approx 2-3\%$ per LHC crossing;

- Outermost region silicon micro-strip detectors: for $r > 55$ cm, the particle flux has dropped sufficiently to allow use of larger-pitch silicon micro-strips with a maximum cell size of 25 cm $\times$ 180 μm, whilst keeping the occupancy to $\approx 1\%$.

The pattern recognition algorithm adopted by CMS for tracker reconstruction have to process a large number of hits per event: typically 5×10^3 hits at low luminosity and ten times more at high luminosity. In order to overcome the severe combinatorial problems the concept of *road* preselection is used in the first stage of the algorithms. In the second stage, the Kalman filter is used to carry out final hit selection and track fitting. Three programs have been developed: the Global Track Finder (GTF), the Connection Machine (CM) and the Forward Kalman Filter (FKF). They all require a *learning* phase where the information of the detector geometry is processed once in order to create a database used in the pattern recognition phase. The algorithms work with a simplified geometry where the detectors are 2D planes organized in layers, an average material distribution is used, and the radial component of the magnetic field is assumed to be zero.

Tracks with $p_{\mathrm{T}} > 0.8$ GeV/c and $|\eta| < 2.4$ originating from the interaction point have ideally between 8 and 15 hits. The hits in the tracker fall into three categories: pixel hits, with high accuracy in both local coordinates; hits in the individual silicon detectors, with precise position measurements in the direction normal to the strips; finally, measurements in twin detectors can be combined together to provide better precision. Of the thirteen or more nominal hits per track available in the detector, some may be missing due to inefficiency or badly measured tracks because of the overlapping. The algorithm have to exclude these *bad hits* and skip missing layers during the pattern recognition phase [17].

The Combinatorial Kalman Filter is a local method — reconstructs one track at a time, starting from an initial trajectory. It uses a recursive procedure to estimate track parameters from a set of reconstructed hits. It takes into account the energy loss and multiple scattering between layers, and integrates patter recognition and track fitting. The KF is mathematically equivalent to a global least square minimization, which is optimal when the model is linear and the random noise is Gaussian.

The steps of track reconstruction by this algorithm can be summarized as:

- Trajectory building: trajectories are extrapolated from layer to layer, accounting for multiple scattering and energy loss. On the new layer, new trajectories are constructed, with updated parameters (and errors) for each compatible hit in the layer. In this way, only the last layer estimate is based on the full track candidate information;

- Trajectory cleaning: removal of any possible ambiguity in the process of the trajectory building;

- Trajectory smoothing: this is the final fit of trajectories. It is done by obtaining the optimal estimates at every measurement point along the track. This procedure provides more accurate rejection of outliers (points outside the trajectory).

For non-linear models or non-Gaussian noise, the Adaptive Filters are used. One method, important for the reconstruction of electrons, is the Gaussian Sum Filter (GSF). It is suitable when the measurement errors have tails and there is a non-Gaussian distribution of energy loss and bremsstrahlung. The method uses a model with the distribution function described by a mixture of gaussians: the main component of the mixture describes the core of the distribution, while the tails are described by one or several additional Gaussians. The GSF is a non-linear generalization of the Kalman Filter (a weighted sum of several Kalman Filters).

2.2.3 Electromagnetic Calorimeter

The Electromagnetic Calorimeter (ECAL) is a hermetic, homogeneous calorimeter comprising 61,200 lead tungstate ($PbWO_4$) crystals mounted in the central barrel part, closed by 7,324 crystals in each of the 2 end-caps. These crystals have short radiation ($\chi_0 = 0.89$ cm) and Molière (2.2 cm) lengths, are fast (80% of the light is emitted within 25 ns) and radiation hard (up to 10 Mrad). However, the relatively low light yield (30 γ/MeV) requires use of photodetectors with intrinsic gain that can operate in a magnetic field. Silicon avalanche photodiodes (APD) are used as photodetectors in the barrel and vacuum photo-triodes (VPT) in the end-caps. In addition, the sensitivity of both the crystals and the APD response to temperature changes requires a temperature stability (the goal is 0.1 $^\circ C$). The use of $PbWO_4$ crystals has thus allowed the design of a compact calorimeter inside the solenoid that is fast, has fine granularity, and is radiation resistant.

The geometrical crystal coverage extends to $|\eta| = 3$. Precision energy measurement, involving photons and electrons, are carried out to $|\eta| < 2.6$. This limit has been determined by considerations of the radiation dose and amount of pileup energy and matches the geometric acceptance of the inner tracking system. The schematic view of a quadrant of the calorimetry and tracking system can be seen in Fig 2.4.

A total thickness of about 26 radiation lengths at $|\eta| = 0$ is required to limit the longitudinal shower leakage of high-energy electromagnetic showers to an acceptable level. This corresponds to a crystal length of 23 cm in the barrel region. The presence of a pre-shower in the end-cap allows the use of slightly shorter crystals (22 cm). The energy resolution has been parametrized for the energy range of about 25 GeV to 500 GeV, appropriate for photons from the $H \rightarrow \gamma\gamma$ decay, as

$$(\sigma/E)^2 = (a/\sqrt{E})^2 + (\sigma_n/E)^2 + c^2 \,, \tag{2.2}$$

where a is the stochastic term, σ_n the noise, and c the constant term. The energy E is in units of GeV. The stochastic term includes fluctuations in the shower containment as well as a contribution of photo-statistics. The noise term contains the contributions from electronic noise and pileup energy; the former is quite important at low energy, the latter is negligible at low luminosity. The constant term must be kept down to 0.55% in order to profit from the excellent stochastic term of $PbWO_4$ in the energy range relevant for the Higgs search. To achieve this goal, in situ calibration/monitoring using isolated high p_T electrons is mandatory. Typical values of energy resolution as a function of energy is shown in Fig 2.3.

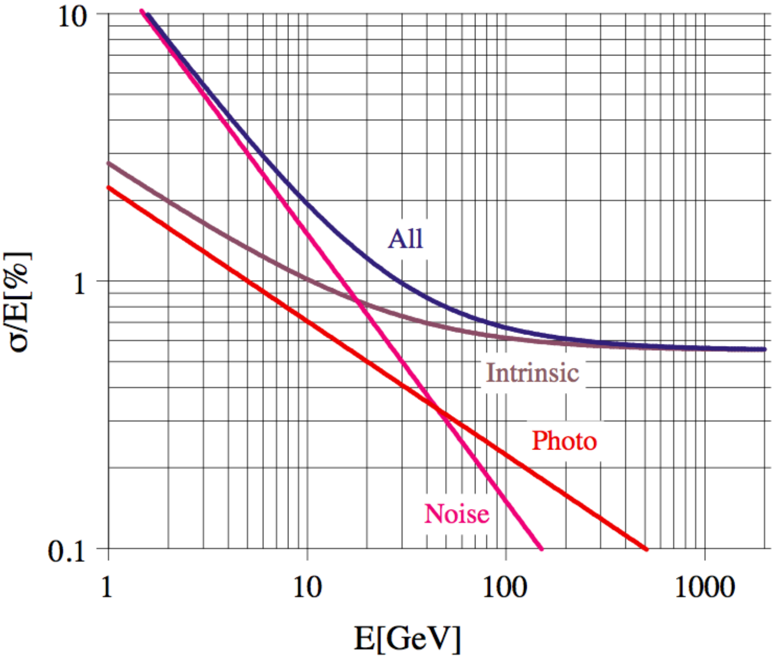

Figure 2.3: Different contributions to the energy resolution of the $PbWO_4$ calorimeter [18].

The pre-shower detectors are currently installed only in the end-caps, it covers a pseudorapidity range from $|\eta| = 1.65$ to 2.61, and it is placed in front of the crystals. It consists of lead converters followed by detector planes of silicon strip

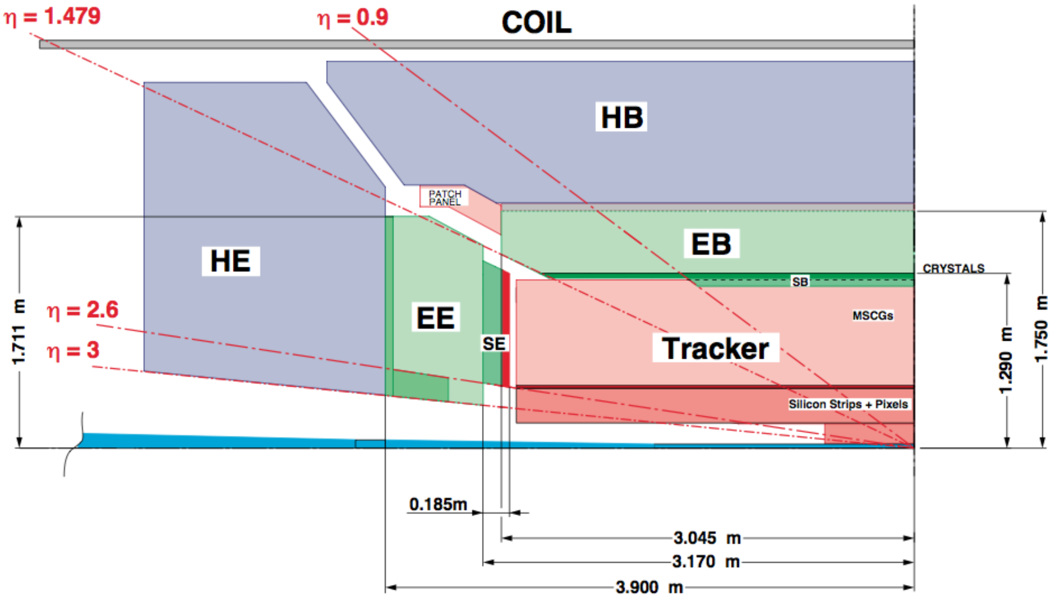

Figure 2.4: Schematic view of one quadrant of the calorimetry and tracking system [18].

with a pitch of < 2 mm. The impact position of the electromagnetic shower is determined by the centre-of-gravity of the deposited energy. The accuracy is typically 300 μm at 50 GeV. In order to correct for the energy deposited in the lead converter, the energy measured in the silicon is used to apply corrections to the energy measurement in the crystal. The fraction of energy deposited in the pre-shower (typically 5 % at 20 GeV) decreases with increasing incident energy. The main function of the pre-shower is to provide $\pi^0 - \gamma$ separation by detecting photons with good spatial resolution in order to distinguish pairs of closely-spaced photons from single photons. The installation of pre-shower detectors in the barrel is due to the high luminosity operation, if the activity of the minimum-bias events seen at LHC start-up shows that additional angular determination is necessary.

2.2.4 Hadron Calorimeter

The hadron calorimeters in conjunction with the ECAL sub-detectors form a complete calorimetry system for the measurement of jets and missing transverse energy. The central barrel and end-cap HCAL sub-detectors completely surround the ECAL and are fully immersed within the high magnetic field of the solenoid. The barrel (HB) and end-cap (HE) are joined hermetically with the barrel extending out to $|\eta| = 1.4$ and the end-cap covering the overlapping range $1.3 < |\eta| < 3.0$. The forward calorimeters are located 11.2 m from the interaction point and extend the pseudorapidity coverage overlapping with the end-cap from $|\eta| = 2.9$ down to $|\eta| = 5$. The forward calorimeters (HF) are specifically designed to measure energetic forward jets optimized to discriminate the narrow lateral shower profile and to increase the hermetic character of the missing transverse energy measurement. Central shower containment in the region $|\eta| < 1.26$ is improved with an array of scintillators located outside the magnet in the outer barrel hadronic calorimeter (HO).

The hadron calorimeter was designed taking into consideration that it is located inside the CMS magnet coil and surrounds the ECAL system. One important requirement of the HCAL is to minimize the non-Gaussian tails in the energy resolution and to provide good containment and hermetic character for the missing transverse energy measurement. Hence, the HCAL design maximizes material inside the magnet coil in terms of interaction lengths. This is complemented by an additional layer of scintillators, referred to as the hadron outer (HO) detector, lining the outside of the coil. Brass has been chosen as absorber material as it has a reasonably short interaction length, it is easy to machine and it is non-magnetic. Maximizing the amount of absorber before the magnet requires keeping to a minimum the amount of space devoted to the active medium. The tile/fibre technology makes for an ideal choice. It consists of plastic scintillator tiles read out with embedded wavelength-shifting (WLS) fibers. The WLS fibers are spliced to high-attenuation-length clear fibers outside the scintillator that carry the light to the readout system.

The photo-detection readout is based on multi-channel hybrid photodiodes (HPD). The absorber structure is assembled by bolting together precisely machined and overlapping brass plates so as to leave space to insert the scintillator plates, which have a thickness of 3.7 mm. The overall assembly enables the HCAL to be built with essentially no cracks without instrumentation or dead areas in ϕ.

The hadron barrel (HB) part of HCAL consists of 32 towers covering the pseudorapidity region $-1.4 < \eta < 1.4$, resulting in 2,304 towers with a segmentation $\Delta\eta \times \Delta\phi = 0.087 \times 0.087$. The HB is constructed in 2 half barrels, and is read out as a single longitudinal sampling. There are 15 brass plates, each with a thickness of about 5 cm, plus 2 external stainless steel plates for mechanical strength. Particles leaving the ECAL volume first see a scintillator plate with a thickness of 9 mm rather than 3.7 mm for the other plates. The light collected by the first layer is optimized to be a factor of about 1.5 higher than the other scintillator plates.

The hadron outer (HO) detector contains scintillators with a thickness of 10 mm, which line the outside of the outer vacuum tank of the coil and cover the region $-1.26 < \eta < 1.26$. The tiles are grouped in 30° sectors, matching the ϕ segmentation of the DT chambers. They sample the energy from penetrating hadron showers leaking through the rear of the calorimeters and so serve as a tail-catcher after the magnet coil. They increase the effective thickness of the hadron calorimetry to over 10 interaction lengths, thus reducing the tails in the energy resolution function. The HO also improves the missing transverse energy resolution of the calorimeter. HO is physically located inside the barrel muon system and is hence constrained by the geometry and construction of that system. It is divided into 5 sections along η, called rings -2, -1, 0, 1, and 2. The fixed ring-0 has 2 scintillator layers on either side of an iron absorber with a thickness of about 18 cm, at radial distances of 3.850 m and 4.097 m, respectively. The other mobile rings have single layers at a radial distance of 4.097 m. Each ring covers 2.5 m in z. HO scintillators follow the HCAL barrel tower geometry in η and ϕ.

Each hadron end-cap (HE) of HCAL consists of 14 η towers with 5° ϕ segmentation, covering the pseudorapidity region $1.3 < |\eta| < 3.0$. For the 5 outermost towers (at smaller η) the ϕ segmentation is 5° and the η segmentation is 0.087. For the 8 innermost towers the ϕ segmentation is 10°, whilst the η segmentation varies from 0.09 to 0.35 at the highest η. The total number of HE towers is 2304.

Coverage between pseudorapidities of 3.0 and 5.0 is provided by the steel/quartz fiber Hadron Forward (HF) calorimeter. Because the neutral component of the hadron shower is preferentially sampled in the HF technology, this design leads to narrower and shorter hadronic showers and hence is ideally suited for the congested environment in the forward region. The front face is located at 11.2 m from the interaction point. The depth of the absorber is 1.65 m. The signal originates from Cherenkov light emitted in the quartz fibers, which is then channeled by the fibers to photomultipliers. The absorber structure is created by machining 1 mm square grooves into steel plates, which are then diffusion welded. The diameter of the quartz fibers is 0.6 mm and they are placed 5 mm apart in a square grid. The quartz fibers, which run parallel to the beam line, have two different lengths (namely 1.43 m and 1.65 m) which are inserted into grooves, creating 2 effective longitudinal samplings. There are 13 towers in η, all with a size given by $\Delta\eta \approx 0.175$, except for the lowest-η tower with $\Delta\eta \approx 0.1$ and the highest-η tower with $\Delta\eta \approx 0.3$. The ϕ segmentation of all towers is 10°, except for the highest-η one which has $\Delta\phi = 20^\circ$. This leads to 900 towers and 1,800 channels in the 2 HF modules.

For evaluating the performance of the HCAL, the jet energy resolution and the missing transverse energy resolution are important parameters. The granularity of the sampling in the 3 parts of the HCAL has been chosen such that the jet energy resolution, as a function of the transverse energy, is similar in all 3 parts. This is illustrated in Fig 2.5. The resolution of the missing transverse energy in QCD dijet events with pile-up is given by

$$\sigma(E_T^{miss}) \approx 1.0\sqrt{\Sigma E_T}\ , \tag{2.3}$$

if energy clustering corrections are not made, while the average E_T^{miss} is given by:

$$< E_T^{miss} > \approx 1.25\sqrt{\Sigma E_T}\ . \tag{2.4}$$

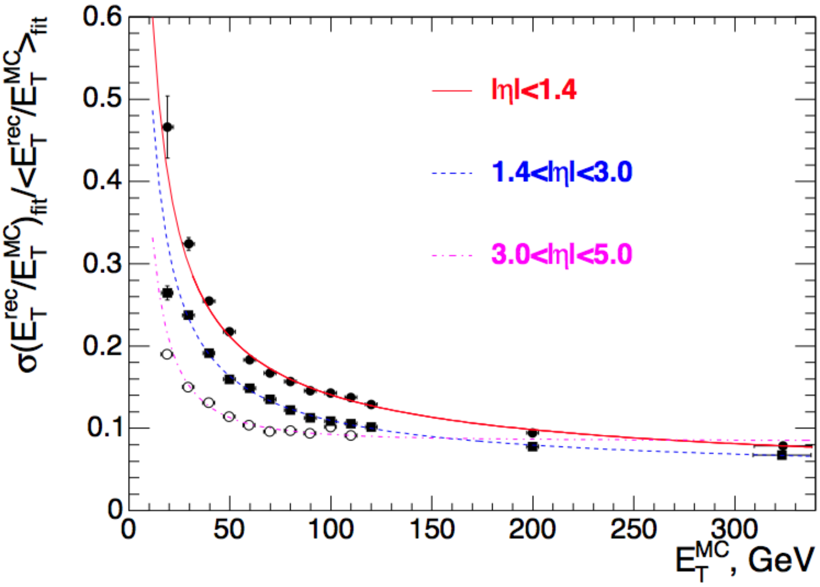

Figure 2.5: The jet transverse energy resolution as a function of the simulated jet transverse energy for barrel jets ($|\eta| < 1.4$), endcap jets ($1.4 < |\eta| < 3.0$) and very forward jets ($3.0 < |\eta| < 5.0$). The jets are reconstructed with the iterative cone R = 0.5 algorithm [16].

2.2.5 The Muon System

The muon system has three purposes: muon identification, muon trigger, and muon (signed) momentum measurement. Performance requirements follow the physics goals, including the maximum reach for unexpected discoveries, and the background environment of LHC at its highest luminosity. A robust 3.8 T solenoid-based system is the key to the CMS design. Comprehensive simulation studies have indicated that the physics goals can be achieved if the muon detector has the following functionality and performance [19]:

- Muon identification: at least 16 λ of material is present up to $|\eta| = 2.4$ with no acceptance losses;
- Muon trigger: the combination of precise muon chambers and fast dedicated trigger detectors provide unambiguous beam crossing identification and trigger on single and multi-muon events with well defined p_T thresholds from a few GeV/c to 100 GeV/c up to $|\eta| = 2.1$;
- Standalone momentum resolution from 8 to 15% $\delta p_T/p_T$ at 10 GeV/c and 20 to 40% at 1 TeV/c;
- Global momentum resolution after matching with the Central Tracker from 1.0 to 1.5% at 10 GeV/c, and from 6 to 17% at 1 TeV/c. Momentum-dependent spatial position matching at 1 TeV/c less than 1 mm in the bending place and less than 10 mm in the non-bending plane;
- Charge assignment correct to 99% confidence up to kinematic limit of 7 TeV;
- Capability of withstanding the high radiation and interaction background expected at the LHC.

Centrally produced muons are measured three times: in the inner tracker, after the coil, and in the return flux. Measurement of the momentum of muons using only the muon system is essentially determined by the muon bending angle at the exit of the 3.8 Tesla coil, taking the interaction point (which is known to $\approx 20\mu$m) as the origin of the muon. The resolution of this measurement (labelled muon system only) is dominated by multiple scattering in the material before the first muon station up to p_T values of 200 GeV/c, when the chamber spatial resolution starts to dominate. For low-momentum muons, the best momentum resolution (by an order of magnitude) is given by the resolution obtained in the silicon tracker (inner tracker only). However, the muon trajectory beyond the return yoke extrapolates back to the beam-line due to the compensation of the bend before and after the coil when multiple scattering and energy loss can be neglected. This fact can be used to improve the muon momentum resolution at high momentum when combining the inner tracker and muon detector measurements (full system).

Three types of gaseous detectors are used to identify and measure muons. The choice of the detector technologies has been driven by the very large surface to be covered and by the different radiation environments. In the barrel region ($|\eta| < 1.2$), where the neutron induced background is small, the muon rate is low and the residual magnetic field in the chambers is low, drift tube (DT) chambers are used. In the two end-caps, where the muon rate as well as the neutron induced background rate is high, and the magnetic field is also high, cathode strip chambers (CSC) are deployed and cover the region up to $|\eta| < 2.4$. In addition to this, resistive plate chambers (RPC) are used in both the barrel and the end-cap regions. These RPC are operated in avalanche mode to ensure good operation at high rates (up to 10 $\mathrm{kHz/cm^2}$) and have double gaps with a gas gap of 2 mm. RPC provide a fast response with good time resolution but with a coarser position resolution than the DT or CSC. RPC can therefore identify unambiguously the correct bunch crossing.

The DT or CSC and the RPC operate within the first level trigger system, providing two independent and complementary sources of information. The complete system results in a robust, precise and flexible trigger device. In the initial stages of the experiment, the RPC system covers the region $|\eta| < 1.6$. The coverage will be extended to $|\eta| < 2.1$ later.

The layout of one quarter of the CMS muon system for initial low luminosity running is shown in Fig 2.6. In the Muon Barrel (MB) region, four stations of detectors are arranged in cylinders interleaved with the iron yoke. The segmentation along the beam direction follows the five wheels of the yoke (labeled $YB-2$ for the farthest wheel in $-z$, and $YB+2$ for the farthest in $+z$). In each of the end-caps, the CSC and RPC are arranged in four disks perpendicular to the beam, and in concentric rings, three rings in the innermost station, and two in the others. In total, the muon system contains of order 25,000 $\mathrm{m^2}$ of active detection planes, and nearly 1 million electronic channels.

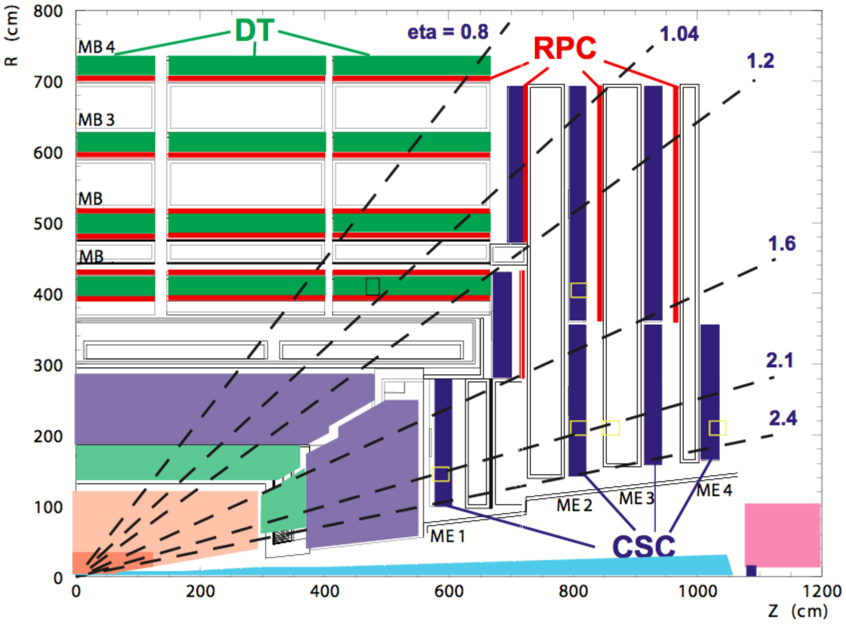

Figure 2.6: Layout of one quarter of the CMS muon system for initial low luminosity running. The RPC system is limited to $|\eta| < 1.6$ in the end-cap, and for the CSC system only the inner ring of the ME4 chambers have been deployed [16].

2.2.6 Trigger and Data Acquisition

The Trigger and Data Acquisition (DAQ) system of an experiment at a hadron collider plays an essential role because both the collision and the overall data rates are much higher than the rate at which one can write data to mass storage. At the LHC, the proton beams are designed to cross each other at a frequency of 40 MHz. At the design luminosity of 10^{34} $\mathrm{cm}^{-2}\mathrm{s}^{-1}$ each crossing results in an average of $\sim$20 inelastic pp events producing approximately 1 MB of zero-suppressed data. These figures are many orders of magnitude larger than the archival storage capability of $\mathcal{O}(10^2)$ Hz at data rates of $\mathcal{O}(10^2)$ MB/s.

The CMS Trigger and Data Acquisition System (TriDAS) is designed to inspect the detector information at the full crossing frequency and to select events at a maximum rate of $\mathcal{O}(10^2)$ Hz for archiving and later offline analysis. The required rejection power of $\mathcal{O}(10^5)$ is too large to be achieved in a single processing step, if a high efficiency is to be maintained for the physics phenomena CMS plans to study. For this reason, the full selection task is split into two steps. The first step (Level-1 Trigger) is designed to reduce the rate of events accepted for further processing to less than 100 kHz. The second step (High-Level Trigger or HLT) is designed to reduce this maximum Level-1 accept rate of 100 kHz to a final output rate of 100 Hz. Even though the system is optimized for the running conditions relevant to pp collisions, its performance is also adequate for Heavy Ion collisions.

The functionality of the CMS DAQ/HLT system is three-fold [20]:

- perform the readout of the front-end electronics after a Level-1 Trigger accept;
- execute physics selection algorithms on the events read out, in order to accept the ones with the most interesting physics content;
- forward these accepted events, as well as a small sample of the rejected events, to the online services which monitor the performance of the CMS detector and also provide the means of archiving the events in mass storage.

Another crucial function of the DAQ system is the operation of a Detector Control System (DCS) for the operation and supervision of all detector components and the general infrastructure of the experiment. The DCS is a key element for the operation of CMS, and guarantees its safe operation to obtain high-quality physics data.

The size of the LHC detectors and the underground caverns imposes a minimum transit time for signals from the front-end electronics to reach the services cavern housing the Level-1 trigger logic and return back to the detector front-end electronics. The total time allocated for the transit and for reaching a decision to keep or discard data from a particular beam crossing is 3.2 μs. During this time, the detector data must be held in buffers while trigger data is collected from the front-end electronics and decisions reached that discard a large fraction of events while retaining the small fraction of interactions of interest (nearly 1 crossing in 1,000). Of the total latency, the time allocated to Level-1 trigger calculations is less than 1 μs.

Custom hardware processors form the Level-1 decision. The Level-1 triggers involve the calorimetry and muon systems, as well as some correlation of information between these systems. The Level-1 decision is based on the presence of trigger primitive objects such as photons, electrons, muons, and jets above set E_T or p_T thresholds. It also employs global sums of E_T and E_T^{miss}. Reduced-granularity and reduced-resolution data are used to form trigger objects. The design value of 100 kHz is set by the average time to transfer full detector information through the readout system.

Upon receipt of a Level-1 trigger, after a fixed time interval of about 3.2 μs, the data from the pipelines are transferred to front-end readout buffers. After further signal processing, zero-suppression and/or data-compression, the data are placed in dual-port memories for access by the DAQ system. Each event, with a size of about 1.5 Mb (pp interactions), is contained in several hundred front-end readout buffers. Through the event building switch, data from a given event are transferred to a processor. Each processor runs the same high-level trigger (HLT) software code to reduce the Level-1 output rate of 100 kHz to 100 Hz for mass storage.

The use of a processor farm for all selections beyond Level-1 allows maximal benefit to be taken from the evolution of computing technology. Flexibility is maximized since there is complete freedom in the selection of the data to access, as well as in the sophistication of the algorithms. Various strategies guide the development of the HLT code. Rather than reconstruct all possible objects in an event, whenever possible only those objects and regions of the detector that are actually needed are reconstructed. Events are to be discarded as soon as possible. This leads to the idea of partial reconstruction and to the notion of many virtual trigger levels, e.g., calorimeter and muon information are used, followed by use of the tracker pixel data and finally the use of the full event information (including full tracking).

2.2.7 Software and Computing

The CMS software and computing systems need to cover a broad range of activities including the calibration of the detector; the storage, access, reconstruction and analysis of data; and the support of a distributed computing infrastructure for physicists engaged in these tasks. The storage, networking and processing power needed to analyze these data is well in excess of today's facilities and exceed any reasonably projected capabilities of CERN's central computing systems. The CMS computing model is therefore highly distributed, with a primary Tier-0 centre at CERN being supplemented by Tier–1 and Tier–2 computing centers at national laboratories and universities worldwide.

New computing grid technologies are used to facilitate the seamless exploitation of these distributed centers. The Worldwide LHC Computing Grid (WLCG), a joint project of the experiments and laboratories, made the deployment of grid technologies for LHC [16].

The computing centers available to CMS around the world are distributed and configured in a tiered architecture that functions as a single coherent system. Each of the three tier levels provides different resources and services [21].

The first tier in the CMS model, for which there is only one site, CERN, is known as Tier-0 (T0). The T0 performs several functions:

- Accepts RAW data from the CMS Online Data Acquisition and Trigger System (TriDAS);
- Repacks the RAW data received from the DAQ into primary datasets based on trigger information (immutable bits);
- Archives the repacked RAW data to tape;
- Distributes RAW data sets among the next tier stage resources (Tier-1) so that two copies of every piece of RAW data is saved, one at CERN, another at a Tier-1;
- Performs PromptCalibration in order to get the calibration constants needed to run the reconstruction;
- Feeds the RAW datasets to reconstruction;
- Performs prompt first pass reconstruction which writes the RECO and Analysis Object Data (AOD) extraction;
- Distributes the RECO datasets among Tier-1 centers, such that the RAW and RECO match up at each Tier–1;
- Distributes full AOD to all Tier–1 centers.

The T0 does not provide analysis resources and only operates scheduled activities. The T0 merges output files if they are too small. The goal of CMS is to write appropriately sized data into the tape robots. Currently CMS typically imports 2-3 GB files, though 5-10 GB files are technically possible and are desirable for tape system performance. At CERN, though logically separated from the T0 is the CMS-CAF (CERN Analysis Facility). The CAF offers services associated with T1 and T2 centers and performs latency critical, non-automated activities. The CAF is not needed for normal Tier-0 operation; it is intended for short-term, high priority, human-operated calibration, physics validation and analysis.

There is a set of eleven Tier–1 (T1) sites, which are large centers in CMS collaborating countries (large national labs, e.g. FNAL, and RAL). Tier–1 sites are in general used for large-scale, centrally organized activities and can provide data to and receive data from all Tier–2 sites. Each T1 center:

- Receives a subset of the data from the T0 related to the size of the pledged resources in the WLCG MoU;
- Provides tape archive of part of the RAW data (secure second copy) which it receives as a subset of the datasets from the T0;
- Provides substantial CPU power for scheduled re-reconstruction, skimming, calibration, AOD extraction;
- Stores an entire copy of the AOD;
- Distributes RECOs, skims and AOD to the other T1 centers and CERN as well as the associated group of T2 centers;
- Provides secure storage and redistribution for MC events generated by the T2's (described below).

A more numerous set of smaller Tier–2 (T2) centers at universities, but with substantial CPU resources, provide capacity for user analysis, calibration studies, and Monte Carlo production. T2 centers provide limited disk space, and no tape archiving. T2 centers rely upon T1s for access to large datasets and for secure storage of the new data (generally Monte Carlo) produced at the T2. The MC production in Tier-2s is centrally organized, with generated MC samples being sent to an associated Tier-1 site for distribution among the CMS community. All other Tier-2 activities are user driven, with data placed to match resources and needs: tape, disk, manpower, and the needs of local communities. The Tier-2 activities are organized by the Tier–2 responsible in collaboration with physics groups, regional associations and local communities. In summary, the Tier–2 sites provide:

- Services for local communities;
- Grid-based analysis for the whole experiment (Tier-2 resources available to whole experiment through the grid);
- Monte Carlo simulation for the whole experiment.

The São Paulo Research and Analysis Center (SPRACE) was implemented in 2003 to provide the necessary means for the participation of high energy physics researchers from the State of São Paulo in DØ and CMS experiments. In 2005, SPRACE became part of the Open Science Grid (OSG), a consortium of universities, national laboratories and computing centers, which share a grid infrastructure over research networks via a common middleware.

By means of the Open Science Grid, SPRACE has become a Tier–2 in the hierarchical computing structure that is being used by the CMS experiment. The SPRACE computing center provides nowadays around more than 10 Teraflops of computing power and 800 TB of storage space and it has been contributing for the processing, storage and analysis of the data produced by CMS. The work presented in this Thesis have used extensively the SPRACE resources for analyzing the CMS data.

Chapter 3

The Standard Model of Particle Physics

The Standard Model of particle physics is the currently accepted theory concerning the phenomena observed at the smallest scales and highest energy densities. It explains the electromagnetic, weak, and strong interactions, which mediate the dynamics of the known subatomic particles.

The theory was formulated throughout the second half of the 20th century. During its development the interplay between theory and experiment was important, and nowadays the Standard Model is a theory which is exhaustively tested and consolidated [22]. Several discoveries, such as the bottom quark (1977), the top quark (1995) and the tau neutrino (2000) have given further credence to the Standard Model.

However, the Standard Model is recognized as an incomplete theory, because it does not incorporate neither the physics of dark energy nor a full theory of gravitation as described by General Relativity. It does not contain any viable dark matter candidates, does not account for neutrino masses and oscillations, and although is considered to be theoretically self-consistent, it has several apparent unnatural properties giving rise to puzzles like the strong CP problem and the hierarchy problem. More exotic models, which incorporate hypothetical particles, extra dimensions, and elaborate symmetries are built as an attempt to explain some of the unsolved issues of the Standard Model.

The Standard Model groups two major theories — electroweak and quantum chromodynamics — into an internally consistent theory that describes the interactions between all known particles in the framework of quantum field theory. The particle content and model structure are described in the next sections.

3.1 Particle Content

The Standard Model particle content can be divided, accordingly their spin, into bosons (particles with integer spin) and fermions (particles with half-integer spin). The fermions are classified according to their interactions: there are six quarks (up, down, charm, strange, top, bottom) and six leptons (electron, electron neutrino, muon, muon neutrino, tau, tau neutrino). Doublets are grouped together to form a generation, with corresponding particles exhibiting similar physical behavior. The fermion structure can be seen in Table 3.1.

Quarks carry color charge and interact via the strong interaction. The quarks are bounded and, due to a phenomenon called color confinement, they form color-neutral composite particles (hadrons) containing either a quark-antiquark pair (mesons) or three quarks (baryons). Protons and neutrons are the baryons with lowest mass. Besides color charge, quarks also have electric charge and weak isospin and hence participate in electroweak interactions along with charged leptons.

Leptons do not carry color charge. The three neutrinos do not carry electric charge either, so their dynamics is directly influenced only by the weak interaction, making them notoriously difficult to detect. However, by virtue of carrying an electric charge, electrons, muons, and taus all interact electromagnetically.

The first generation charged particles are stable; hence all ordinary (baryonic) matter is made of such particles. Specifically, all atoms consist of electrons orbiting atomic nuclei ultimately constituted of up and down quarks. Second and third generations are composed of increasingly heavy particles and the charged particles decay with very short lifetimes. Neutrinos of all generations also do not decay, and pervade the universe, but weakly interact with baryonic matter.

Table 3.1: Organization of the Standard Model elementary fermions in family structure.

	Charge	First Generation		Second Generation		Third Generation	
Quarks	$+2/3$	Up	u	Charm	c	Top	t
	$-1/3$	Down	d	Strange	s	Bottom	b
Leptons	-1	Electron	e^-	Muon	μ^-	Tau	τ^-
	0	Electron neutrino	ν_e	Muon neutrino	ν_μ	Tau neutrino	ν_τ

The Standard Model describes the interactions in terms of the exchanging of other particles, known as the force mediators. These particles, also called gauge bosons, mediate the strong, weak, and electromagnetic fundamental interactions. The quantum field theory description of particle interactions can be implemented using perturbation theory which allows for Feynman diagrammatic calculations that predict the outcome of scattering experiments. In the case of strong interactions, the asymptotic freedom of quantum chromodynamics is an essential ingredient to allow the perturbation theory to be applied.

The gauge bosons of the Standard Model include the photon and the weak vector bosons. The photon is massless and mediates the electromagnetic force between electrically charged particles which is well-described by the theory of quantum electrodynamics. The W^+, W^- and Z gauge bosons mediate the weak interactions between particles of different flavors (all quarks and leptons). They are massive due to the short distance character to the weak interaction. The $W^\pm$ couples exclusively to left-handed fermions (and right-handed anti-fermions), while the electrically neutral Z boson interacts with both left and right-handed particles. These three gauge bosons along with the photons are grouped together, as collectively mediating the electroweak interaction.

The eight gluons mediate the strong interactions between color charged particles (quarks), and are massless. The eightfold multiplicity of gluons is labeled by a combination of color and anti-color charge. Because the gluons have an effective color charge, they can also interact among themselves. The gluons and their interactions are described by the theory of quantum chromodynamics.

The Higgs mechanism, theorized by Robert Brout, François Englert, Peter Higgs, Gerald Guralnik, Carl Hagen, and Tom Kibble in 1964, is a key ingredient in the formulation to the Standard Model [23, 24, 25]. It plays a unique role in the model, explaining how the gauge bosons and the elementary particles acquire their masses. In electroweak theory, the Higgs boson is a remnant of the spontaneous breaking symmetry. He interacts with all massive particles and also have self-interaction.

Because the Higgs boson is quite massive and decays promptly after being created, only a very high energy particle accelerator, with high luminosity, can be able to produce and observe it. It remained as the only fundamental particle predicted by the Standard Model that was not found for a very long time. Experiments to confirm and determine the nature of the Higgs boson using the Large Hadron Collider (LHC) at CERN began in early 2010, and were performed at Fermilab's Tevatron until its closure in late 2011. Mathematical consistency of the Standard Model requires that any mechanism capable of generating the masses of elementary particles become accessible at energies not higher than 1.4 TeV [26]; therefore, the LHC had the main objective to answer the question of whether the Higgs boson actually exists.

On July 4th 2012, the two main experiments at the LHC (ATLAS [27] and CMS [28]) both independently reported the discovery of a new particle with a mass of about 125 GeV/c^2, which seems to be consistent with the Higgs particle. They acknowledged that further work would be needed to conclude if it is indeed the SM Higgs boson, *i.e.* if it has the predicted couplings to the other particles. On the other hand, the Tevatron experiments released a combination of their Higgs search which presents a broad 3.1σ excess in the [120-135] GeV/c^2 range, mainly from the $H \to b\bar{b}$ channel [29].

3.2 Field Content

The Standard Model has fields of spin one, half and zero. The spin one fields are related to the forces in the model, and each field has its own charge, which defines the interaction with the matter particles and fields. The symmetry groups and coupling strengths of the spin one fields are the following:

- $U(1)_Y$ gauge field $B_{\mu\nu}$ with coupling g' (weak hypercharge);
- $SU(2)_L$ gauge field W^i_μ, $i = 1, 2, 3$ with coupling g (weak isospin);
- $SU(3)_C$ gauge field G^a_μ $a = 1, \cdots, 8$ with coupling g_s (color charge).

The spin half fields are the matter particles, arranged in the fundamental representation of the gauge groups. All leptons and $SU(3)_C$ singlets and the quarks are $SU(3)_C$ triplets. The left-handed fermions, both leptons and quarks, are $SU(2)_L$ doublets and the right-handed ones are $SU(2)_L$ singlets. The weak hypercharge of the fields are given in terms of the third component of weak isospin and the electrical charge by

$$Y = 2(Q - T_3)$$

The scalar (spin zero) field, known as the Higgs field, is an $SU(2)_L$ doublet with $U(1)_Y$ hypercharge $+1$. The Higgs potential induces the spontaneous symmetry breaking of three out of the four generators of the gauge group $SU(2)_L \otimes U(1)_Y$, giving rise to three would–be massless Goldstone bosons, if they were not coupled to gauge fields. However, after symmetry breaking, these three degrees of freedom mix with three vectorial gauge bosons (W^+, W^- and Z) giving them an additional degree of freedom: the longitudinal component of their spins. The weak vector bosons become massive. A remaining degree of freedom remains in the theory as a physical field: the Higgs boson. The unbroken generator corresponds to the electromagnetic $U(1)$ group and, therefore, the photon remains massless.

3.3 Quantum Electrodynamics (QED)

Quantum Electrodynamics (QED) is the relativistic quantum field theory concerning the interaction of electrically charged particles with electromagnetic fields. It is the first theory where full agreement between quantum mechanics and special relativity is achieved. QED describes all phenomena involving electrically charged particles interacting by means of exchange of photons and represents the quantum counterpart of classical electrodynamics giving a complete account of matter and light interaction.

A fundamental feature of the electromagnetic field is the gauge invariance — a continuous local $U(1)$ transformation does not change the electromagnetic Lagrangian. Photons do not possess an electric charge and thus do not self-interact.

Mathematically, QED is an abelian gauge theory with the symmetry group $U(1)$. The gauge field, which mediates the interaction between the charged spin one–half fields, is the electromagnetic field. The QED Lagrangian for a spin one–half field interacting with the electromagnetic field is given by,

$$\mathcal{L}_{QED} = \bar{\psi}\left(i\gamma^{\mu}D_{\mu} - m\right)\psi - \frac{1}{4}F_{\mu\nu}F^{\mu\nu}\,, \tag{3.1}$$

where γ^{μ} are the Dirac matrices, the ψ a Dirac spinor field of spin one–half particles (*e.g.* electron–positron field), $\bar{\psi} \equiv \psi^{\dagger}\gamma_0$ is the Dirac adjoint, $D_{\mu} \equiv \partial_{\mu} + ieA_{\mu}$ is the gauge covariant derivative, e is the coupling constant (electric charge of the spinor field), A_{μ} is the covariant four-potential of the electromagnetic field generated by the electron itself and $F_{\mu\nu} = \partial_{\mu}A_{\nu} - \partial_{\nu}A_{\mu}$ is the electromagnetic field strength tensor. From the Lagrangian, it is straightforward to derive the equations of motion of the theory.

3.4 Quantum Chromodynamics (QCD)

Quantum Chromodynamics (QCD) is the theory which describes the strong nuclear force. Prior to 1950's, the strong nuclear force was theorized as a Yukawa interaction mediated by the exchange of π–mesons between protons and neutrons. Experimental advances, such as the invention of the bubble chamber and spark chambers, allowed a large number of particles to be discovered, the so–called hadrons. First, particles were classified by their charge and isospin by Eugene Wigner and Werner Heisenberg; then, in 1953, according to strangeness by Murray Gell-Mann and Kazuhiko Nishijima. In 1961, Murray Gell-Mann and Yuval Ne'eman invented the eightfold way to group the particles in a more insightful way. In 1963, Gell-Man and George Zweig, improving an earlier approach of Shoichi Sakata, proposed the structure of the groups could be explained by the existence of three flavors of smaller particles inside the hadrons: the quarks. Further research lead to the what is known today as the quark model.

The interactions of the quarks are governed by the QCD, a non-abelian Yang-Mills theory based on the SU(3) special unitary group. QCD introduces a color charge, as well anti-colors for the anti-particles. QCD describes the interaction involving the color charge, between the gauge boson — the gluon — and the quarks. The gluons also possess color charge and thus undergo self–interaction. Each gluon exists as a superposition of color and anti-color states and the set of different possible combinations form an octet.

The strong coupling constant α_s is the characteristic parameter of the strong nuclear force, and it is known to depend on the energy scale of the interaction. At small distances, the gluons provide an anti-screening effect that reduces the strength of the strong interaction, giving rise to the asymptotic freedom character of the strong interaction [30, 31]. Additionally, QCD requires that all free particles must be colorless, thus precluding any unbound quarks. This is known as confinement. This aspect of the theory is verified within lattice QCD computations, but is not mathematically proven.

The dynamics of the quarks and gluons are controlled by the quantum chromodynamics Lagrangian. The gauge invariant QCD Lagrangian is given by,

$$\mathcal{L}_{QCD} = \bar{\psi}_i \left(i\gamma_\mu D^\mu_{ij} - m\delta_{ij} \right) \psi_j - \frac{1}{4} G^a_{\mu\nu} G^{\mu\nu}_a \ , \tag{3.2}$$

where $(D_\mu)_{ij}$ is the covariant derivative, the $\psi_i(x)$ is the quark field in the fundamental representation of the SU(3)$_C$ gauge group, indexed by $i, j = 1, 2, 3$; $G^a_\mu(x)$ are the gluon fields in the adjoint representation of the SU(3)$_C$ gauge group, indexed by $a, b = 1, \cdots, 8$; the γ^μ are the Dirac matrices connecting the spinor representation to the vector representation of the Lorentz group.

The $G^a_{\mu\nu}$ represents the gauge invariant gluonic field strength tensor, analogous to the electromagnetic field strength tensor $F^{\mu\nu}$ in Electrodynamics. It is given by,

$$G^a_{\mu\nu} = \partial_\mu G^a_\nu - \partial_\nu G^a_\mu - g f^{abc} G^b_\mu G^c_\nu \, , \tag{3.3}$$

where the f_{abc} are the structure constants of $SU(3)_C$.

The constants m and g are the quark mass and coupling constants of the theory, subject to renormalization in the full quantum field theory. The associate Feynman rules for QCD can be extracted for the above Lagrangian 3.2 and involve the gluon interaction with the quark current and the 3– and 4–gluon vertices

3.5 Electroweak Model

The electroweak theory is the unified description of the weak nuclear theory and QED. Although the weak interaction and the electromagnetism appear in a very different way in the everyday low energies, they are two aspects of the same electroweak force.

The weak nuclear force has long been known to be short ranged, leading to the hypothesis that the mediator of the forces should be a massive particle with an exponentially-decaying Yukawa interaction. The culmination of intense effort to explain the nature of the electroweak forces is the Glashow-Weinberg-Salam (GSW) model, which is named after the three physicists awarded with the Nobel Prize of Physics in 1979.

The model started to become a new paradigm when the existence of a weak process without the exchange of charge was experimentally stablished by the observation of the neutral currents in neutrino scattering by the Gargamelle collaboration in 1973 [32], and with the discovery of W and Z gauge bosons in proton-antiproton collisions by UA1 [33, 34, 35] and UA2 [36, 37] in 1983.

Mathematically, the unification is accomplished under an $SU(2) \otimes U(1)$ gauge group. The corresponding gauge bosons are the three W bosons of weak isospin from $SU(2)_L$ (W^1, W^2 and W^3) and the B^0 bosons of weak hypercharge from $U(1)_Y$, all of which are introduced massless. The correspondent Lagrangian can be divided in four parts,

$$\mathcal{L}_{EW} = \mathcal{L}_g + \mathcal{L}_f + \mathcal{L}_h + \mathcal{L}_y \, . \tag{3.4}$$

The $\mathcal{L}_g$ term describes the propagation and the interactions between the gauge bosons $W^{1,2,3}$ and B^0:

$$\mathcal{L}_g = -\frac{1}{4} W^{a\mu\nu} W^a_{\mu\nu} - \frac{1}{4} B^{\mu\nu} B_{\mu\nu} \,, \tag{3.5}$$

where $W^{a\mu\nu}$ (a = 1,2,3) and $B^{\mu\nu}$ are the field strength tensors for the weak isospin and weak hypercharge fields.

The $\mathcal{L}_f$ term gives the kinetic term for the Standard Model fermions. The interaction between gauge bosons and fermions are introduced through the covariant derivative,

$$\mathcal{L}_f = \bar{Q}_i i \not{D} Q_i + \bar{u}_i i \not{D} u_i + \bar{d}_i i \not{D} d_i + \bar{L}_i i \not{D} L_i + \bar{e}_i i \not{D} e_i \,, \tag{3.6}$$

where the subscript i runs over all the three generations of fermions, Q, u, and d are the left–handed doublet, right–handed singlet up, and right–handed singlet down type quark fields, and L and e are the left–handed doublet and right–handed singlet lepton fields.

The $\mathcal{L}_h$ term includes the Higgs potential,

$$\mathcal{L}_h = |D_\mu h|^2 - \lambda \left(|h|^2 - \frac{v^2}{2} \right)^2 \,. \tag{3.7}$$

The $\mathcal{L}_y$ term gives the Yukawa interaction that generates the fermion masses after the Higgs acquires a vacuum expectation value,

$$\mathcal{L}_y = -y_{uij} h^\dagger \bar{Q}_i u_j - y_{dij} h \bar{Q}_i d_j - y_{eij} h \bar{L}_i e_j + h.c. \tag{3.8}$$

The spontaneous electroweak symmetry breaking is accomplished via the Higgs potential and gives rise to the Standard Model $W^\pm$ and Z bosons masses. The relation between the W^0 and B^0 and the Z boson and photon (γ) is given by

$$\begin{pmatrix} \gamma \\ Z^0 \end{pmatrix} = \begin{pmatrix} \cos\theta_W & \sin\theta_W \\ -\sin\theta_W & \cos\theta_W \end{pmatrix} \begin{pmatrix} B^0 \\ W^0 \end{pmatrix} . \tag{3.9}$$

The θ_W is the weak mixing angle, and can be seen as the rotation angle that diagonalizes the mass matrix of the (W^0, B^0) fields. The photon does not acquire mass since the group $\mathrm{U(1)_{em}}$ remains unbroken.

The electroweak Lagrangian, after the symmetry breaking, reorganizes itself after the Higgs boson acquires a vacuum expectation value, and can be divided into several parts,

$$\mathcal{L}_{EW} = \mathcal{L}_K + \mathcal{L}_N + \mathcal{L}_C + \mathcal{L}_H + \mathcal{L}_{HV} + \mathcal{L}_{WWW} + \mathcal{L}_{WWVV} + \mathcal{L}_Y \, . \tag{3.10}$$

The kinetic term $\mathcal{L}_K$ contains all the quadratic terms of the Lagrangian, which include the dynamic terms and the mass terms:

$$\begin{aligned} \mathcal{L}_K = & \sum_f \bar{f}(i\partial\!\!\!/ - m_f)f - \frac{1}{4}A_{\mu\nu}A^{\mu\nu} - \frac{1}{2}W^{+}_{\mu\nu}W^{-\mu\nu} + m_W^2 W^{+}_{\mu}W^{-\mu} \\ & - \frac{1}{4}Z_{\mu\nu}Z^{\mu\nu} + \frac{1}{2}m_Z^2 Z_\mu Z^\mu + \frac{1}{2}(\partial^\mu H)(\partial_\mu H) - \frac{1}{2}m_H^2 H^2 \, . \end{aligned} \tag{3.11}$$

The sum runs over all fermions of the theory (quarks and leptons), the stress tensor $A_{\mu\nu}$ is given by $A_{\mu\nu} = \partial_\mu A_\nu - \partial_\nu A_\mu$, and in a similar way for $Z_{\mu\nu}$, $W^{\pm}_{\mu\nu}$.

The W and Z bosons masses are given in terms of parameters measured at lower energies: electron charge e, Fermi constant G_F, and electroweak angle θ_W. The masses, at tree level, are given by,

$$M_W^2 = \frac{e^2}{4\sqrt{2}\sin^2\theta_W G_F} \, , \tag{3.12}$$

$$M_Z = \frac{M_W}{\cos\theta_W} \, . \tag{3.13}$$

The current experimental values [22] are $M_W = 80.385 \pm 0.015$ GeV/c^2 and $M_Z = 91.1876 \pm 0.0021$ GeV/c^2, in an impressive agreement with the expected values from theory.

The neutral current $\mathcal{L}_N$ and the charged current $\mathcal{L}_C$ contain the interactions between the fermions and gauge bosons,

$$\mathcal{L}_N = eJ^{em}_\mu A^\mu + \frac{g}{\cos\theta_W}(J^3_\mu - \sin^2\theta_W J^{em}_\mu)Z^\mu \, . \tag{3.14}$$

The electromagnetic current is given by

$$J^{em}_\mu = \sum_f q_f \bar{f}\gamma_\mu f \, ,$$

and the neutral weak current is given in terms of

$$J^3_\mu = \sum_f T^f_3 \bar{f}\gamma_\mu \frac{1-\gamma_5}{2} f \, ,$$

with q_f and T_3^f being the fermions' electric charges and weak isospin.

The charged current Lagrangian is given by,

$$\mathcal{L}_C = -\frac{g}{\sqrt{2}} \left[\bar{u}_i \gamma^\mu \frac{1-\gamma^5}{2} M_{ij}^{CKM} d_j + \bar{\nu}_i \gamma^\mu \frac{1-\gamma^5}{2} e_i \right] W_\mu^+ + h.c. \tag{3.15}$$

The Higgs three-point and four-point self-interaction terms are in $\mathcal{L}_H$,

$$\mathcal{L}_H = -\frac{g m_H^2}{4 m_W} H^3 - \frac{g^2 m_H^2}{32 m_W^2} H^4 \,. \tag{3.16}$$

The Higgs interactions with gauge vector bosons are in the term $\mathcal{L}_{HV}$,

$$\mathcal{L}_{HV} = \left(g m_W H + \frac{g^2}{4} H^2 \right) \left(W_\mu^+ W^{-\mu} + \frac{1}{2\cos^2\theta_W} Z_\mu Z^\mu \right) \,. \tag{3.17}$$

The gauge bosons three-point self-interactions are in $\mathcal{L}_{WWW}$,

$$\begin{aligned} \mathcal{L}_{WWW} = -ig \Big[& \left(W_{\mu\nu}^+ W^{-\mu} - W^{+\mu} W_{\mu\nu}^- \right) \left(A^\nu \sin\theta_W - Z^\nu \cos\theta_W \right) \\ & + W_\nu^- W_\mu^+ \left(A^{\mu\nu} \sin\theta_W - Z^{\mu\nu} \cos\theta_W \right) \Big] \,. \end{aligned} \tag{3.18}$$

The term $\mathcal{L}_{WWVV}$ contains the gauge four-point self interactions,

$$\begin{aligned} \mathcal{L}_{WWVV} = -\frac{g^2}{4} \Big\{ & \left[2 W_\mu^+ W^{-\mu} + \left(A_\mu \sin\theta_W - Z_\mu \cos\theta_W \right)^2 \right]^2 \\ & - \left[W_\mu^+ W_\nu^- + W_\nu^+ W_\mu^- + \left(A_\mu \sin\theta_W - Z_\mu \cos\theta_W \right) \left(A_\nu \sin\theta_W - Z_{nu} \cos\theta_W \right) \right]^2 \Big\} \end{aligned} \tag{3.19}$$

Finally, $\mathcal{L}_Y$ contains the Yukawa interactions between the fermions and the Higgs field,

$$\mathcal{L}_Y = -\sum_f \frac{g m_f}{2 m_W} \bar{f} f H \,. \tag{3.20}$$

All the factors $(1-\gamma^5)/2$ in the fermionic couplings project out the left–handed components of the spinor fields. After symmetry breaking, the electroweak theory is chiral.

Noether's first theorem states that any differentiable symmetry of the action of a physical system has a corresponding conservation law. The Poincaré and gauge symmetries were imposed to the Standard Model as conditions, on its formulation. However, there are four other exact symmetries that are accidental. They are continuous global U(1) symmetries that give rise to the barionic and leptonic flavor number conservation. To each quark is assigned a baryon number of $1/3$, and to every antiquark, $-1/3$. This implies, by baryon number conservation, that the number of quarks minus the number of antiquarks is a constant. Similarly, each electron and its associated neutrino is assigned an electron number $+1$, while its antiparticles carry electron number -1. The same for the muons, taus, its associated neutrinos and antiparticles. The Standard Model predicts that each of these three numbers should be conserved separately in a manner similar to the baryon number conservation. These numbers are collective known as the lepton family numbers. Besides the exact symmetries, there are the approximate symmetries, such as the SU(2) custodial symmetry and the SU(2) or SU(3) quark flavor symmetry.

3.6 Tests and Predictions

The Standard Model has been tested in a large variety of experiments at a vast range of energies and distance scales. The most comprehensive tests of the Standard Model were provided by electron-positron collisions in the LEP accelerator at CERN and the SLC accelerator at SLAC. Several measurements were made in the neighborhood of the Z^0 peak, which include [38]:

- **The total Z^0 decay rate**: In the absence of exotic decay modes, $\Gamma_Z = \Gamma_{ee} + \Gamma_{\mu\mu} + \Gamma_{\tau\tau} + N_\nu \Gamma_\nu + \Gamma_{had}$ and $\Gamma_\nu = 1.992 \pm 0.003\ \Gamma_{\ell\ell}$, where the three leptonic decay rates are equal if one assumes universality, and N_ν is the number of light neutrino species. Experimentally, $\Gamma_Z = 2.4952 \pm 0.0023$ GeV/c^2.

- **Number of light neutrino families**: From the high-precision measurement of Z^0 decay properties, LEP last value for the total number of neutrino species is [39] 2.9840 ± 0.0082, in agreement with the three observed generations of fundamental fermions.

- **Partial decay rates**: Looking at particular final states, it is possible to disentangle various partial decay rates of the Z^0. Particularly, $R_\ell = \Gamma_{had}/\Gamma_{\ell\ell}$ and $R_b = \Gamma_{b\bar{b}}/\Gamma_{had}$. Experimentally, $R_\ell = 20.788 \pm 0.032$ and $R_b = 0.2219 \pm 0.0017$.

- **Forward-backward asymmetries**: At tree level, it's possible to parametrize the angular distribution of $f\bar{f}$ $(f \neq e)$ final states by:

  $$\frac{d\sigma}{d\cos\theta}\left(e^+e^- \to \bar{f}f\right) \simeq \left(1+\cos^2\theta\right)F_1 + 2\ \cos\theta F_2 \tag{3.21}$$

  One then can define the forward-backward asymmetry:

  $$A_{FB} \equiv \frac{\int_0^1 - \int_{-1}^0}{\int_0^1 + \int_{-1}^0} = \frac{3F_2}{4F_1} \tag{3.22}$$

  which has the value $3(1-4\sin^2\theta_W)^2$ for $\mu^+\mu^-$ and $\tau^+\tau^-$. The experimental measurements are $A^{\ell}_{FB} = 0.0172 \pm 0.0012$, $A^{b}_{FB} = 0.0999 \pm 0.0031$ and $A^{c}_{FB} = 0.0725 \pm 0.0058$.

- **Polarized beam asymmetry**: If a longitudinally-polarized electron beam is available (as at the SLC), one can measure the total cross-section asymmetry:

  $$A_{LR} \equiv \frac{\sigma_L - \sigma_R}{\sigma_L + \sigma_R} = \frac{2(1-4\sin^2\theta_W)}{1+(1-4\sin^2\theta_W)} \tag{3.23}$$

  where L and R label the different electron helicities. The experimental measurement gives $\sin^2\theta_{eff}(A_{LR}) = 0.23049 \pm 0.00050$.

- **Loop prediction of top quark mass**: Through radiative corrections evaluated in the framework of the Standard Model, the Z-pole data are also used to predict the mass of the top quark, $M_t = 173^{+13}_{-10}$ GeV/c^2. This indirect constraint is compared to the direct measurement [22] $M_t = 173.5 \pm 0.6 \pm 0.8$ GeV/c^2, providing a stringent test of the Standard Model.

One way of presenting the combined results of the precision measurements of the Standard Model parameters is the global SM fit to electroweak precision data. The latest fit by the `Gfitter Group` [40] includes the mass of the new boson discovered at the LHC assuming it is the SM Higgs. The pull comparison of the fit results with the direct measurements in units of the experimental uncertainty is shown in Fig. 3.1. The input values and fit results for the observables and parameters of the global electroweak fit is shown in Tab. 3.2. The m_H mass measurement of ATLAS and CMS agree within 1.3σ with the indirect determination $m_H = 94^{+25}_{-22}$ GeV.

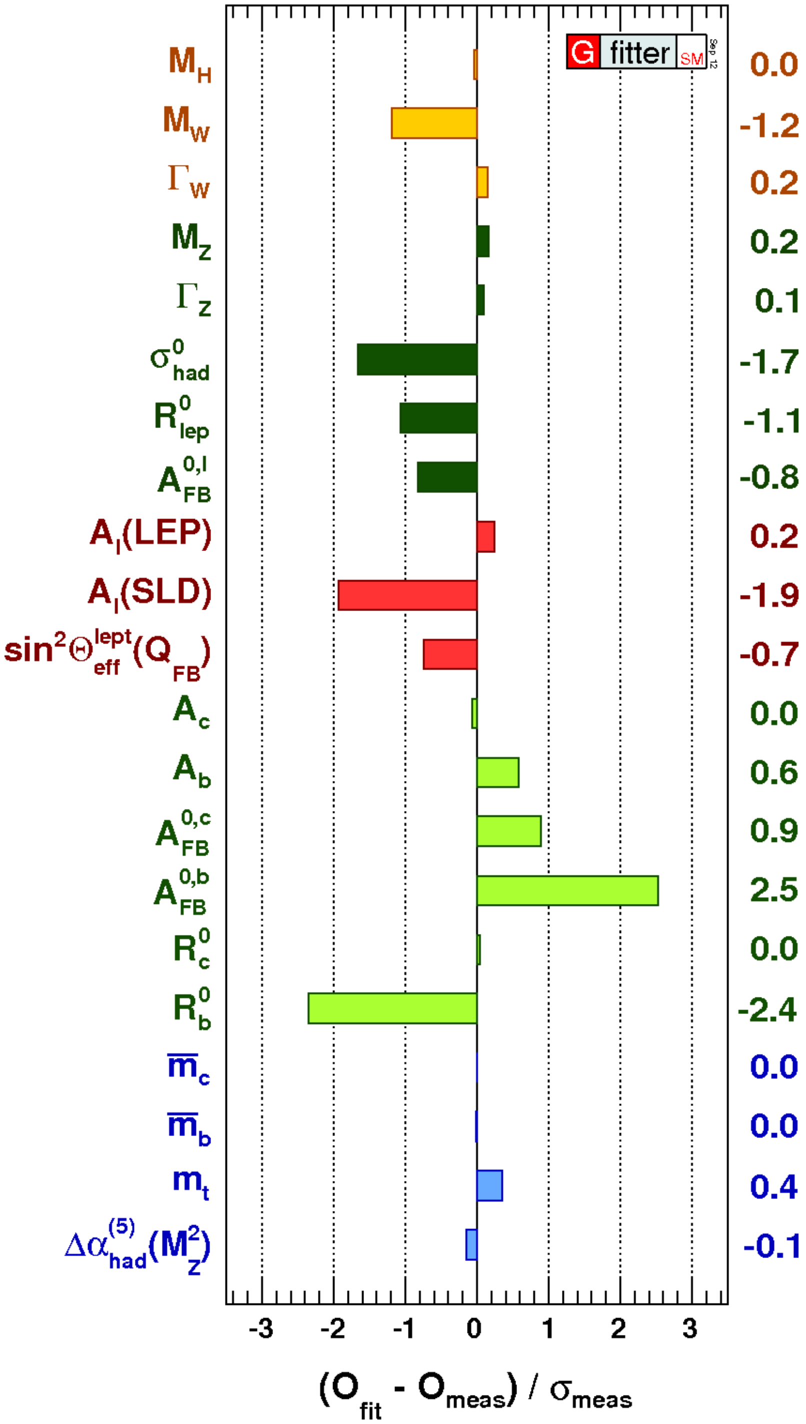

Figure 3.1: Pull comparison of the fit results with the direct measurements in units of the experimental uncertainty [40].

Parameter	Input value	Free in fit	Fit result incl. M_H	Fit result not incl. M_H	Fit result incl. M_H but not exp. input in row
M_H [GeV]$^{(\circ)}$	125.7 ± 0.4	yes	125.7 ± 0.4	94^{+25}_{-22}	94^{+25}_{-22}
M_W [GeV]	80.385 ± 0.015	–	80.367 ± 0.007	80.380 ± 0.012	80.359 ± 0.011
Γ_W [GeV]	2.085 ± 0.042	–	2.091 ± 0.001	2.092 ± 0.001	2.091 ± 0.001
M_Z [GeV]	91.1875 ± 0.0021	yes	91.1878 ± 0.0021	91.1874 ± 0.0021	91.1983 ± 0.0116
Γ_Z [GeV]	2.4952 ± 0.0023	–	2.4954 ± 0.0014	2.4958 ± 0.0015	2.4951 ± 0.0017
σ^0_{had} [nb]	41.540 ± 0.037	–	41.479 ± 0.014	41.478 ± 0.014	41.470 ± 0.015
R^0_ℓ	20.767 ± 0.025	–	20.740 ± 0.017	20.743 ± 0.018	20.716 ± 0.026
$A^{0,\ell}_{\mathrm{FB}}$	0.0171 ± 0.0010	–	0.01627 ± 0.0002	0.01637 ± 0.0002	0.01624 ± 0.0002
$A_\ell\ ^{(\star)}$	0.1499 ± 0.0018	–	$0.1473^{+0.0006}_{-0.0008}$	0.1477 ± 0.0009	$0.1468 \pm 0.0005^{(\dagger)}$
$\sin^2\theta^\ell_{\mathrm{eff}}(Q_{\mathrm{FB}})$	0.2324 ± 0.0012	–	$0.23148^{+0.00011}_{-0.00007}$	$0.23143^{+0.00010}_{-0.00012}$	0.23150 ± 0.00009
A_c	0.670 ± 0.027	–	$0.6680^{+0.00025}_{-0.00038}$	$0.6682^{+0.00042}_{-0.00035}$	0.6680 ± 0.00031
A_b	0.923 ± 0.020	–	$0.93464^{+0.00004}_{-0.00007}$	0.93468 ± 0.00008	0.93463 ± 0.00006
$A^{0,c}_{\mathrm{FB}}$	0.0707 ± 0.0035	–	$0.0739^{+0.0003}_{-0.0005}$	0.0740 ± 0.0005	0.0738 ± 0.0004
$A^{0,b}_{\mathrm{FB}}$	0.0992 ± 0.0016	–	$0.1032^{+0.0004}_{-0.0006}$	0.1036 ± 0.0007	0.1034 ± 0.0004
R^0_c	0.1721 ± 0.0030	–	0.17223 ± 0.00006	0.17223 ± 0.00006	0.17223 ± 0.00006
R^0_b	0.21629 ± 0.00066	–	0.21474 ± 0.00003	0.21475 ± 0.00003	0.21473 ± 0.00003
$\overline{m}_c$ [GeV]	$1.27^{+0.07}_{-0.11}$	yes	$1.27^{+0.07}_{-0.11}$	$1.27^{+0.07}_{-0.11}$	–
$\overline{m}_b$ [GeV]	$4.20^{+0.17}_{-0.07}$	yes	$4.20^{+0.17}_{-0.07}$	$4.20^{+0.17}_{-0.07}$	–
m_t [GeV]	173.18 ± 0.94	yes	173.52 ± 0.88	173.14 ± 0.93	$175.8^{+2.7}_{-2.4}$
$\Delta\alpha^{(5)}_{\mathrm{had}}(M_Z^2)\ ^{(\triangle\triangledown)}$	2757 ± 10	yes	2755 ± 11	2757 ± 11	2716^{+49}_{-43}
$\alpha_S(M_Z^2)$	–	yes	0.1191 ± 0.0028	0.1192 ± 0.0028	0.1191 ± 0.0028
$\delta_{\mathrm{th}} M_W$ [MeV]	$[-4, 4]_{\mathrm{theo}}$	yes	4	4	–
$\delta_{\mathrm{th}} \sin^2\theta^\ell_{\mathrm{eff}}\ ^{(\triangle)}$	$[-4.7, 4.7]_{\mathrm{theo}}$	yes	-1.4	4.7	–

$^{(\circ)}$Average of ATLAS ($M_H = 126.0 \pm 0.4\ (\mathrm{stat}) \pm 0.4\ (\mathrm{sys})$) and CMS ($M_H = 125.3 \pm 0.4\ (\mathrm{stat}) \pm 0.5\ (\mathrm{sys})$) measurements assuming no correlation of the systematic uncertainties. $^{(\star)}$Average of LEP ($A_\ell = 0.1465 \pm 0.0033$) and SLD ($A_\ell = 0.1513 \pm 0.0021$) measurements, used as two measurements in the fit. $^{(\dagger)}$The fit w/o the LEP (SLD) measurement gives $A_\ell = 0.1474^{+0.0005}_{-0.0009}$ ($A_\ell = 0.1467^{+0.0006}_{-0.0004}$). $^{(\triangle)}$In units of 10^{-5}. $^{(\triangledown)}$Rescaled due to α_S dependency.

Table 3.2: Input values and fit results for the observables and parameters of the global electroweak fit. The first and second columns list respectively the observables/parameters used in the fit, and their experimental values or phenomenological estimates. The subscript "theo" labels theoretical error ranges. The third column indicates whether a parameter is floating in the fit. The fourth column quotes the results of the complete fit including all experimental data. The fifth column gives the fit results for each parameter without using the m_H measurement in the fi. In the last column the fit results are given without using the corresponding experimental or phenomenological estimate in the given row [40].

3.7 Incompleteness of the Standard Model

In spite of the fact that the Standard Model has been tested in a high precision level, it is not expected to be the final description of the fundamental interactions, but rather an effective low-energy manifestation of a more complete theory [41]. There are still outstanding issues concerning the SM:

- **Electroweak symmetry breaking mechanism**: The Standard Model implements the Higgs mechanism via a single weak-isospin doublet with a non–zero vacuum expectation value in order to generate the gauge boson masses, but this is not the only possible way in which the electroweak symmetry can be broken. The new Higgs-like resonance announced by CERN experiments CMS and ATLAS in July 4th 2012 [28, 27] has to undergo tests to see its compatibility with the Standard Model Higgs. This includes the total cross section, the relative fractions of the decay channels, and a spin measurement.

- **The hierarchy problem**: The Higgs mass has divergent quantum loop corrections, expanding in perturbation theory as:

  $$m_H^2(p^2) = m_{0,H}^2 + \mathcal{C}g^2 \int_{p^2}^{\Lambda^2} dk^2 + \cdots \tag{3.24}$$

  where $m_{0,H}^2$ is the tree-level classical contribution to the Higgs mass squared, g is the coupling constant on the theory, $\mathcal{C}$ is a model-dependent constant, and Λ is the reference scale up to which the SM is assumed to remain valid. The integrals represent contributions at loop level and are quadratically divergent. If there is no new physics, the reference scale is high, like the Planck scale, $\Lambda \sim M_{Pl} \approx 10^{19}$ GeV or, in Grand Unified Theories (GUTs), $\Lambda \sim M_{GUT} \approx 10^{15} - 10^{16}$ GeV. Both choices result in large corrections to the Higgs mass. In order to be small, either there is a fine tuning in the loop contributions or there is another mechanism (like supersymmetry or extra dimensions) that protects the Higgs mass.

- **Vacuum energy problem**: The problem, also called the cosmological constant problem, is the same as the hierarchy problem, but considering operators of dimension 0 (vacuum energy) instead of dimension 2 (Higgs mass). It consists of a discrepancy between theory and experiment, of 60 to 120 orders of magnitude, arising from the Standard Model and General Relativity (GR), in a regime where both theories have been reliably and precisely tested and hence cannot be dramatically modified. In the field equation for GR,

$$R_{\mu\nu} - \frac{1}{2}Rg_{\mu\nu} + \Lambda g_{\mu\nu} = 8\pi G T_{\mu\nu}, \tag{3.25}$$

there is an ambiguity: Λ, the cosmological constant, is not determined by the theory structure, and there is no satisfactory reason to set it to zero. However, a non-vanishing value of Λ introduces a length scale and time scale into GR, $r_\Lambda = ct_\Lambda = \sqrt{3/|\Lambda|}$. The Planck length is an independent length scale which arises from the constants of Nature, $l_{Pl} = \sqrt{G\hbar/c^3} \approx 1.616 \times 10^{-33}$ cm. Experimentally, the cosmological constant has to be small in units of the the Planck scale (i.e., r_Λ is large in natural units). This can also be deduced from the fact that the Planck length is small compared to the size of the universe, and the universe is old compared to the Planck time. Because Λ is so small, it is tempting to set it to zero in the Einstein equation; and this works well at the level of classical gravity. However, in Eq 3.25, the Λ term is not the only one proportional to the metric. Another, much more problematic contribution enters through the stress tensor on the right hand side.

In quantum field theory, the vacuum is nontrivial, and have an energy density; the energy-momentum stress tensor is proportional to the metric, $< T_{\mu\nu} >= -\rho_{\text{vacuum}}\, g_{\mu\nu}$. The vacuum energy has the form of a cosmological constant, and Λ can be redefined as $\Lambda = \Lambda_{\text{Einstein}} + 8\pi\rho_{\text{vacuum}}$. Equivalently, $\Lambda_{\text{Einstein}}$ can be absorbed into the density energy of the vacuum, $\rho_\Lambda \equiv \rho_{\text{vacuum}} + \Lambda_{\text{Einstein}}/8\pi$. From the GR equations, the empirical bound on the total energy density of the vacuum is $|\rho_\Lambda| \lesssim 10^{-121}$. But in the SM, this value is enormous even with a conservative cutoff, as there are multiple perturbative contributions to $|\rho_\Lambda|$, each 60 to 120 orders of magnitude larger than the experimental bound based on GR [42].

- **Broken flavor symmetry**: Part of the flavor problem in the SM is the widely different mass assignments of the fermions attributed to the Yukawa couplings, which also set the mixing angles between flavor and mass eigenstates. Mixing occurs in both quark and lepton sectors (parametrized by the Cabibbo-Kobayashi-Maskawa and Maki-Nakagawa-Sakata matrices, respectively), and while the off-diagonal elements in the quark sector are rather small ($\sim 10^{-1} - 10^{-3}$) so there is little mixing between the quark families, in the lepton sector the off-diagonal elements (except $[V_{MNS}]_{e3}$) are of order 1, so the mixing between families is large. The SM does not provide an explanation for this difference.

- **Dark matter**: There are evidences that the dark matter makes up to $\sim 25\%$ of the energy density of the universe [43]. Structure formation indicates that dark matter should be cold at the time of its formation. There are no candidates as such in the SM. Within the Minimal Supersymmetric extension of the Standard Model (MSSM), the lightest supersymmetric particle, called a neutralino, is a popular dark matter candidate.
- **Baryon asymmetry**: The antibaryon density of the universe is negligible. In a cosmological model with inflation, conventional thermal equilibrium processes would have yielded an equal number of particles and antiparticles. However, the CP violation observed so far, which is described by the Kobayashi–Maskawa mechanism of the Standard Model, is known to be insufficient to explain the observed discrepancy of matter anti-matter and new physics is needed. One possible solution lies in leptogenesis scenarios, where the baryon asymmetry is a result of a previously existing lepton asymmetry generated by the decay of heavy sterile neutrinos [44].
- **Electric charge quantization**: The charges of all observed particles are simple multiples of a fundamental charge, which can be taken as the electron charge. The charge quantization can be explained by the presence of a single magnetic monopole, but so far no indication of existence of such a particle was found. An alternative route to explain the lack of experimental evidence for magnetic monopoles would be the GUT — in such theories, magnetic monopoles exists but are so massive that their cosmological density would be suppressed to a not observable small value by cosmological inflation.
- **Quantum gravity**: The Standard Model does not incorporate gravity, which is classically described by the theory of General Relativity. However, for the consistency of our physical theories, a quantum theory of gravity is required. The main issue trying to build such theories is the non–renormalizability. String theory and loop quantum gravity constitute attempts at building a quantized theory of gravity.

Several theories Beyond the Standard Model (BSM) were formulated to try to explain the deficiencies and incompleteness of the Standard Model. Extra dimensions, Supersymmetry, Technicolor, Little Higgs, Hidden Valleys, are just some examples of the large variety of new theoretical developments available in order to address the issues discussed in this section.

Chapter 4

Extra Dimensions

There is not an explanation in the framework of the Standard Model why the weak force is 10^{32} times stronger than gravity: the Planck scale, in which the quantum effects of gravity would become observable, is in the order of 10^{19} GeV, while the electroweak scale is about 250 GeV. The solution of this dilemma can be an important guide to the construction of new models beyond the Standard Model.

In General Relativity (GR), the Planck scale appears as a natural theory regulator. However, if this same cutoff is set for the field theory describing all interactions, problems in the Higgs mass arise from loop corrections. The sensitivity of the dressed Higgs boson mass to the theory cutoff can be solved by either fine tuning of the physical constants or by new physics to cancel the divergent loop corrections. Mathematically,

$$(m_H^{Ren})^2 = (m_{0,H})^2 + \delta m_H^2 \leq (\mathrm{TeV})^2 \,, \tag{4.1}$$

$$\delta m_H^2 \sim \int_0^{\Lambda_{UV}} \frac{d^4k}{k^2} \sim \Lambda_{UV}^2 \,. \tag{4.2}$$

Equation 4.2 shows that the correction to the tree-level Higgs mass ($m_{0,H}$) is proportional to the square of the ultraviolet cutoff, making the physical (renormalized) Higgs mass to become very large if the theory cutoff is in the Planck scale,

$$\Lambda_{\mathrm{UV}} \sim M_{Pl} \ \rightarrow (m_H^{Ren})^2 \gg (\mathrm{TeV})^2 \,. \tag{4.3}$$

Some of the possibilities to solve the hierarchy problem include Higgs compositeness, supersymmetry and spacial extra dimensions. The later will be the focus of this thesis.

The Newton gravitational force behaves as $\sim r^{-2}$. Direct gravitational tests of this behavior are carried out only up to 80 μm in torsion balance experiments [45]. Gravitational effects that differ from Newton's law for distances smaller than this limit are not experimentally discarded.

Extra spacial dimensions can solve the hierarchy problem by allowing gravity to show quantum effects already at the TeV scale. Generally, for N flat extra dimensions, the gravitational force behaves as,

$$F_{Newton} \sim r^{-(2+N)} . \tag{4.4}$$

One way to parametrize this difference is considering massive gravitons contributing to the force, in a Yukawa description with range parameter λ and strength α, with $V_N(r)$ being the Newtonian potential,

$$V_N(r) \sim r^{-1};\ V(r) = V_N(r)\left(1 + \alpha e^{-r/\lambda}\right) . \tag{4.5}$$

The current limits on the parameters α and λ are shown in Fig 4.1. The strength parameter α compares the magnitude of the new effect compared to the regular gravity. The parameter λ is the length scale above which the interaction has r^{-2} character. At short ranges, the experimental sensitivity falls off roughly as λ^4. The region below 1 mm has been the subject of intense research because of its large potential for observing new physics

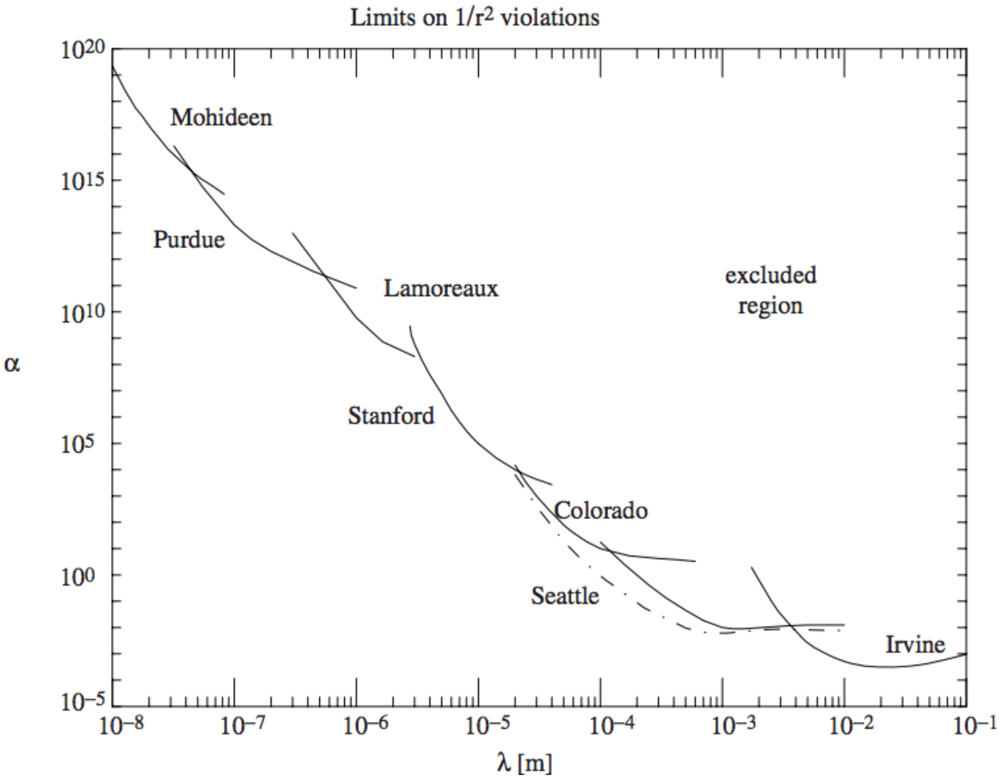

Figure 4.1: 2σ limits on r^{-2} violations of gravitational force. The violation is described as a new interaction that has the form of a Yukawa interaction [45].

Extra dimensions were not observed (so far) and, therefore, the models have to explain why its effects do not appear in our current understanding of Nature. One alternative is to compactify the extra dimension, like in the Randall–Sundrum I model [4], or in the case of the Calabi–Yau manifolds of superstring theory [46]. Another alternative is to consider an infinite extra dimension, like in the Randall-Sundrum II model [5] and, at the same time, localize the Standard Model particles in one four dimensional brane.

The new massive gravitons are usually implemented in the extra dimensions theories using the Kaluza–Klein mechanism. The qualitative idea is very simple: the relativistic relation between energy and momentum, in five dimensions, is given by:

$$5D \rightarrow P^A P_A = P^\mu P_\mu - P_5^2 = m^2 \; . \tag{4.6}$$

An observer in 4 dimensions will measure the same relation as:

$$4D \rightarrow P^\mu P_\mu = P_5^2 + m^2 \; . \tag{4.7}$$

Thus, the momentum in the extra dimension P_5 will be observed as an additive term in the mass of the particle observed in 4 dimensions, and the mass will vary according to the momentum in the extra dimension. If there is a boundary condition in the 5-th component (*i.e.* the extra dimension is compact), the momentum P_5 will be quantized. This gives rise to discrete mass states in 4 dimensions, known as the Kaluza–Klein towers.

Quantitatively, for quantum fields in $4+i$ dimensions, one can expand any field function $\Phi(x^\mu, y^i)$ by parametrizing in the 4 dimension coordinates and in the extra coordinates i,

$$\Phi(x^\mu, y^i) = \frac{1}{\sqrt{V}} \sum_n \phi^{(n)}(x^\mu) f_n(y^i) \; , \tag{4.8}$$

where the index μ runs over the usual 4-dimensional coordinates ($\mu = 0, 1, 2, 3$), $\{f_n(y^i)\}$ is a complete set of functions used to parametrize the y^i coordinates in the compact space of the extra dimensions, and $\phi^{(n)}(x^\mu)$ is the n–th Kaluza Klein mode. Choosing an orthonormal basis,

$$\langle f_n | f_m \rangle = \delta_{nm} \; , \tag{4.9}$$

allows to think of the $\phi^{(n)}(x^\mu)$ as independent degrees of freedom. The functions

$\phi^{(n)}(x^\mu)$ and $\{f_n(y^i)\}$ chosen for the expansion will depend on the generalized metric of the model and are, in general, eigenfunctions of the free theory.

To demonstrate the procedure in the simplest case, consider a massive scalar field, with one flat extra dimension which gets compactified in a cylinder of radius R. In this situation, the boundary conditions are periodic,

$$y \to y + 2\pi R\ ; \quad V = 2\pi R\ ; \quad \Phi(x^\mu, y) = \Phi(x^\mu, y + 2\pi R)\ . \tag{4.10}$$

The 5–dimensional action of a complex scalar field ϕ is given by:

$$S_5 = \int d^4x \int_0^{2\pi R} dy \left[\frac{1}{2}\left(\partial_\mu \phi\right)^* \left(\partial^\mu \phi\right) - \frac{1}{2} m_0^2 \phi^* \phi\right]\ . \tag{4.11}$$

The Kaluza-Klein expansion is then given by:

$$\Phi(x^\mu, y) = \frac{1}{\sqrt{2\pi R}} \sum_{n=-\infty}^{\infty} \Phi_n(x^\mu) \exp\left(\frac{iny}{R}\right)\ . \tag{4.12}$$

Substituting the expansion from Eq. 4.12 into action in Eq. 4.11,

$$\begin{aligned} S_5 = \int d^4x \int_0^{2\pi R} dy &\left[\frac{1}{2}\sum_{m,n} \partial_\mu \phi_m^* \partial^\mu \exp\left(\frac{i(n-m)y}{R}\right)\right] \\ &- \frac{1}{2}\sum_{m.n}\left(\frac{-im}{R}\right)\left(\frac{in}{R}\right)\phi_m^*\phi_n \exp\left(\frac{i(n-m)y}{R}\right) \\ &- \frac{1}{2} m_0^2 \sum_{m,n} \phi_m^* \phi_n \exp\left(\frac{i(n-m)y}{R}\right)\ . \end{aligned} \tag{4.13}$$

Using the orthogonality relation:

$$\int_0^{2\pi R} dy\ \exp\left(\frac{i(n-m)y}{R}\right) = 2\pi R \delta_{mn}\ , \tag{4.14}$$

the integral in the extra dimension can be performed, and the effective action in 4–dimensions is given by:

$$S_4 = \int d^4x \left[\frac{1}{2}\sum_n \left(\partial_\mu \phi_n^*\right)\left(\partial^\mu \phi_n\right) - \frac{1}{2}\sum_n \left(m_0^2 + \frac{n^2}{R^2}\right)\phi_n^* \phi_n\right], \tag{4.15}$$

where the mass of the n–ith Kaluza-Klein mode is given by:

$$m_n^2 = m_0^2 + \frac{n^2}{R^2} \; . \tag{4.16}$$

This simple example shows the procedure to obtain the effective action in four dimensions of a higher dimensional theory, and it can be applied to more complicated configurations.

4.1 The Randall-Sundrum Model

Randall–Sundrum models — also called 5-dimensional warped geometry theory — suggest that the universe has one extra spatial dimension and is described by a warped geometry. More concretely, our Universe is a five-dimensional anti–de Sitter space and the elementary particles, except for the graviton, are localized on a $(3+1)-$dimensional brane(s).

The models were proposed in 1999 by Lisa Randall and Raman Sundrum [4, 5]. Later, while studying RS models in the context of the AdS/CFT correspondence, they showed how it can be dual to technicolor models. There are two popular versions of the model. The first, called RSI, has a finite size for the extra dimension with two branes, one at each end. The second, RSII, is similar to the first, but one brane has been placed infinitely far away, so that there is only one brane left in the model.

In RSI models, the Standard Model particles live only on the *visible* or *weak* 4 dimensional brane while gravity is mostly at the *gravitational* or *Planck* brane but also extends into the bulk. The hierarchy between the electroweak and Planck scales is generated by the curvature in the extra dimension, and the energies of the order of Planck scale in the gravitational brane are exponentially suppressed along the extra dimension, and arise in the weak brane in the TeV scale.

To build the model, the Einstein's equation is solved in 5 dimensions. Poincaré invariance in 4 dimensions (*i.e.* x^μdirection) is imposed. One 5 dimensional metric satisfying this ansatz has the form,

$$ds^2 = e^{-2kr_C|\phi|}\eta_{\mu\nu}dx^\mu dx^\nu + r_C^2 d\phi^2, \;\; 0 \leq |\phi| \leq \pi \; . \tag{4.17}$$

The r_C coefficient is independent of the 5th dimension coordinate and corresponds to the extra dimension radius prior to orbifolding. The scale k is of order of the Planck scale and relates the 5 dimensional Planck scale M to the cosmological constant. The metric in Eq. 4.17 is non–factorizable. The two branes have opposite tensions, and are located in the two fixed points of the orbifold S_1/Z_2.

The reduced Planck scale $\overline{M}_{Pl}$ in 4 dimensions is given by:

$$\overline{M}_{Pl}^2 = \frac{M^3}{k}\left(1 - e^{-2kr_C\pi}\right) . \tag{4.18}$$

Thus, Eq. 4.18 shows that the Planck scale is not very affected by the exponential term. However, assuming the weak brane is located at $|\phi| = \pi$, the physical masses of the effective theory in 4 dimensions with fundamental mass parameter m_0 is given by,

$$m = m_0\, e^{-kr_C\pi} , \tag{4.19}$$

which requires $kr_C \sim 12$ to solve the hierarchy problem.

To get the Kaluza-Klein modes in warped metrics, a linear expansion of the metric around its Minkowski value is performed [47],

$$\hat{G}_{\alpha\beta} = e^{-2\sigma}(\eta_{\alpha\beta} + \kappa^* h_{\alpha\beta}) , \tag{4.20}$$

where κ^* is the expansion parameter.

In order to obtain the mass spectrum of the tensor fluctuations, consider the 4 dimensional $\alpha\beta$ components of Einstein's equation with the replacement $G_{\alpha\beta} \to \hat{G}_{\alpha\beta}$, keeping terms up to O($\kappa^*$). Working in the gauge where $\partial^\alpha h_{\alpha\beta} = 0 = h^\alpha_\alpha$, upon compactification the graviton field $h_{\alpha\beta}$ is expanded into a KK tower,

$$h_{\alpha\beta}(x,\phi) = \sum_{n=0}^{\infty} h^{(n)}_{\alpha\beta}(x)\frac{\chi^{(n)}(\phi)}{\sqrt{r_C}} , \tag{4.21}$$

where the $h^{(n)}_{\alpha\beta}(x)$ correspond to the KK modes of the graviton on the background of Minkowski space on the brane. $\eta^{\alpha\beta}$ satisfy,

$$\eta^{\alpha\beta}\partial_\alpha h^{(n)}_{\beta\gamma} = 0 ,$$

$$\eta^{\alpha\beta} h^{(n)}_{\alpha\beta} = 0 .$$

The equation of motion for $h^{(n)}_{\alpha\beta}$ is given by:

$$\left(\eta^{\alpha\beta}\partial_\alpha\partial_\beta - m_n^2\right) h^{(n)}_{\mu\nu}(x) = 0 . \tag{4.22}$$

Equation 4.22 corresponds to the states with masses $m_n \geq 0$. Using the KK expansion for $h_{\alpha\beta}$ in $\hat{G}_{\alpha\beta}$, Einstein's equation in conjunction with the equation of motion yields the differential equation for $\chi^{(n)}(\phi)$:

$$\frac{-1}{r_C^2}\frac{d}{d\phi}\left(e^{-4\sigma}\frac{d\chi^{(n)}}{d\phi}\right) = m_n^2 e^{-2\sigma}\chi^{(n)} \, . \tag{4.23}$$

The orthonormality condition for $\chi^{(n)}$ is

$$\int_{-\pi}^{\pi} d\phi e^{-2\sigma}\chi^{(m)}\chi^{(n)} = \delta_{mn} \, .$$

In deriving Eq. 4.23, it was used that

$$\left(\frac{d\sigma}{d\phi}\right)^2 = (kr_C)^2 \quad \text{and} \quad \frac{d^2\sigma}{d\phi^2} = 2kr_C[\delta(\phi) - \delta(\phi - \pi)] \, ,$$

as required by the orbifold symmetry for $\phi \in [-\pi, \pi]$. The solutions for $\chi^{(n)}$ are given by [48]:

$$\chi^{(n)}(\phi) = \frac{e^{2\sigma}}{N_n}[J_2(z_n) + \alpha_n Y_2(z_n)] \, , \tag{4.24}$$

where J_2 and Y_2 are Bessel functions of order 2, N_n represents the wavefunction normalization, α_n are constant coefficients, and

$$z_n(\phi) = \frac{m_n e^{\sigma(\phi)}}{k} \, .$$

Defining $x_n \equiv z_n(\pi)$ and working in the limit that $m_n/k \ll 1$ and $e^{kr_C\pi} \gg 1$, the requirement that the first derivative of $\chi^{(n)}$ be continuos at the orbifold fixed points yield $a_n \sim x_n^2 e^{-2kr_C\pi}$ and $J_1(x_n) = 0$, so that the x_n are simply roots of the Bessel function of order 1.

In this way the masses of the graviton KK excitations are given by

$$m_n = kx_n e^{-kr_c\pi} \, ,$$

and depends on the roots of J_1 which are not equally spaced, in contrast to most KK models with one extra dimension.

For $x_n \ll e^{kr_C\pi}$, we see that $\alpha_n \ll 1$, and hence $Y_2(z_n)$ can be neglected compared to $J_2(z_n)$ in Eq. 4.24. Thus, the normalization is given by Eq. 4.25, and the normalization of the zero mode is simply $N_0 = 1/\sqrt{kr_c}$, and,

$$N_n \simeq \frac{e^{kr_c\pi}}{\sqrt{kr_c}} J_2(x_n) \; ; \; n > 0 \; . \tag{4.25}$$

Having found the solutions for $\chi^{(n)}$, the interactions of $h^{(n)}_{\alpha\beta}$ with the matter field in the brane can be derived. Starting with the 5 dimensional action and imposing the constraint that the Standard Model fields are confined in the brane at $\phi = \pi$, the usual form of the interaction Lagrangian in the 4-dimensional effective theory is given by:

$$\mathcal{L} = -\frac{1}{M^{3/2}} T^{\alpha\beta}(x) h_{\alpha\beta}(x, \phi = \pi) \; , \tag{4.26}$$

where $T_{\alpha,\beta}$ represents the symmetric conserved Minkowski space energy-momentum tensor of the matter fields and $\kappa^* = 2/M^{3/2}$.

Expanding the graviton field into the KK states of Eq. 4.21 and using the normalization in Eq. 4.25 for $\chi^{(n)}(\phi)$, the Lagrangian is,

$$\mathcal{L} = -\frac{1}{\overline{M}_{Pl}} T^{\alpha\beta}(x) h^{(0)}_{\alpha\beta}(x) - \frac{1}{\Lambda_\pi} T^{\alpha\beta}(x) \sum_{n=1}^{\infty} h^{(n)}_{\alpha\beta}(x) \; . \tag{4.27}$$

From Eq. 4.27 one can see that the zero mass mode (long distance gravity) has the coupling suppressed by a factor of the order of magnitude of Planck mass. For the massive Kaluza–Klein modes, the coupling is proportional to the inverse of Λ_π in the TeV scale. Thus, the massive modes cross sections are high enough to be produced and seen in accelerators that can reach the TeV scale, such as the LHC.

4.1.1 Resonant Production Cross Section

The gravitons can, in principle, be detected through its resonant production. As an example, we present below the resonant cross section for RS graviton production in fermion–antifermion collisions (*e.g.*, electron-positron, quark-antiquark) or gluon–gluon fusion. For calculating the cross section of the RS graviton resonant production, it is necessary to evaluate the decay width of the graviton in each of the Standard Model particles. This calculation can be carried out using the Feynman rules taken from the Lagrangian (Eq. 4.27).

The on–shell resonant production cross section can be described by a Breit-

Wigner given by [22]:

$$\sigma_{BW} = \frac{(2J+1)}{(2S_1+1)(2S_2+1)} \frac{4\pi}{k^2} \left[\frac{M^2\Gamma^2}{(s-M^2)^2 + M^2\Gamma^2} \right] B_{in} B_{out} , \tag{4.28}$$

where $J = 2$ is the spin of the resonance and M its mass, $2S_i + 1$ are the multiplicities of the incident spin states and $B_{in(out)}$ are the branching fractions of the resonance into the incoming and outgoing channels. From relativistic kinematics, the center–of–mass momentum k can be written as:

$$k^2 = \frac{\lambda(s, m^2, m^2)}{4s} = \frac{s(1-4m^2/s)}{4} . \tag{4.29}$$

Therefore, for the process $f\bar{f} \to f\bar{f}, VV, ...$, resonant production cross section can be written as:

$$\sigma_{BW} = \frac{5}{4} \frac{16\pi M^2}{s(1-4m_f^2/s)} \left[\frac{1}{(s-M^2)^2 + M^2\Gamma^2} \right] \Gamma_{in} \Gamma_{out} . \tag{4.30}$$

Equation 4.30 shows that the necessary quantities to calculate the resonant cross section are the decay width of the massive gravitons for the following processes:

- Production: $f\bar{f}, gg \to G_{KK}$
- Decays: $G_{KK} \to gg, VV, \gamma\gamma, \ell^+\ell^-, q\bar{q}$

For notation convention, G_{KK} is defined as the Kaluza-Klein excitations of the RS graviton and VV are a pair of massive vector bosons (ZZ or WW).

The decay width is given by:

$$\begin{aligned} d\Gamma &= \frac{S}{2M} |\mathcal{M}|^2 \prod_{i=1}^{n} \frac{d^3 p_i}{2E_i (2\pi)^3} (2\pi)^4 \delta^4 \left(p - \sum_{i=1}^{n} p_n \right) S \\ &= \frac{S}{2M} \frac{1}{(2\pi)^{3n-4}} |\mathcal{M}|^2 d\mathcal{R}_n . \end{aligned} \tag{4.31}$$

For identical particles in the final state $S = 1/2$ and $S = 1$ otherwise. For $1 \to 2$ processes in the graviton rest frame, the decay width is independent of angles; thus:

$$\begin{aligned} \Gamma &= \frac{S}{64\pi^2 M^3} \lambda^{1/2}(M^2, m^2, m^2) |\mathcal{M}|^2 d\Omega^* \\ &= \frac{S}{64\pi^2 M^3} 4\pi [M^2(M^2 - 4m^2)]^{1/2} |\mathcal{M}|^2 . \end{aligned} \tag{4.32}$$

4.1.2 Decay Widths

Fermions

The Feynman rule for fermions is given by Eq. 4.33 and Fig. 4.2.

$$h_{\mu\nu}\bar{\psi}\psi : \quad \frac{-i\kappa}{8}\left[\gamma^{\mu}(k_1^{\nu}+k_2^{\nu})+\gamma_{\nu}(k_1^{\mu}+k_2^{\mu})-2\eta_{\mu\nu}(k_1+k_2-2m)\right] \tag{4.33}$$

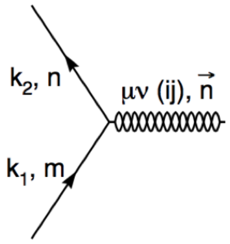

Figure 4.2: Vertex for the graviton coupling to a fermion pair.

For the decay $G_{KK}(q) \to \psi(k_1) + \bar{\psi}(k_2)$, the invariant amplitude is written as:

$$\begin{aligned}\mathcal{M} &= \left(\frac{-i\kappa}{8}\right)\epsilon_{\mu\nu}(q)\ . \\ &. \ \bar{u}(k_1)\left[\gamma^{\mu}(k_1^{\nu}-k_2^{\nu})+\gamma^{\nu}(k_1^{\mu}-k_2^{\mu})-2\eta^{\mu\nu}(k_1-k_2-2m)\right]v(k_2)\ .\end{aligned} \tag{4.34}$$

Detailed calculations are carried out in Appendix A.1.

The final expression for the decay width $\Gamma(G_{KK} \to f\bar{f})$ is given by:

$$\Gamma(G_{KK} \to f\bar{f}) = N_C\frac{\kappa^2 m_G^3}{320\pi}\left(1-4\frac{m_f^2}{m_G^2}\right)^{3/2}\left(1+\frac{8}{3}\frac{m_f^2}{m_G^2}\right)\ . \tag{4.35}$$

In Eq. 4.35, m_G is mass of the first Kaluza-Klein graviton (G_{KK}), m_f is the fermion mass and N_C is the number of colors (3 for quarks and 1 for leptons). The factor κ, in Randall–Sundrum theory, is given by:

$$\kappa = \frac{\sqrt{2}x_1 k}{\overline{M}_{Pl}m_G}\ . \tag{4.36}$$

This leads to the cross sections of $f\bar{f} \to f\bar{f}$ with the exchange of a graviton

G_{KK},

$$\begin{aligned}\sigma(f\bar{f} \to f\bar{f}) =& \frac{5}{4}\frac{16\pi m_G^2}{s(1-4m_f^2/s)}\left[\frac{1}{(s-m_G^2)^2+m_G^2\Gamma^2}\right] \times \\ & \times \left[N_C\left(\frac{\kappa^2 m_G^3}{320\pi}\right)\left(1-4\frac{m_f^2}{m_G^2}\right)^{3/2}\left(1+\frac{8}{3}\frac{m_f^2}{m_G^2}\right)\right]^2 .\end{aligned} \tag{4.37}$$

Vector bosons

The Feynman rule for vector bosons is given by Eq. 4.38 and Fig. 4.3.

$$h_{\mu\nu}VV : \quad \frac{-i\kappa}{2}\left[(k_1.k_2+m^2)C_{\mu\nu,\alpha\beta}+D_{\mu\nu,\alpha\beta}\right] \tag{4.38}$$

In the unitary gauge ($\xi \to \infty$), C and D are given by:

$$C_{\mu\nu,\alpha\beta} = \eta_{\mu\alpha}\eta_{\nu\beta}+\eta_{\mu\beta}\eta_{\nu\alpha}-\eta_{\mu\nu}\eta_{\alpha\beta} , \tag{4.39}$$

and

$$D_{\mu\nu,\alpha\beta} = \eta_{\mu\nu}k_{1\beta}k_{2\alpha}-\left[\eta_{\mu\beta}k_{1\nu}k_{2\alpha}+\eta_{\mu\alpha}k_{1\beta}k_{2\nu}-\eta_{\alpha\beta}k_{1\mu}k_{2\nu}+(\mu\leftrightarrow\nu)\right] . \tag{4.40}$$

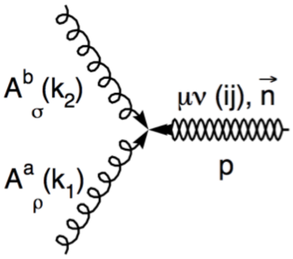

Figure 4.3: Vertex for the graviton coupling to a gauge boson pair.

For the decay $G_{KK}(q,\epsilon^{\mu\nu}) \to V(k_1,\epsilon^{\alpha})+V(k_2,\epsilon^{\beta})$, the invariant amplitude is written as,

$$\mathcal{M} = \frac{-i\kappa}{2}\left(\frac{M^2}{2}C_{\mu\nu,\alpha\beta}+D_{\mu\nu,\alpha\beta}\right)\epsilon^{\mu\nu}(q)\epsilon^{\alpha}(k_1)\epsilon^{\beta}(k_2) . \tag{4.41}$$

Detailed calculations are carried out in Appendix A.2.

The final expression for the decay width is given by,

$$\Gamma(G_{KK} \to V\bar{V}) = \delta\frac{\kappa^2 m_G^3}{80\pi}\left(1-4\frac{m_V^2}{m_G^2}\right)^{1/2}\left[\frac{13}{12}+\frac{14}{3}\frac{m_V^2}{m_G^2}+4\left(\frac{m_V^2}{m_G^2}\right)^2\right], \quad (4.42)$$

where $\delta = 0.5$ for Z and $\delta = 1$ for W bosons.

For the massless vector bosons, there is no longitudinal degree of freedom, which simplifies the calculations. The decay width for photons and gluons are,

$$\Gamma(G_{KK} \to \gamma\gamma) = \frac{\kappa^2 m_G^3}{160\pi}, \quad (4.43)$$

and

$$\Gamma(G_{KK} \to gg) = \frac{\kappa^2 m_G^3}{20\pi}. \quad (4.44)$$

Note that the gluon width is 8 times bigger due to the color factor.

This leads to the cross sections of $f\bar{f} \to V\bar{V}$ with the exchange of a graviton G_{KK}, plugging Eqs. 4.42, 4.43 and 4.44 into Eq. 4.28:

$$\begin{aligned}\sigma(f\bar{f} \to V\bar{V}) =& \frac{5}{4}\frac{16\pi m_G^2}{s(1-4m_f^2/s)}\left[\frac{1}{(s-m_G^2)^2+m_G^2\Gamma^2}\right]\times\\ &\times\left[N_C\left(\frac{\kappa^2 m_G^3}{320\pi}\right)\left(1-4\frac{m_f^2}{m_G^2}\right)^{3/2}\left(1+\frac{8}{3}\frac{m_f^2}{m_G^2}\right)\right]\times\\ &\times\left\{\delta\frac{\kappa^2 m_G^3}{80\pi}\left(1-4\frac{m_V^2}{m_G^2}\right)^{1/2}\left[\frac{13}{12}+\frac{14}{3}\frac{m_V^2}{m_G^2}+4\left(\frac{m_V^2}{m_G^2}\right)^2\right]\right\},\end{aligned} \quad (4.45)$$

and for the two–photon decay,

$$\begin{aligned}\sigma(f\bar{f} \to \gamma\gamma) =& \frac{5}{4}\frac{16\pi m_G^2}{s(1-4m_f^2/s)}\left[\frac{1}{(s-m_G^2)^2+m_G^2\Gamma^2}\right]\left(\frac{\kappa^2 m_G^3}{160\pi}\right)\times\\ &\times\left[N_C\left(\frac{\kappa^2 m_G^3}{320\pi}\right)\left(1-4\frac{m_f^2}{m_G^2}\right)^{3/2}\left(1+\frac{8}{3}\frac{m_f^2}{m_G^2}\right)\right],\end{aligned} \quad (4.46)$$

and for gluon final state,

$$\begin{aligned}\sigma(f\bar{f} \to gg) =& \frac{5}{4}\frac{16\pi m_G^2}{s(1-4m_f^2/s)}\left[\frac{1}{(s-m_G^2)^2+m_G^2\Gamma^2}\right]\left(\frac{\kappa^2 m_G^3}{20\pi}\right)\times \\ &\times\left[N_C\left(\frac{\kappa^2 m_G^3}{320\pi}\right)\left(1-4\frac{m_f^2}{m_G^2}\right)^{3/2}\left(1+\frac{8}{3}\frac{m_f^2}{m_G^2}\right)\right] .\end{aligned} \tag{4.47}$$

For obtaining the cross sections when the production is due to gluon fusion, the procedure is straightforward: using Eq. 4.28, and plugging in $\Gamma(G_{KK} \to gg)$ in Γ_{in}, which will change factor $5/4$, the second line in Eqs. 4.37, 4.45, 4.46 and 4.47. The cross section results obtained above are in agreement with the literature [49, 50].

4.2 Experimental Prospects

Direct searches in hadron colliders can constrain the allowed parameter space for the Randall–Sundrum extra dimension theory. The cleanest signal to be detected is the resonant production of the first Kaluza–Klein mode, in processes with dileptons in the final state ($q\bar{q}, gg \to G_{KK} \to l^+l^-$). Other possibilities are the dijet and diboson decay channels ($q\bar{q}, gg \to G_{KK} \to q\bar{q}, gg, VV$). The mass and width of the first massive graviton resonance are the only parameters needed to fully determine the model predictions. The curvature radius can be written as:

$$r_C = -\log\left(\frac{m_1}{kx_1}\right) \quad \text{with} \quad k = \overline{M}_{Pl}\left(\frac{\Gamma_1}{m_1\rho x_1^2}\right), \tag{4.48}$$

where x_1 is the first order Bessel function root, and ρ is a constant which depends on the open channels. Using these relations, the model parameters become,

$$\Lambda_\pi = \frac{m_1\overline{M}_{Pl}}{kx_1}; \quad \Gamma_1 = \rho m_1 x_1^2\left(\frac{k}{\overline{M}_{Pl}}\right)^2 . \tag{4.49}$$

The expected shape of the resonance varies according to the $k/\overline{M}_{Pl}$ parameter, and it can be seen in Fig. 4.4. Besides the theoretical limitation in the original Randall-Sundrum I formulation, where $k/\overline{M}_{Pl} \lesssim 0.1$ due to limits in the AdS$_5$ curvature, when the parameter gets above 0.3, the resonance no longer has a narrow shape. The spin 2 nature can be determined using angular correlations in the decay products, once enough signal data is accumulated. One way of doing the spin determination is illustrated in angular distribution presented in Fig. 4.5.

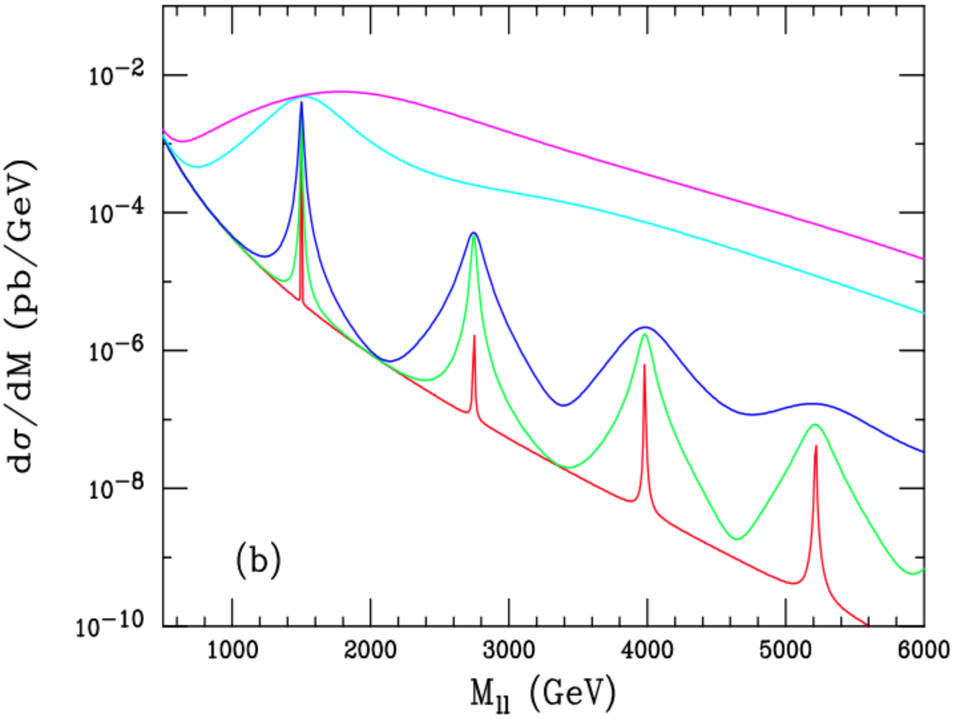

Figure 4.4: Drell-Yan production of a 1500 GeV/c^2 G_{KK} and its subsequent tower states at a 14 TeV LHC. From top to bottom, the curves are for $k/\overline{M}_{Pl}$ =1, 0.5, 0.1, 0.05, and 0.01, respectively [51].

The first direct searches limits were imposed by the Tevatron RunII. The focus were on signals with dileptons and diphotons in the final state: both CDF and DØ collaborations used the channels $G_{KK} \rightarrow e^+e^-, \mu^+\mu^-, \gamma\gamma$ [53, 54]. The latest limits used 5.4 fb^{-1} of integrated luminosity and excluded at 95% C.L. the graviton mass $m_G \geq 459$ (560) GeV/c^2 in CDF (DØ) collaborations for $k/\overline{M}_{Pl}$ =0.01. For $k/\overline{M}_{Pl} = 0.1$, the limits are $m_G \geq 963$ (1050) GeV/c^2 in CDF (DØ) collaborations.

The LHC have higher center of mass energy and luminosity, allowing its experiments (ATLAS and CMS collaborations) to reach better sensitivity to look for extra dimension models than those obtained by Tevatron. The ATLAS Collaboration searched for RSI gravitons in the dielectron and dimuon channels, with 1.08 and 1.21 fb^{-1} integrated luminosity, respectively. The 95% C.L. lower limit in the graviton mass is $m_G \geq 1.63$ TeV/c^2, for $k/\overline{M}_{Pl} = 0.1$ [55]. The CMS Collaboration holds the most restrictive limit in the mass of the graviton in the RSI model to date, in the diphoton channel. The 95% C.L. limit in the graviton mass is $m_G \geq$ 860 GeV/c^2, for $k/\overline{M}_{Pl} = 0.01$, and $m_G \geq 1.84$ TeV/c^2, for $k/\overline{M}_{Pl} = 0.1$ [56].

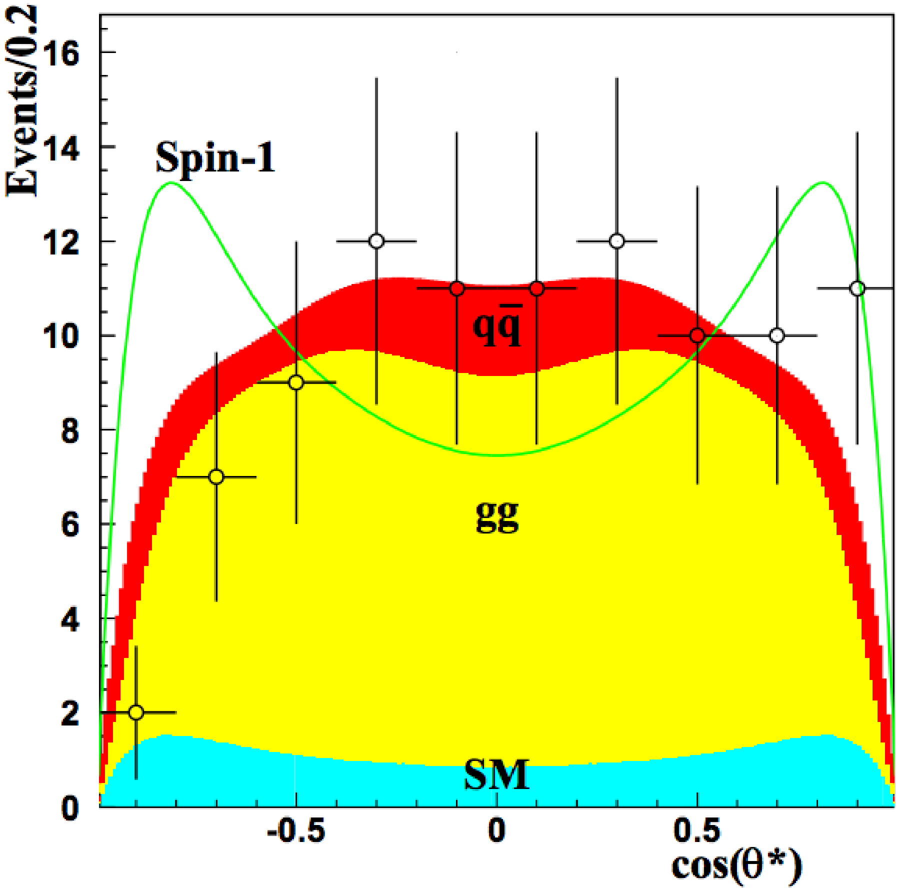

Figure 4.5: Angular distribution of simulated data (points with errors) in the test model for $m_G = 1.5$ TeV/c^2 and 100 fb^{-1} integrated luminosity. The stacked histograms show the contributions from the Standard Model (SM), gg production and $q\bar{q}$ production. The curve shows the distribution expected from a spin-1 resonance [52].

The searches in the vector boson channels (WW, ZZ) are not as competitive as the dilepton and diphoton results. However, this assumes a democratic RS model. In more recent studies [57], the Standard Model fields are allowed to propagate in the bulk, providing solution not only to the hierarchy problem but also to the flavor puzzle. In this scenario, the production via $q\bar{q}$ annihilation and decays to the conventional photon and lepton channels are highly suppressed. However, the graviton production via gluon fusion followed by decay to longitudinal Z/W can be significant; vector boson fusion is found to be a sub-dominant production mode. It is also argued that the ratio of the AdS$_5$ curvature to the Planck scale modestly above unity can still be within the regime of validity of the framework.

Chapter 5

Search for Exotic Resonances

5.1 Introduction

The main testable prediction of the Randall-Sundrum I extra dimension model is the resonant production of massive Kaluza-Klein gravitons (G_{KK}), which interact with all Standard Model particles. The branching ratios of the graviton in the different channels are presented in Tab. 5.1. The largest branching ratio is represented by the hadronic channel ($G_{KK} \to gg,\ q\bar{q}$), followed by the massive vector boson decays ($G_{KK} \to VV$, with $V = W, Z$), diphoton ($G_{KK} \to \gamma\gamma$) and dileptons ($G_{KK} \to \ell^+\ell^-$). However, the experimental signature of the decay to hadrons is the production of two back–to–back high p_T jets, which is overwhelmed by the QCD dijet production background.

This thesis is focused on the graviton decay $G_{KK} \to ZZ$, considering the semileptonic final states, that is,

$$G_{KK} \to ZZ \to \ell^+\ell^- q\bar{q}\ ,$$

with $\ell = e, \mu$. These channels were chosen due to the high efficiency in reconstructing the well-known process $Z \to \ell^+\ell^-$, and the high branching fraction of the hadronic decay of the Z boson.

The Randall-Sundrum model of extra dimensions represents an interesting motivation to look for resonances in the double vector boson channel. However, the study of the a pair of vector boson production is relevant by itself: several models predict new phenomena to be observed in this channel at the energy scales that are now being explored by the LHC.

This analysis is performed using the most general approach to look for any resonance in the VZ channel: the information of the spin 2 of the graviton is not explicitly used to optimize the signal over background efficiency. Furthermore, the experimental resolution of the hadronic V reconstruction does not allow us to distinguish between a W and a Z boson. This characteristic opens an interesting

Table 5.1: Branching ratios of the massive graviton G_{KK} decays, for m_G = 1 TeV.

Channel	Branching Ratio
$G_{KK} \rightarrow$ hadrons	68.5 %
$G_{KK} \rightarrow WW$	9.1 %
$G_{KK} \rightarrow ZZ$	4.5 %
$G_{KK} \rightarrow \gamma\gamma$	4.1 %
$G_{KK} \rightarrow \ell^+\ell^-$	2.0 %
$G_{KK} \rightarrow HH$	0.3 %

possibility: interpreted the present analysis in different scenarios, covering a broader range of new physics searches.

The hadronic V can be interpreted either as a W or a Z boson, leading to limits in the production cross section of WZ and ZZ exotic resonances. The ZZ bound can be interpreted in terms of the Randall–Sundrum model, and the WZ can be viewed in terms, for instance, of the Sequential Standard Model W'.

The Sequential Standard Model for new massive vector bosons is based on a 1989 proposal by G. Altarelli, B. Mele and M. Ruiz-Altaba [58]. They study the possibility of new heavy vector bosons being produced at $p\bar{p}$ colliders, and discuss the production and detection of the new particle in a general class of models, in particular signals decaying into $\ell\bar{\ell}jj$ channels.

The models are built considering some simple schemes for the vector boson couplings which are intended to cover the main possibilities, ranging from composite vector particles to new gauge bosons. The usual searches for new vector bosons $V^\pm$, V^0 are performed in the leptonic channels $V^\pm \rightarrow \ell^\pm\nu$ or $V^0 \rightarrow \ell^+\ell^-$. However, this new resonance could also be observed in channels such as $V^\pm \rightarrow \ell^\pm\nu jj$ or $V^0 \rightarrow \ell^+\ell^- jj$, typically arising from $V^\pm \rightarrow W^\pm Z$ or $V^0 \rightarrow W^+W^-$. The latter channels are, in many cases, the most favourable ones, for example in the following situations:

- When the $W^\pm Z$ or W^+W^- decay modes are large and consequently the already small branching ratios for the leptonic modes are further suppressed;
- When the leptonic modes are forbidden or very strongly suppressed. This is the case of a left-handed $W_R^\pm$ when the right-handed neutrino ν_R is too heavy for the decay $W_R \rightarrow e\nu_R$ to occur.

We present in the Appendix B further details on the cross section predicted by this benchmark model.

For heavy resonances the two-fermion system produced in the decay of each V is boosted, *i.e.* the fermions are emitted within a small opening angle in the laboratory frame. The hadronization of the $V \to q\bar{q}$ quarks would then produce a "single" jet with mass close the V mass, very different from a typical QCD jet. Monte Carlo (MC) simulations suggest that $\sim$ 70% of the decays would produce a merged-jet topology for resonances heavier than $\sim$ 800 GeV. This feature is exploited in a VZ final state, to discriminate a possible signal from the SM background (mainly coming from Z+jets events). For the same reason, some care is needed when reconstructing the $Z \to \ell^+\ell^-$ vector boson: the presence of each lepton interferes in the isolation of the other lepton, and has to be excluded from the isolation calculation in order to avoid introducing inefficiencies.

5.2 Datasets

The analysis is performed with the data sample of proton–proton collisions corresponding to an integrated luminosity of 5.0 fb^{-1} collected by the CMS detector at the LHC at $\sqrt{s} = 7$ TeV in 2011.

The considered events were recorded with single muon and double electron triggers, corresponding to the `SingleMu` and `DoubleElectron` datasets. Typical efficiencies exceed 95% (83%) for the muon (electron) triggers.

Events are triggered based on the logical `OR` of the lowest-threshold, unprescaled High Level Trigger (HLT) paths. The electron paths have additional requirements of isolation and electron identification. In order to follow the increase in instantaneous luminosity, the trigger thresholds have been progressively increased during the data taking throughout the year. A summary of the triggers used for each run period is given in Tab. 5.2 (Tab. 5.3) for the muon (electron) triggers.

Simulated Monte Carlo samples were generated to study the signal and background kinematic distributions. Several possible Standard Model (SM) background processes that could contribute with two leptons and a (massive) jet in the final state were considered:

- Z/γ^* + jets: the dominant background for this analysis, with a leptonic Z and a jet that can pass the analysis selections;

Table 5.2: HLT muon paths. The run range refers to the data-taking period with the trigger unprescaled. The luminosity is the recorded luminosity in that period.

HLT path	Run range	Luminosity
HLT_Mu24_v*	160431–163869	216 pb^{-1}
HLT_Mu30_v*	165088–167913	930 pb^{-1}
HLT_Mu40_v*	170249–175921	1.10 fb^{-1}
HLT_Mu40_eta2p1_v*	175973–180252	2.44 fb^{-1}

Table 5.3: HLT electron paths. The run range refers to the data-taking period with the trigger unprescaled. The luminosity is the recorded luminosity in that period.

HLT path	Run range	Luminosity
HLT_Ele17_CaloIdL_CaloIsoVL_ Ele8_CaloIdL_CaloIsoVL_v*	160404–173198	1.81 fb^{-1}
HLT_Ele17_CaloIdT_CaloIsoVL_ TrkIdVL_TrkIsoVL_Ele8_CaloIdT_ CaloIsoVL_Tr kIdVL_TrkIsoVL_v*	167039–180252	4.24 fb^{-1}

- $t\bar{t}$ + jets: the second leading background, can generate two prompt leptons from the leptonic decay of the W pair, and have high multiplicity of jets which can pass the analysis selections;
- $WW, WZ, ZZ, \gamma V$ + jets: non-resonant diboson SM background, with prompt leptons and jets from hadronic V decays or initial state radiation;
- W + jets: the process can generate one prompt lepton from the W decay, a fake lepton from hadronic activity and a jet passing the analysis selection.

The summary of the signal samples for the RS and W' scenarios are given in Table 5.4 and Table 5.5 respectively. The listed cross sections are `PYTHIA` LO, per channel (electrons or muons). The k factors include NLO (NNLO) corrections for the RS (W') samples. The G_{KK} samples are generated with $\overline{M}_{Pl} = 0.05$. The Monte Carlo samples are presented in Table 5.6).

The `PYTHIA` 6.424 [59] leading-order (LO) generator with tune Z2 [60] is used to generate the signal events and simulate the parton showering. The passage

Table 5.4: Signal Monte Carlo samples in the RS scenario.

Mass (GeV/c^2)	Cross Section (pb)	K factor
$\mathrm{G_{KK}} \to q\bar{q}\,\ell^+\ell^-$ (e^+e^- or $\mu^+\mu^-$)		
750	8.35×10^{-3}	1.75
1000	1.52×10^{-3}	1.78
1250	3.47×10^{-4}	1.79
1500	8.83×10^{-5}	1.78
1750	3.43×10^{-5}	1.76
2000	7.05×10^{-6}	1.76

Table 5.5: Signal Monte Carlo samples in the W' scenario.

Mass (GeV/c^2)	Cross Section (pb)	K factor
$W' \to q\bar{q}\,\ell^+\ell^-$ (e^+e^- or $\mu^+\mu^-$)		
700	1.267×10^{-2}	1.35
800	6.815×10^{-3}	1.35
900	3.842×10^{-3}	1.34
1000	2.286×10^{-3}	1.33
1100	1.413×10^{-3}	1.32
1200	8.955×10^{-4}	1.31
1300	5.750×10^{-4}	1.30
1400	3.784×10^{-4}	1.28
1500	2.554×10^{-4}	1.26

Table 5.6: Background Monte Carlo samples. The notation ℓ stands for electrons, muons or taus.

Samples	Cross Section (pb)	Simulation Details
W+jets	212.5	LO ($p_T^W > 100$ GeV/c)
$t\bar{t}$	157.5	NLO
γV+jets	56.5	LO
$Z/\gamma^*(\ell^+\ell^-)$+jets	25.1	LO ($p_T^Z > 100$ GeV/c)
$W(\ell\nu)\,W(\ell\nu)$+jets	3.8	LO
$W(q\bar{q})\,Z(\ell^+\ell^-)$+jets	1.14	LO
$Z(q\bar{q})\,Z(\ell^+\ell^-)$+jets	0.57	LO

of the particles through the detector is fully simulated with the `GEANT4` 9.4 — package [61].

To better account for the loop effects, calculations of higher orders in perturbation theories were carried on in the literature to get a more accurate value of the cross section. The ratio $\sigma_{(N)NLO}/\sigma_{LO}$ — known as k factor — is then used as a scale factor in the simulated samples produced with a LO generator. Mass-dependent k factors are applied. For the $\mathrm{G_{KK}}$ signal, next-to-leading order (NLO) corrections are calculated using the two cutoff phase space slicing method [62, 63] and the diphoton final state. For the W' signal, the next-to-next-to-leading order (NNLO) corrections are calculated with `FEWZ` [64] and the leptonic final state.

The background samples are generated using the `MADGRAPH` 5.1.1.0 matrix-element generator [65, 66], while `PYTHIA` is used for the parton showering and hadronization, with the same version and tuning as for signal samples. The PDF used is CTEQ6L1 [67]. Jets are matched to partons using the MLM scheme [68].

The LHC data in 2011 had several simultaneous pp interactions per bunch crossing, phenomenon known as pile-up. These extra interactions have to be included in the Monte Carlo simulation to evaluate its effect and to better reproduce the data conditions seen in the detector. The datasets were simulated using as pile-up scenario a flat distribution from 0–10 interactions per crossing with a tail above 10 to higher values corresponding to a Poisson distribution, with a mean of 10 interactions. The simulated data is then reweighted according to the distribution of the number of vertices in the collision data.

5.3 Reconstruction and Event Selection

5.3.1 Muon Reconstruction

The analysis is based on the *cocktail* muon reconstruction [69], an algorithm optimized for the high-p_T muon kinematic region. The muon candidates are selected according to the standard “tight” selection criteria inside CMS collaboration, with the exception of the isolation requirement due to the boosted topology considerations.

In summary, the muon selection consists of the following requirements:

- The muon must be reconstructed in two algorithms: using only the tracker information (“tracker” muon), and using both tracker and muon chamber information (“global” muon);
- The muon’s transverse impact parameter with respect to the beam-spot as measured by the tracker-only fit must be less than 2 mm;
- The global muon track must have at least one associated pixel and one associated muon hits;
- The tracker-muon must be matched to segments in at least two muon stations;
- The muon must have at least 9 tracker layers used in the fit.
- The offline muon transverse momentum (p_T^{μ}) must be greater than 45 GeV/c and its pseudorapidity ($|\eta|$) smaller than 2.4;

5.3.2 Electron Reconstruction

The electrons are reconstructed using the Gaussian-sum filter (GSF) algorithm [70]. Electron candidates are then selected using simple cuts on a few discriminating variables. These variables can be categorized in three groups: electron identification (ID), conversion rejection or isolation. In the simplest selection, the cuts have been optimized jointly so to define various working points corresponding to different efficiency and background rejection.

The selection used in this analysis is the “95% efficiency Working Point”, or WP95 (see Table 5.7); it is a loose selection, as the Z mass constraint manages to keep the electron background at a manageable level. Electrons are required to have $p_T^e > 45$ GeV/c and $|\eta| < 2.5$. The isolation variables have been corrected for pile-up by using the FASTJET energy density technique [71, 72].

Table 5.7: The definition of cuts used in the simple cuts electron selection for electron candidates in the barrel (EB) and in the endcaps (EE).

Electron Selection (WP95)		
Electron ID	EB	EE
$\sigma_{i\eta i\eta}$	0.012	0.031
$\|\Delta\eta_{in}\|$	0.07	0.011
$\|\Delta\phi_{in}\|$	0.8	0.7
Conversion rejection	EB	EE
Expected missing inner hits	0	0
Isolation	EB	EE
Combined relative isolation	0.15	0.1

5.3.3 Jet Reconstruction

The particle-flow (PF) algorithm [73] reconstructs a complete list of particle candidates in each event from the measurements in all the components of the CMS detector in an integrated fashion. The algorithm separately identifies muons, electrons, photons, charged and neutral hadrons. Jets are clustered from the reconstructed PF particles using the infrared-safe anti-k_T [74] algorithm with a distance parameter of 0.7, as implemented in `FASTJET` [75, 76]. The jet momentum is determined as the vector sum of all particle momenta in this jet, and is found in the simulation to be within 5% to 10% of the true momentum of the generator-level jet over the whole p_T spectrum and detector acceptance. An area-based correction is applied to take into account the extra energy clustered in jets due to additional proton-proton interactions within the same bunch crossing, and for the average effect of out-of-time pile-up interactions [71, 72].

Jets are filtered according to the following requirements:

- The jet neutral hadron energy fraction must be less than 0.99;

- The jet neutral electromagnetic energy fraction must be less than 0.99;
- The number of constituents must be greater than 1;
- The jet charged hadron energy fraction must be greater than 0.0;
- The jet charged electromagnetic energy fraction must be less than 0.99;
- The charged multiplicity must be greater than 0;
- $p_T^{jet} > 30$ GeV/c;
- $|\eta| < 2.4$.

5.3.4 Event Preselection

The event preselection is the collection of the most loose requirements applied in the datasets to start the analysis. Candidate events need to have at least two good quality reconstructed leptons and one good jet, according to the selection requisites presented in the previous sections. An additional requirement in the muon channel is that at least one muon have to be within $|\eta| < 2.1$, due to online trigger requirements in this variable.

5.3.5 $Z \rightarrow \ell\ell$ Reconstruction

Whenever two same-flavor, opposite-sign leptons are found in the event, a Z candidate is formed summing the four-momenta of the leptons. The selected Z candidate is required to have invariant mass in the $70 < M_Z < 110$ GeV/c^2 mass range and with a transverse momentum $p_T^Z > 150$ GeV/c.

The selection on the Z boson p_T is motivated by the boosted topology of the signal — this selection provides a good background suppression. The cut value was motivated by the a combination of two factors: optimization of a figure of merit given by $N_s/\sqrt{N_s + N_b}$ (where N_S and N_B are the number of expected signal and background events) and the generator level cut ($p_T^Z > 100$ GeV/c) on DY+jets simulated samples. In the case of multiple matching pairs, the Z candidate with the mass closest to the nominal Z mass is selected.

Figure 5.1 shows the distribution of M_Z (top) and p_T^Z (bottom) for data after the full event selection, compared to distributions for the major background processes from Monte Carlo simulation. The distributions for two benchmark signal samples (RS graviton with mass $M_{KK} = 750$ GeV/c^2 and $k/\overline{M}_{Pl} = 0.05$, and a W' with mass $M_{W'} = 1000$ GeV/c^2) are also plotted for comparison. Figure 5.2 shows the p_T^Z distributions of $Z \rightarrow \ell\ell$ candidates after the VZ candidate selection (top) and after all selection criteria have been applied (bottom).

5.3.6 $V \rightarrow$ jet Reconstruction

The $V \rightarrow q\bar{q}$ candidate is reconstructed as a *single* jet satisfying the following requirements:

- $\Delta R^1(\text{jet}, \ell) > 1.0$, where ℓ is any of the two leptons forming the Z candidate;
- $65 < M_j < 120$ GeV/c^2, where M_j is the jet mass, computed from the vector sum of the four-momenta of the constituent particle-flow particles;
- $p_T^V > 250$ GeV/c, where p_T^V is the V candidate transverse momentum. The value has been determined by maximizing a $N_S/\sqrt{N_S + N_B}$ significance for the lowest W' mass point (700 GeV/c^2) considered in this search.

Studies on simulated signal samples show that this approach results in an efficiency of $\sim 75\%$ for resonances heavier than 1000 GeV/c^2 (see bottom plot of Fig. 5.3). In these cases, the reconstructed jet mass exhibits a broader distribution than the generator-level jet, due to detector resolution. Other effect seen is the shift of the jet mass peak to higher masses (~ 100 GeV/c^2) with respect to the generator-level jets (~ 90 GeV/c^2, see center plot of Fig. 5.3 for $m_G = 2000$ GeV/c^2). This shift is due to the over-correction of the jet energy scale for $p_T^{jet} > 500$ GeV/c, also responsible for the 3% drop in the monojet efficiency for signal masses of 1500 GeV/c^2 and above, seen in Fig. 5.3 (bottom).

The top plot of Fig. 5.3 shows the jet mass distributions for $m_G = 750$ GeV/c^2. In this case a second peak appears at $M_j \sim 30$ GeV/c^2, corresponding to the kinematic regime in which the two jets cease to overlap, and the $R = 0.7$ single-jet reconstruction approach becomes inefficient. For the regions with resonance mass smaller than ~ 700 GeV/c^2, the standard dijet topology reconstruction techniques should be followed. For the purposes of this analysis the studies were limited to the monojet reconstruction approach which has been optimized for the high-mass signal region.

Other possibilities for the efficient reconstruction of the high-mass hadronic resonances have been investigated in Ref. [77]. Two alternatives have been taken

---

[1] ΔR is defined as $\Delta R = \sqrt{\Delta\phi^2 + \Delta\eta^2}$

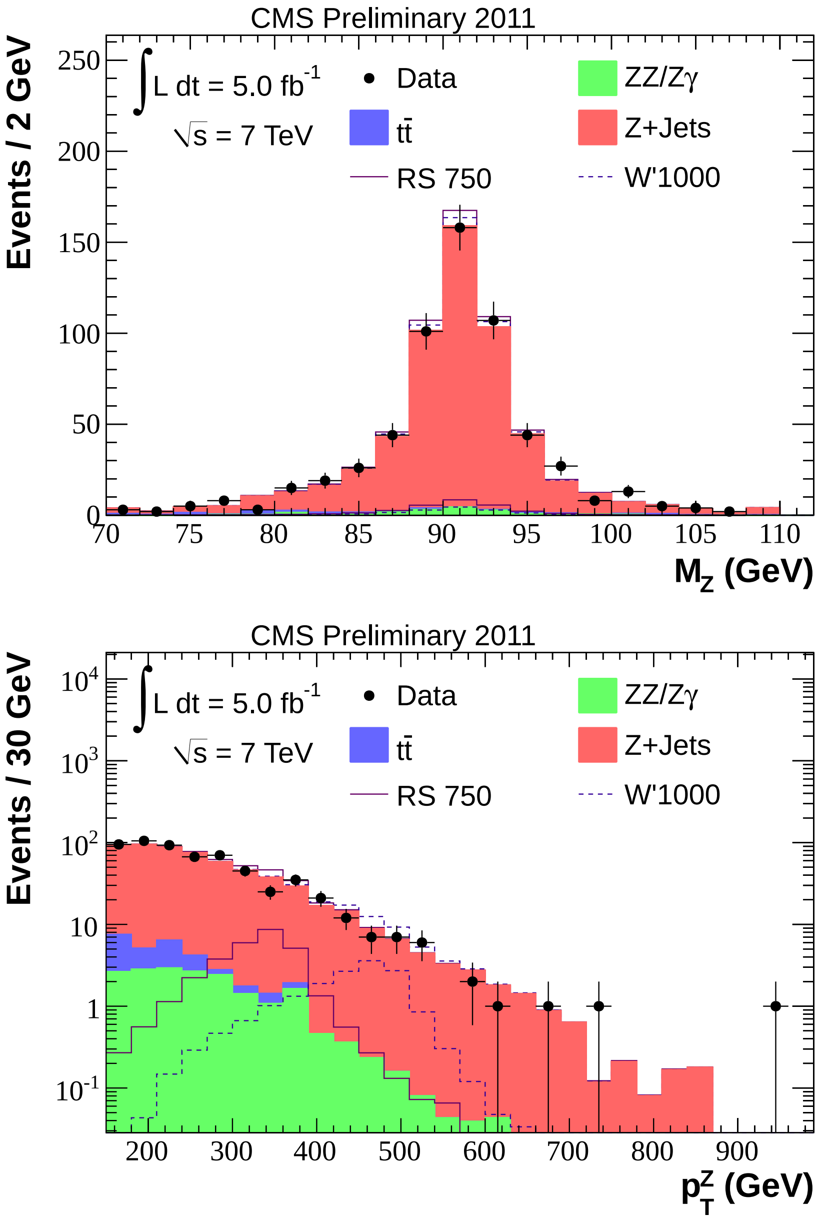

Figure 5.1: Distribution of M_Z (top) and p_T^Z (bottom) for data after the full Z leptonic selection, compared to distributions for the major background processes from Monte Carlo simulation for the electron and muon channels combined. The distributions for simulated RS and W' samples are also overlaid for illustration purposes.

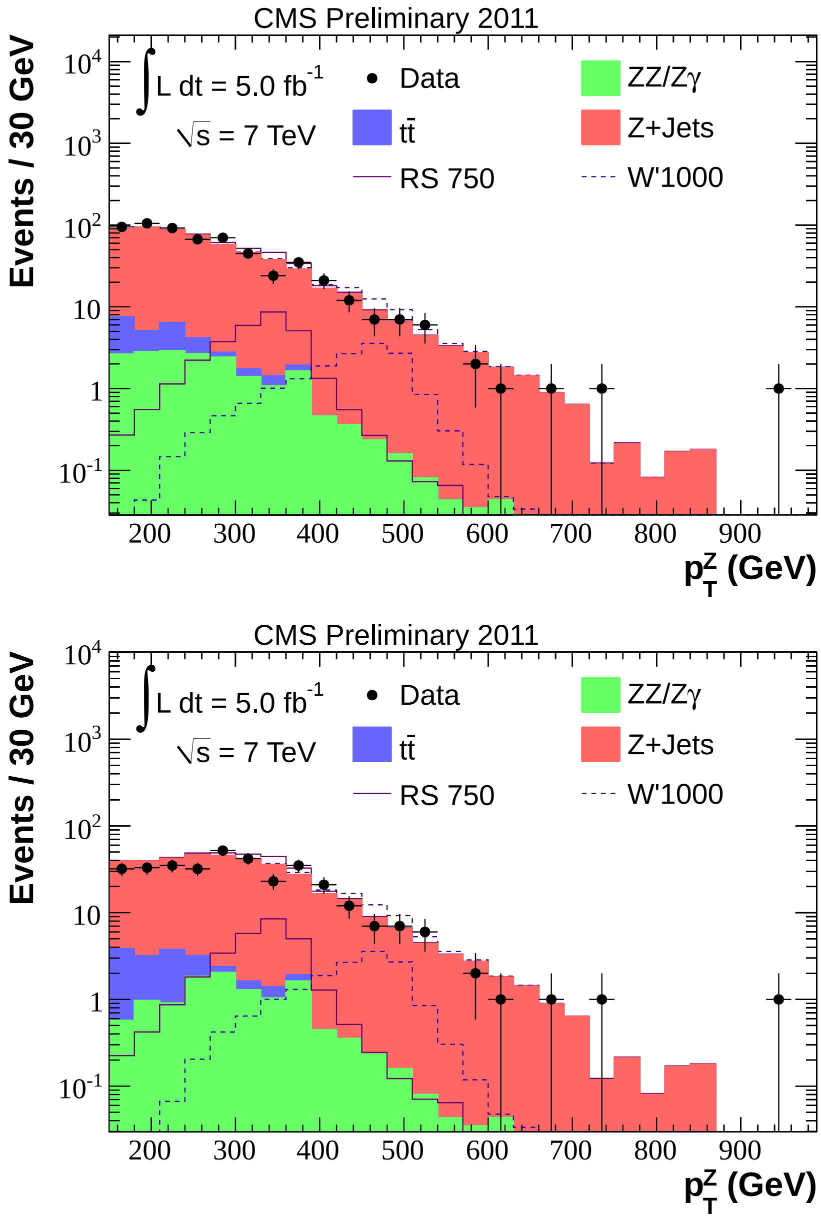

Figure 5.2: p_T^Z distributions of $Z \rightarrow \ell\ell$ candidates for MC background, signal and data after the VZ candidate selection (top) and after all selection criteria have been applied (bottom).

into account: the *FatJets* approach in the dijet resonance search [78]; and the Cambridge-Aachen jet algorithm used in the studies of jet substructure. In both cases, the different algorithm choices did not achieve a better reconstruction efficiency for the merged-jets topology.

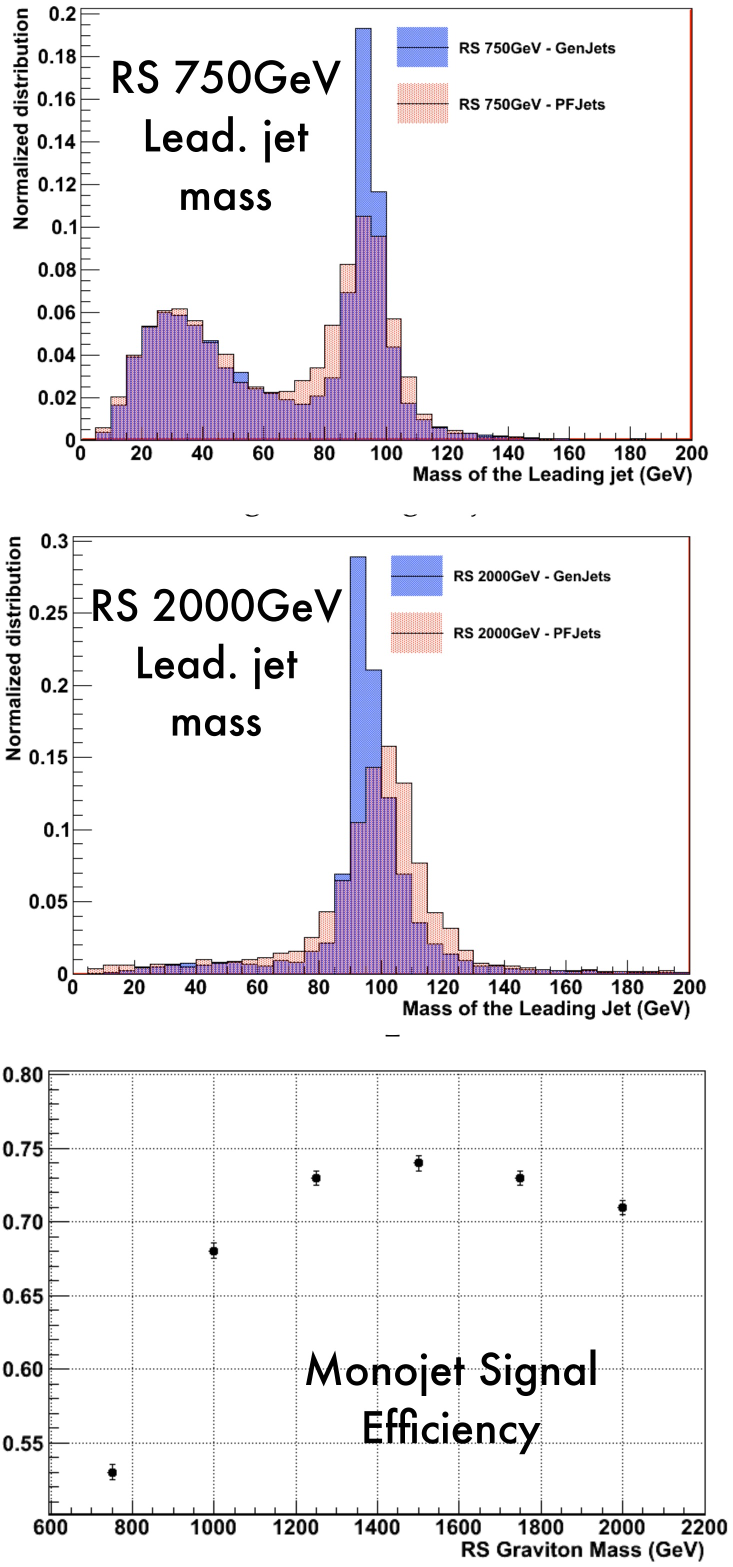

Figure 5.3: Comparison of M_j distributions produced with generator-level ("GenJets", in blue color) and reconstructed ("PF Jets", in red color) kinematic information for a resonance of mass 750 GeV/c^2 (top) and 2000 GeV/c^2 (middle). In the bottom plot, the "massive" monojet reconstruction efficiency is shown as a function of the signal resonance mass.

Figure 5.4 shows the comparison of the M_j (left) and p_T^V (right) distributions between data and the major background processes from Monte Carlo simulation after the full event selection. The distributions of two benchmark signals are also shown. The distributions of the M_j and p_T^V before the invariant mass cut on the monojet are shown in Fig. 5.5.

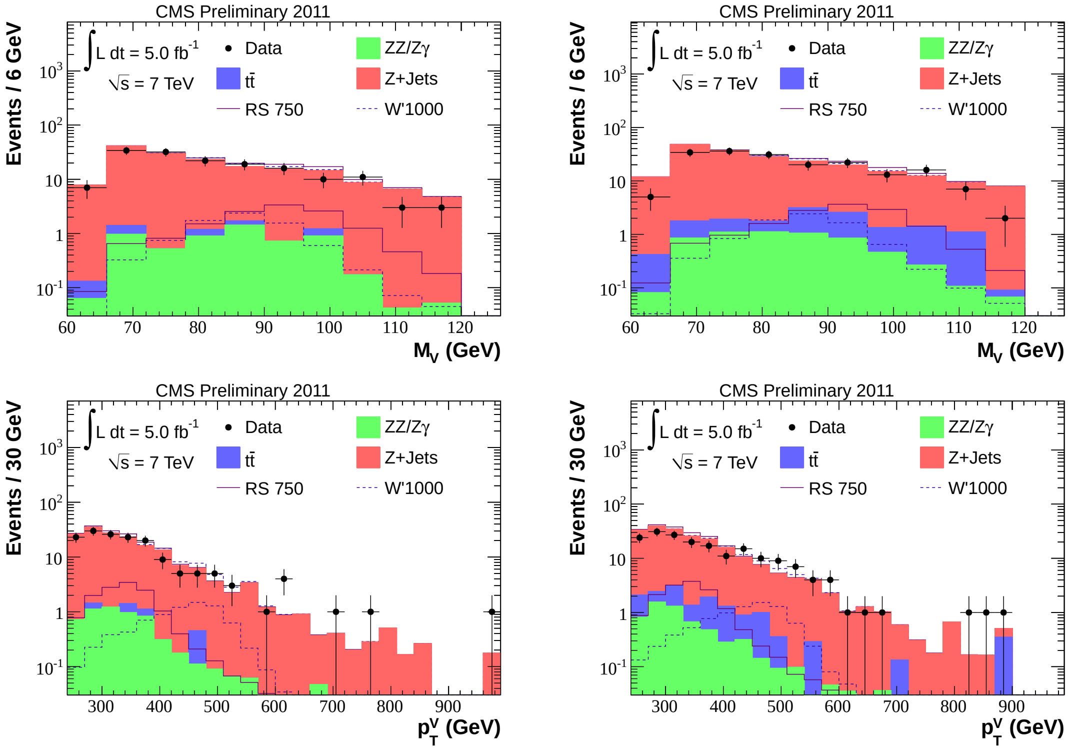

Figure 5.4: Comparison of the M_j (top) and p_T^V (bottom) distributions for electron (left) and muon (right) channels between data and the MC distributions for the major background processes after the full event selection.

5.3.7 The Resonance Mass

Once the $Z \to \ell^+\ell^-$ and (mono-jet) $V \to q\bar{q}$ candidates have been reconstructed, their four momenta are combined to compute the mass of the mother particle, M_{VZ}. This variable is used to evaluate the hypothesis of the signal presence in the analyzed datasets.

Figure 5.6 shows the comparison of the M_{VZ} distributions between data and the main background processes from Monte Carlo simulation after the full event selection in the electron (top) and muon (bottom) channels. Figure 5.7 shows the

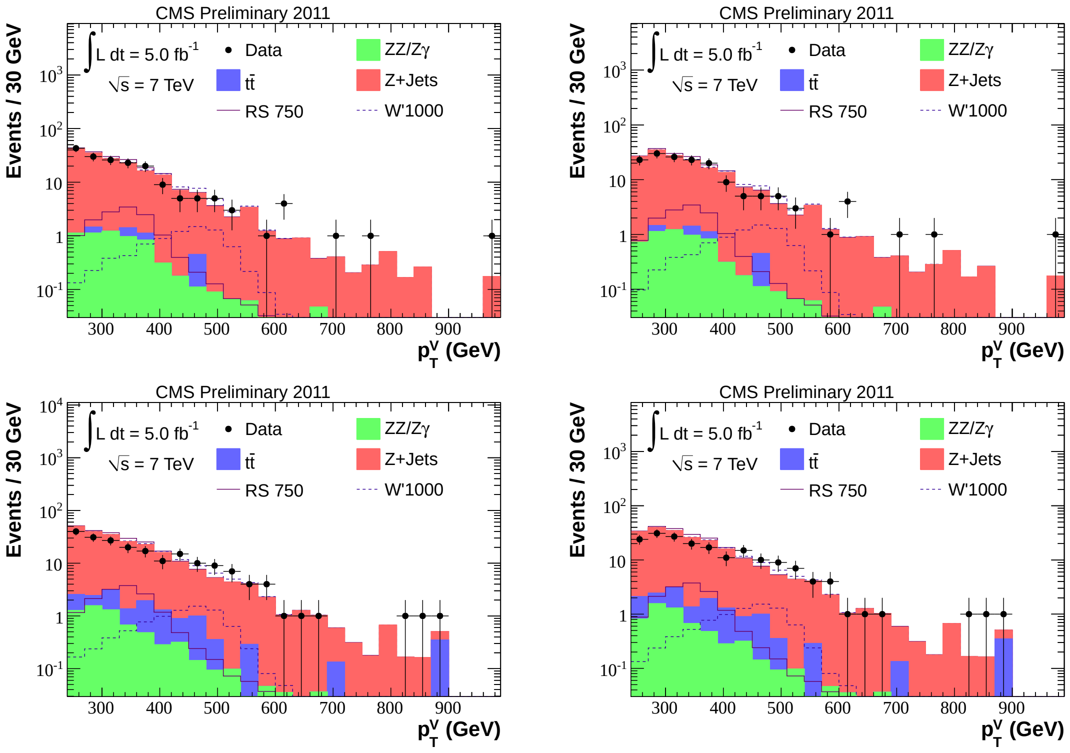

Figure 5.5: p_T^V distributions of $V \rightarrow jet$ candidates for MC background, signal and data after the VZ candidate selection (left) and after all selection criteria have been applied (right) for the electron (top) and muon (bottom) channels.

cumulative[2] plots. The distributions of two benchmark signals are also shown.

5.3.8 Expected and Observed Yields

Table 5.8 lists the expected signal and background yields, based on Monte-Carlo estimated acceptance and NLO cross-section calculations. It is broken down into the electron and muon channels in Tables 5.9 and 5.10, respectively. Since the Z+jets sample we use has a generator level cut of $p_T^Z = 100$ GeV/c, the agreement between data and Monte Carlo is only seen after a reconstruction level cut of $p_T^Z = 150$ GeV/c has been applied. The total expected background yield is 354 ± 7 events for a luminosity of 5.0 fb^{-1} , to be compared to 332 observed events. This comparison is *not* used to test the presence of a signal. Instead, the background estimate is derived using a data-driven approach, and a search for excess of the

---

[2] A cumulative distribution of a histogram of N bins is obtained by, for each n ranging from 1 to $N-1$, adding to the $(N-n)^{\text{th}}$ bin its content plus the content of the $(N-n+1)^{\text{th}}$ bin. It is useful to graphically estimate the compatibility in the low statistics tail of two distributions, in this case, the data against the simulated background samples.

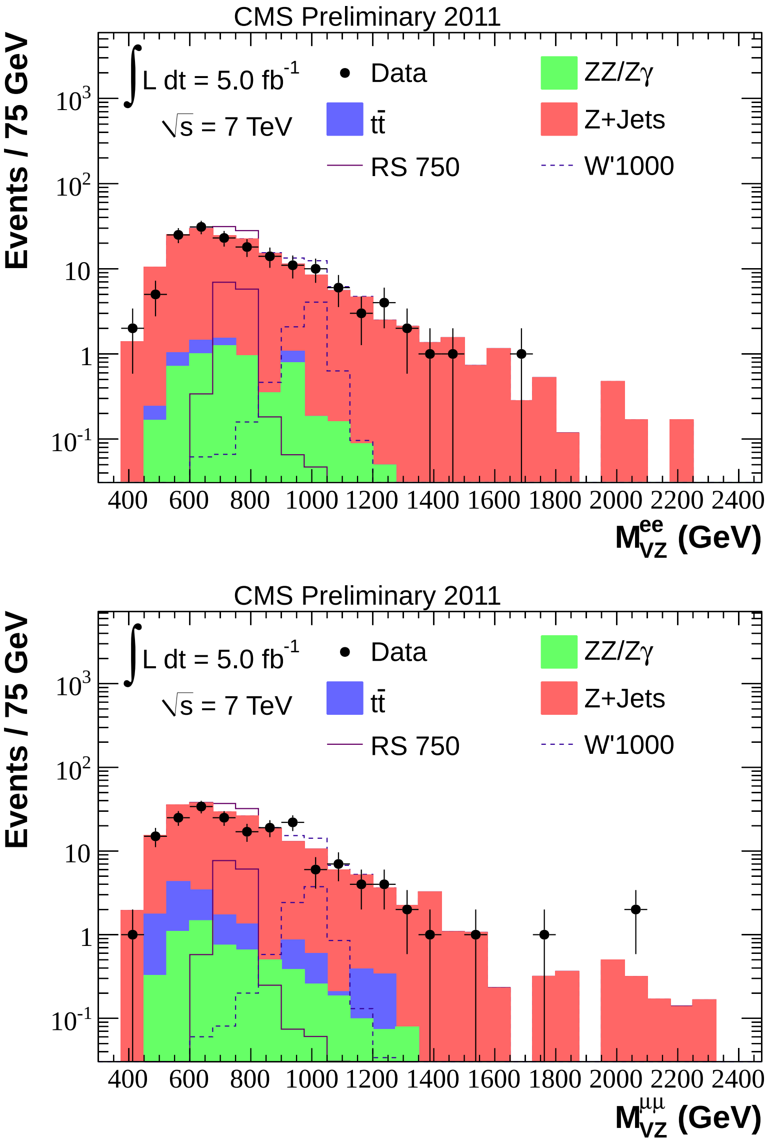

Figure 5.6: Distribution of M_{VZ} for the electron (top) and muon (bottom) channels. The comparison to the total MC background distribution is also shown.

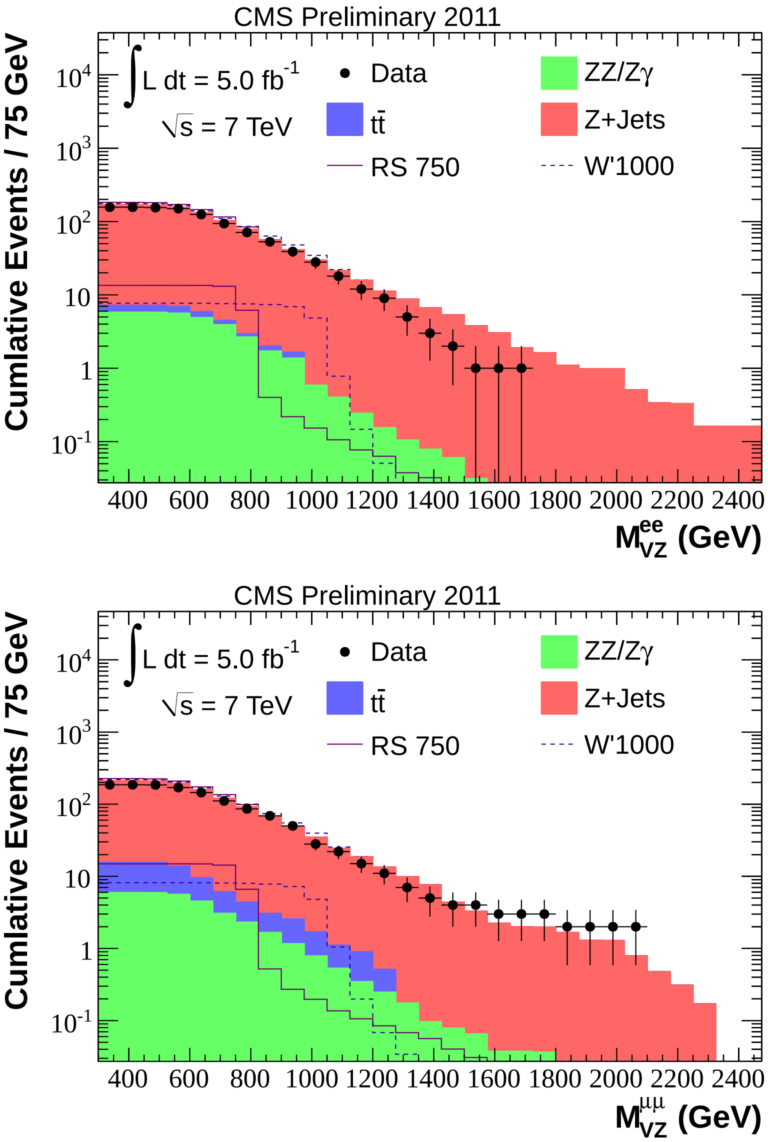

Figure 5.7: Cumulative distribution of M_{VZ} for the electron (top) and muon (bottom) channels. The comparison to the total MC background distribution is also shown.

expected background is carried out as a function of the VZ candidate mass.

Table 5.8: Observed events denoted as "Data", and expected signal and background yields after the main steps of the event selection for the electron and muon channels combined. The numbers correspond to an integrated luminosity of 5.0 fb^{-1} .

Sample	Z Selection	V Selection	p_T^V
$Z + jets$	11071 ± 39	514 ± 8	333 ± 7
$t\bar{t}$	88 ± 5	13 ± 2	10 ± 2
ZZ	39.8 ± 0.4	4.1 ± 0.1	2.9 ± 0.1
$V\gamma$	83 ± 6	5 ± 1	2 ± 1
$W + jets$	3.8 ± 0.9	0.4 ± 0.3	0.4 ± 0.3
WW	6.2 ± 0.4	0.36 ± 0.08	0.25 ± 0.07
WZ	65.6 ± 0.7	8.8 ± 0.3	5.5 ± 0.2
Total Background	11358 ± 40	545 ± 9	354 ± 7
Data	12503	578	332
G_{RS} (750 GeV)	50.2 ± 0.2	28.1 ± 0.2	26.4 ± 0.2
G_{RS} (1000 GeV)	9.73 ± 0.04	6.99 ± 0.04	6.83 ± 0.03
G_{RS} (1250 GeV)	2.177 ± 0.010	1.706 ± 0.009	1.678 ± 0.009
G_{RS} (1500 GeV)	0.461 ± 0.002	0.376 ± 0.002	0.368 ± 0.002
G_{RS} (1750 GeV)	0.1082 ± 0.0006	0.0894 ± 0.0005	0.0874 ± 0.0005
G_{RS} (2000 GeV)	0.0276 ± 0.0001	0.0229 ± 0.0001	0.0222 ± 0.0001
W' (700 GeV)	85.6 ± 0.8	63.4 ± 0.7	57.2 ± 0.6
W' (800 GeV)	47.8 ± 0.4	38.9 ± 0.4	36.8 ± 0.4
W' (900 GeV)	29.0 ± 0.3	24.9 ± 0.2	24.1 ± 0.2
W' (1000 GeV)	17.1 ± 0.2	15.1 ± 0.1	14.8 ± 0.1
W' (1100 GeV)	10.30 ± 0.10	9.26 ± 0.09	9.09 ± 0.09
W' (1200 GeV)	6.26 ± 0.06	5.66 ± 0.05	5.56 ± 0.05
W' (1300 GeV)	3.53 ± 0.03	3.22 ± 0.03	3.16 ± 0.03
W' (1400 GeV)	2.15 ± 0.02	1.94 ± 0.02	1.90 ± 0.02
W' (1500 GeV)	1.27 ± 0.01	1.14 ± 0.01	1.11 ± 0.01

Table 5.9: Observed events denoted as "Data", and expected signal and background yields after the main steps of the event selection for the electron channel. The numbers correspond to an integrated luminosity of 5.0 fb^{-1} .

Sample	Z Selection	V Selection	p_T^V
$Z + jets$	5195 ± 27	235 ± 6	151 ± 5
$t\bar{t}$	21 ± 2	1.4 ± 0.6	1.3 ± 0.6
ZZ	18.8 ± 0.3	1.98 ± 0.08	1.39 ± 0.07
$V\gamma$	39 ± 4	1.6 ± 0.8	1.4 ± 0.8
$W + jets$	1.0 ± 0.5	0 ± 0	0 ± 0
WW	2.9 ± 0.2	0.18 ± 0.06	0.14 ± 0.05
WZ	30.4 ± 0.5	4.1 ± 0.2	2.5 ± 0.1
Total Background	5308 ± 27	244 ± 6	157 ± 5
Data	6044	277	157
G_{RS} (750 GeV)	24.0 ± 0.2	13.4 ± 0.1	12.5 ± 0.1
G_{RS} (1000 GeV)	4.60 ± 0.03	3.27 ± 0.02	3.19 ± 0.02
G_{RS} (1250 GeV)	0.977 ± 0.006	0.759 ± 0.005	0.747 ± 0.005
G_{RS} (1500 GeV)	0.176 ± 0.001	0.141 ± 0.001	0.137 ± 0.001
G_{RS} (1750 GeV)	0.0374 ± 0.0003	0.0301 ± 0.0003	0.0290 ± 0.0003
G_{RS} (2000 GeV)	0.00819 ± 0.00008	0.00662 ± 0.00008	0.00629 ± 0.00007
W' (700 GeV)	41.8 ± 0.5	30.6 ± 0.5	27.8 ± 0.4
W' (800 GeV)	22.7 ± 0.3	18.4 ± 0.3	17.5 ± 0.3
W' (900 GeV)	13.9 ± 0.2	11.9 ± 0.2	11.6 ± 0.2
W' (1000 GeV)	8.2 ± 0.1	7.30 ± 0.10	7.16 ± 0.10
W' (1100 GeV)	4.93 ± 0.07	4.41 ± 0.06	4.33 ± 0.06
W' (1200 GeV)	2.92 ± 0.04	2.64 ± 0.04	2.59 ± 0.04
W' (1300 GeV)	1.52 ± 0.02	1.38 ± 0.02	1.35 ± 0.02
W' (1400 GeV)	0.84 ± 0.01	0.74 ± 0.01	0.72 ± 0.01
W' (1500 GeV)	0.456 ± 0.008	0.400 ± 0.008	0.382 ± 0.008

Table 5.10: Observed events denoted as "Data", and expected signal and background yields after the main steps of the event selection for the muon channel. The numbers correspond to an integrated luminosity of 5.0 fb^{-1} .

Sample	Z Selection	V Selection	p_T^V
$Z + jets$	5876 ± 29	279 ± 6	182 ± 5
$t\bar{t}$	67 ± 4	11 ± 2	9 ± 2
ZZ	21.1 ± 0.3	2.08 ± 0.09	1.53 ± 0.07
$V\gamma$	45 ± 4	3 ± 1	0.9 ± 0.6
$W + jets$	2.8 ± 0.8	0.4 ± 0.3	0.4 ± 0.3
WW	3.3 ± 0.3	0.18 ± 0.06	0.11 ± 0.04
WZ	35.2 ± 0.5	4.7 ± 0.2	3.0 ± 0.2
Total Background	6050 ± 29	300 ± 7	197 ± 5
Data	6459	301	175
G_{RS} (750 GeV)	26.2 ± 0.2	14.8 ± 0.1	13.9 ± 0.1
G_{RS} (1000 GeV)	5.13 ± 0.03	3.73 ± 0.03	3.64 ± 0.03
G_{RS} (1250 GeV)	1.200 ± 0.008	0.947 ± 0.007	0.930 ± 0.007
G_{RS} (1500 GeV)	0.285 ± 0.002	0.235 ± 0.002	0.231 ± 0.001
G_{RS} (1750 GeV)	0.0708 ± 0.0004	0.0593 ± 0.0004	0.0584 ± 0.0004
G_{RS} (2000 GeV)	0.0194 ± 0.0001	0.0162 ± 0.0001	0.0160 ± 0.0001
W' (700 GeV)	43.8 ± 0.6	32.7 ± 0.5	29.4 ± 0.5
W' (800 GeV)	25.1 ± 0.3	20.5 ± 0.3	19.4 ± 0.3
W' (900 GeV)	15.1 ± 0.2	13.0 ± 0.2	12.5 ± 0.2
W' (1000 GeV)	8.8 ± 0.1	7.8 ± 0.1	7.6 ± 0.1
W' (1100 GeV)	5.37 ± 0.07	4.85 ± 0.07	4.76 ± 0.06
W' (1200 GeV)	3.34 ± 0.04	3.03 ± 0.04	2.97 ± 0.04
W' (1300 GeV)	2.01 ± 0.03	1.84 ± 0.02	1.81 ± 0.02
W' (1400 GeV)	1.31 ± 0.02	1.20 ± 0.02	1.18 ± 0.02
W' (1500 GeV)	0.81 ± 0.01	0.74 ± 0.01	0.72 ± 0.01

5.4 Background Estimation

According to simulation, the dominant ($\sim$ 90%) background in this analysis, after all selection cuts, is the inclusive Z production ("Z+jets"), with additional contributions from $t\bar{t}$+jets and the continuum SM two-vector boson production (WZ and ZZ). The shape and the overall normalization of the expected background M_{VZ} distributions are derived from data, with additional cross-checks carried out with the inclusive simulated background samples. Effects caused by pile-up were modeled by adding to the generated events multiple interactions with a multiplicity distribution matched to the luminosity profile of the collision data.

5.4.1 Background Modeling

The background is modeled by using a "M_j sideband" which provides a sample kinematically equivalent to the nominal selection. In the case of the (dominant) Z+jets background, the sideband is populated by the combinatorial background that leaks in the nominal M_j window. The only qualitative difference between the sideband and the nominal M_j window is observed for the (subdominant) ZZ background. In this case, events fall in the sideband only when the two quarks from the Z partially overlap. In this case the mass associated to the reconstructed jet is smaller than the Z mass. This difference is not problematic for the analysis, since Z+jets represents more than 90% of the background in both the M_j sideband and the nominal M_j window.

The M_j sideband has been used by the $H \to ZZ \to \ell^+\ell^- q\bar{q}$ analysis performed by CMS on the 2011 dataset [79]. To explain the procedure, it will be used the distributions made for the electron and the muon channels combined. The procedure includes the following steps:

- A sideband of the M_j distribution is defined ($30 < M_j < 65$ GeV/c^2), on which the remaining selection cuts are applied unmodified. Figure 5.8 shows the distributions for the M_j in the full (sideband and nominal-selection) mass window.

- The M_{VZ} distribution for the sideband dataset is considered. This is shown in the top plot of Fig. 5.9, compared to the simulated distribution for the same selection.

- The ratio $\alpha(M_{VZ})$ is defined as the total number of simulated background

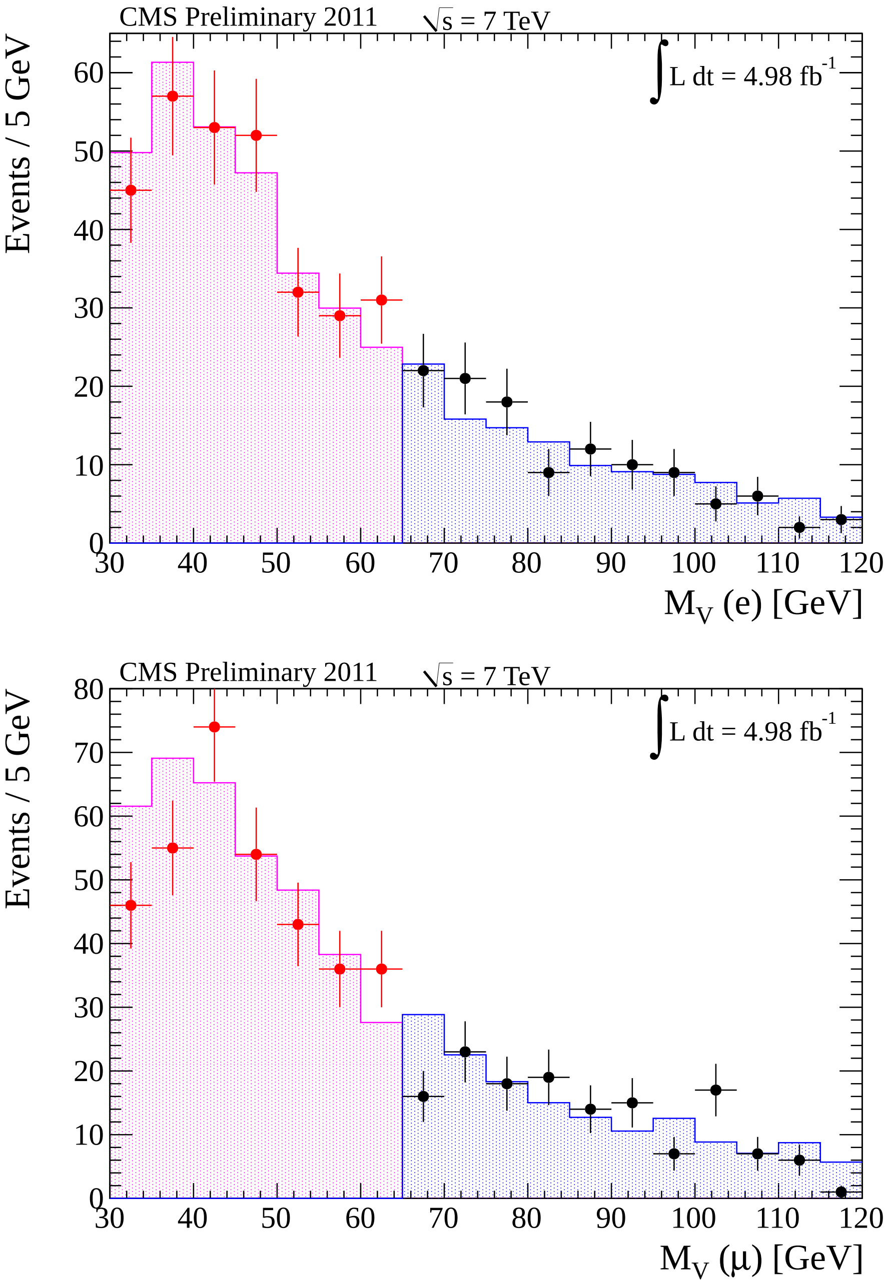

Figure 5.8: Distribution of M_j in the sideband and nominal window for data and Monte Carlo for the electron (top) and muon (bottom) channels. The Monte Carlo background samples have been normalized to the integrated luminosity and reweighted to match the pileup distributions observed in the data.

entries in the M_{VZ} spectrum with the nominal ("NS": $65 < M_j < 120$ GeV/c^2) and sideband ("SB": $30 < M_j < 65$ GeV/c^2) selections:

$$\alpha(M_{VZ}) = \frac{N_{NS}(M_{VZ})}{N_{SB}(M_{VZ})} \tag{5.1}$$

where $N_{NS}(M_{VZ})$ [$N_{SB}(M_{VZ})$] is the number of events in the signal region (sideband) contained in a bin of the VZ mass distribution centered at a given value M_{VZ}. The $\alpha(M_{VZ})$ distribution for the electron and muon channels combined can be seen in the center plot of Fig. 5.9.

- The product of the M_{VZ} distribution made with the data sideband selection and the $\alpha(M_{VZ})$ ratio is used to derive an estimate of the background M_{VZ} distribution with the nominal selection. The estimated background M_{VZ} distribution for the electron and muon channels combined is shown on the bottom plot of Fig. 5.9 (red dots), along with the total Monte Carlo background (blue histogram) and the data distributions (black dots). The product of the $\alpha(M_{VZ})$ and the sideband M_{VZ} distribution is done bin–by–bin instead of fitting $\alpha(M_{VZ})$ to avoid fitting on top of an already fitted variable in the final background estimation.

- An analytical function is used to fit the derived M_{VZ} distribution, which is then used as the basis for the modeling of the expected SM background distribution.

There are several advantages in using the differential ratio $\alpha(M_{VZ})$ for the background modeling of the M_{VZ} distributions:

- The larger statistics available in the M_j data sideband can be exploited;

- The background estimation gets insensitive to several systematic effects (*e.g.* the luminosity of the collected sample, pile-up corrections, etc) which cancel out in the $\alpha(M_{VZ})$ ratio;

- The $\alpha(M_{VZ})$ ratio is less sensitive to mismodeling of the matrix element calculation for the background and to theory systematics (*e.g.* normalization and factorization scale, PDFs, etc) since the background composition is similar in the two regions.

The above description aims to illustrate the method employed in the analysis. The actual fits used for the background determination are performed separately

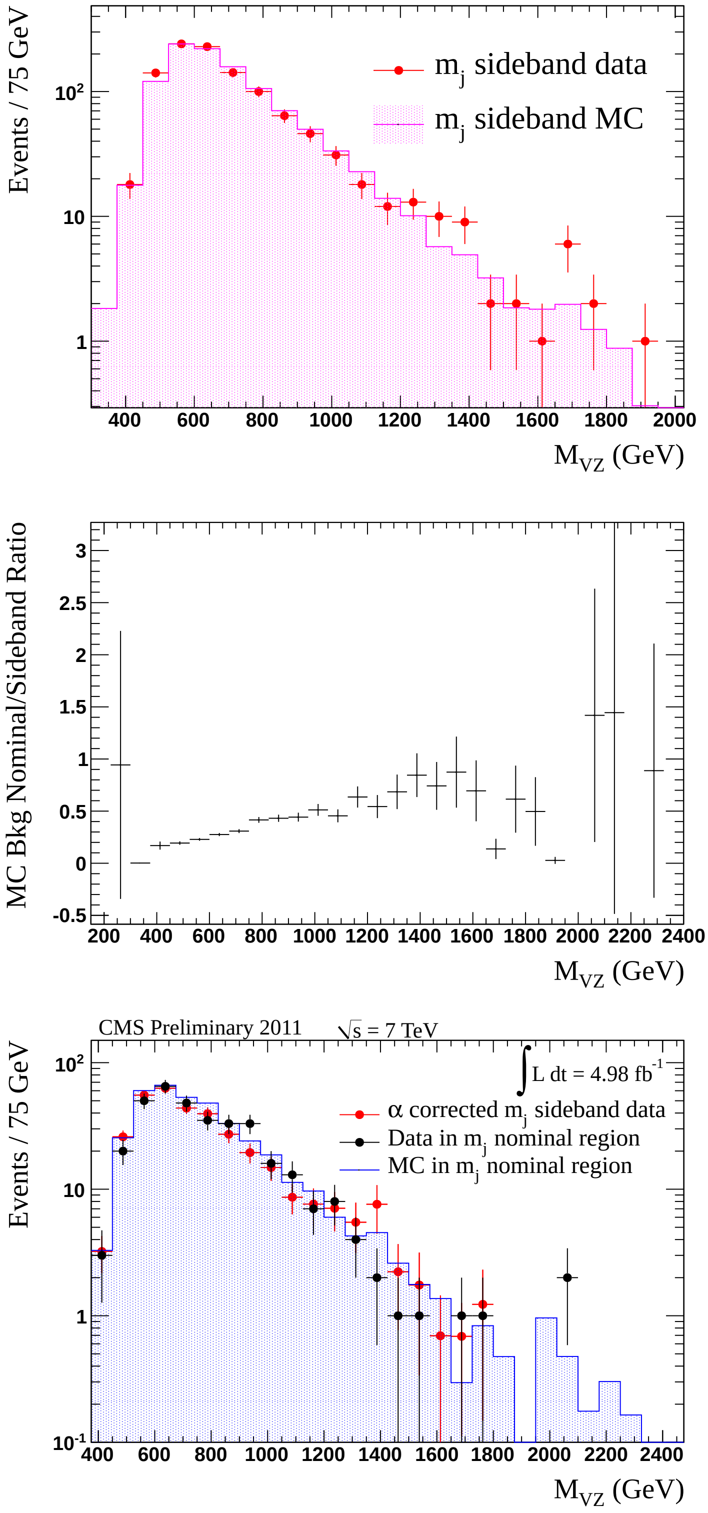

Figure 5.9: Distributions made for the electron and muon channels combined; Top: Distribution of M_{VZ} with the M_j sideband selection made with collision data (red points) and comparison with the inclusive Monte Carlo background (pink histogram) for the same selection. Center: The differential $\alpha(M_{VZ})$ ratio as determined by using MC-based background distributions with the nominal and sideband selections. Bottom: The comparison of the estimated background determined as described in the text (red points) with the total MC background (blue histogram) and the data (black points) M_{VZ} distributions.

for the electron and muon channels, as they have different resolution and reconstruction efficiencies.

Figure 5.10 shows the $\alpha(M_{VZ})$ distributions for the electron (left) and the muon (right) channels. The ratios are used to derive the estimated background distribution, as explained above, for the two channels individually. These derived distributions are then fit with the following function

$$f_A(M_{VZ}) = p_0 \frac{\left[1 - \left(\frac{M_{VZ}}{\sqrt{s}}\right)\right]^{p_1}}{\left(\frac{M_{VZ}}{\sqrt{s}}\right)^{p_2 + p_3 \log\left(M_{VZ}/\sqrt{s}\right)}} \tag{5.2}$$

where $\sqrt{s}$ is the center of mass energy, p_0, p_1, p_2 and p_3 are free parameters, and M_{VZ} is expressed in GeV.

Figures 5.11 and 5.12 on the top shows the fit on the derived M_{VZ} distribution (red points) in the electron and muon channels, respectively, and its comparison with the inclusive MC background with the nominal selection (blue histogram), as well as the data with the nominal selection (black points). The fit determines both the shape and the overall normalization of the expected background as a function of M_{VZ}. The fitting range is $350 < M_{VZ} < 2300$ GeV/c^2 for both electron and muon channels. The fitting functions are then used to describe the expected background in any subregion of the M_{VZ} spectrum.

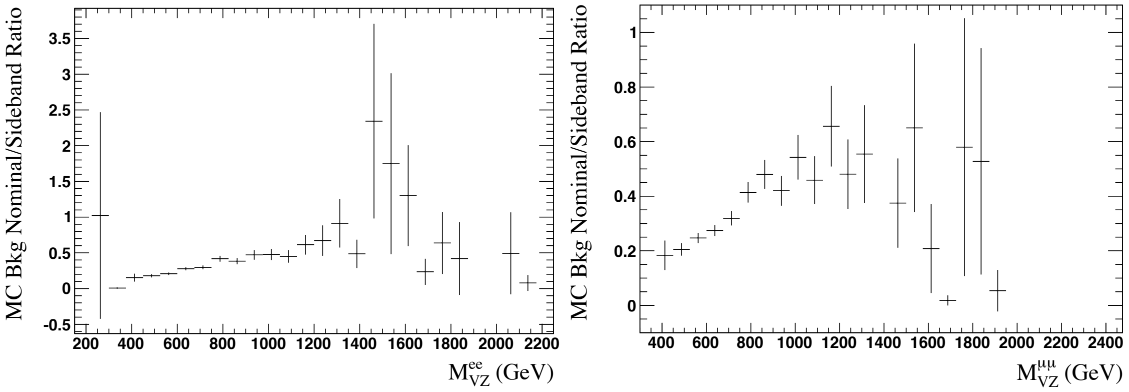

Figure 5.10: The differential $\alpha(M_{VZ})$ ratios as determined by using MC-based background distributions with the nominal and sideband selections for the electron (left) and muon (right) channels.

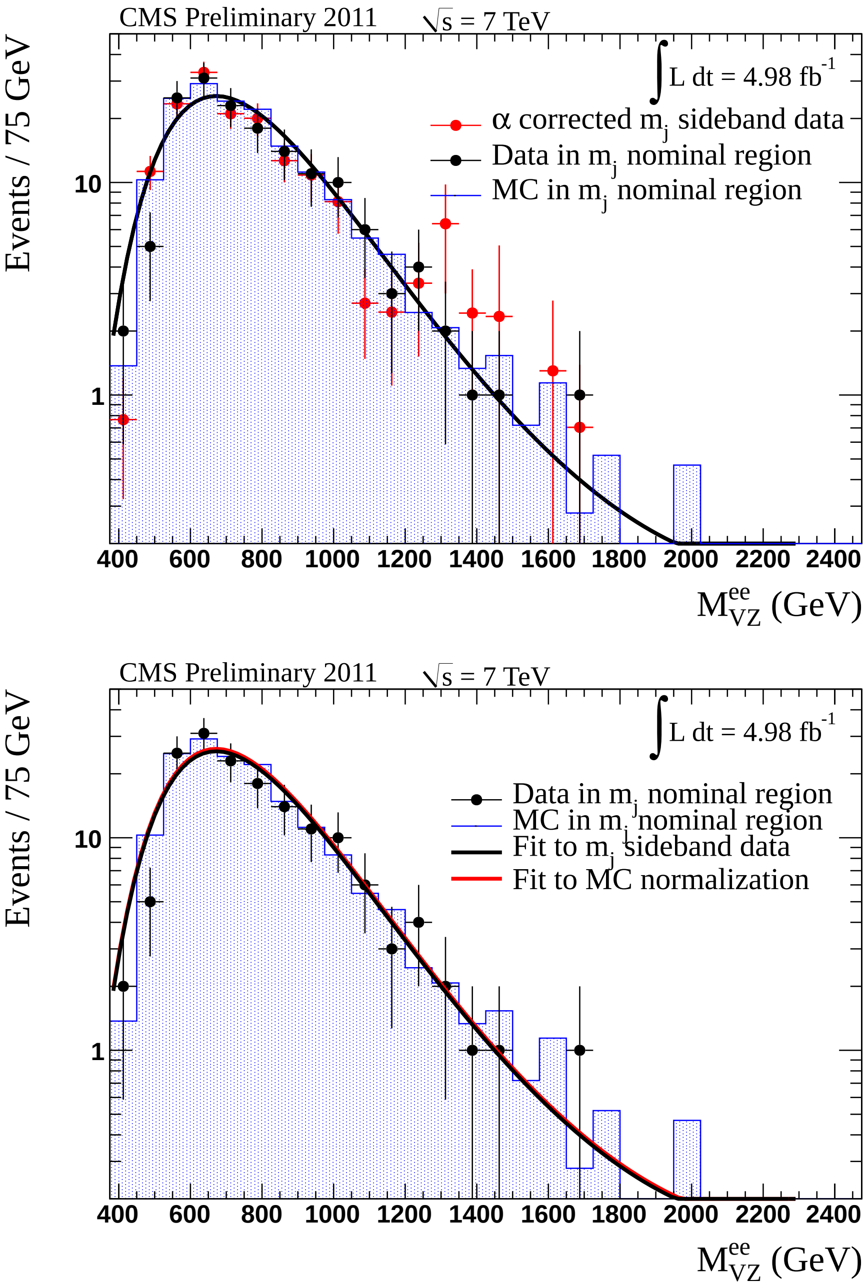

Figure 5.11: Electron channel; Top: fit on the derived M_{VZ} distribution (red points) as explained in the text. Bottom: comparison of the fitting function as determined from the top plot (black line) and a “renormalized” fitting function that gives the best match to the MC background distribution. The distributions for the inclusive MC background (blue histogram) and the data (black points) produced with the nominal selection are also shown.

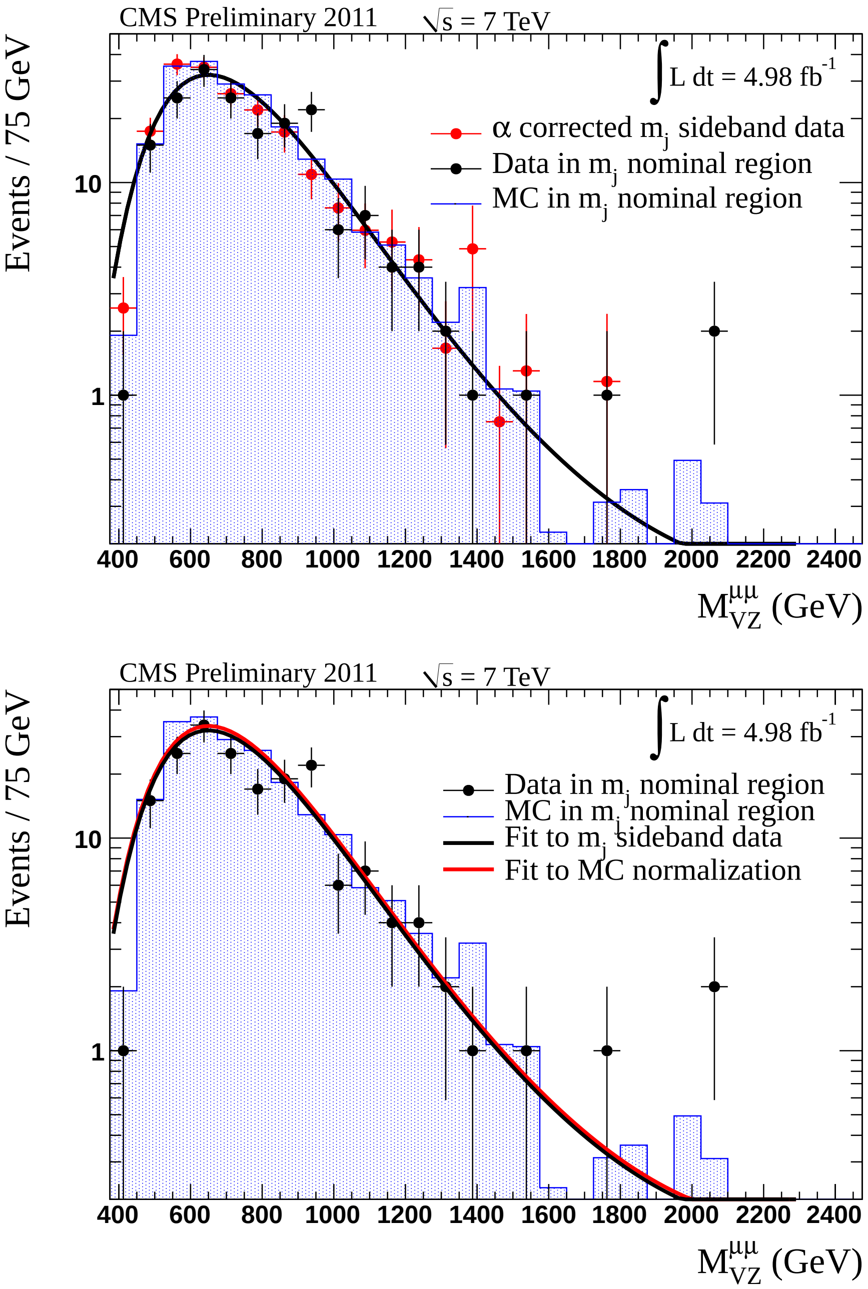

Figure 5.12: Muon channel; Top: fit on the derived M_{VZ} distribution (red points) as explained in the text. Bottom: comparison of the fitting function as determined from the top plot (black line) and a "renormalized" fitting function that gives the best match to the MC background distribution. The distributions for the inclusive MC background (blue histogram) and the data (black points) produced with the nominal selection are also shown.

5.4.2 Background Cross-checks

Closure Test

In order to show that the background method correctly describes the M_{VZ} distribution a closure test is performed:

- The Z and V p_T cuts are relaxed to increase the statistics of the data samples;
- The jet mass sideband is split into two: the "higher sideband" ($50 < M_j < 65$ GeV/c^2) and the "lower sideband" ($30 < M_j < 50$ GeV/c^2) regions;
- The $\alpha(M_{VZ})$ is computed from simulation and used to correct the "lower sideband" data, then compared to the "higher sideband" data.

The result is shown in Fig. 5.13 for the electron (top), muon (center) and combined channels (bottom). The combined channels event yields for the two selections are consistent with each other: 549 ± 23 [545 ± 31] for the higher sideband [$\alpha(M_{VZ})$-corrected lower sideband] yields. When the closure test is performed in the separated channels, the yields are 266 ± 16 [260 ± 23] in the higher sideband [$\alpha(M_{VZ})$-corrected lower sideband] for the electron channel and 283 ± 17 [286 ± 22] for the muon channel. The closure test shows satisfactory agreement between the predicted and observed distributions, both in terms of shape and overall normalization. This demonstrates that one can use one region of the (sideband) M_{VZ} spectrum to describe another region by using the MC-calculated $\alpha(M_{VZ})$ ratio, and therefore that this method can be used as a background estimation method.

Comparison with MC–based Estimates

An additional cross-check is to fit the inclusive MC background M_{VZ} distribution for the nominal selection with function f_A whose parameters have been fixed to the results of the previous step, with the exception of an overall normalization factor. The bottom plots in Figs. 5.11 and 5.12 show these "normalization" fit results: the black line corresponds to f_A without any additional scaling, and the red line is the "renormalized" f_A that gives the best match to the MC background distribution (blue histogram). The data distributions for the nominal selection (black points) are also shown. This exercise allows to see the relative difference between the data driven prediction on the background (black curve) and the Monte Carlo expectation (red curve). This difference is 2.2 ± 7.9% for the electron channel and 0.98 ± 0.07% for the muon channel. The difference between the MC–based

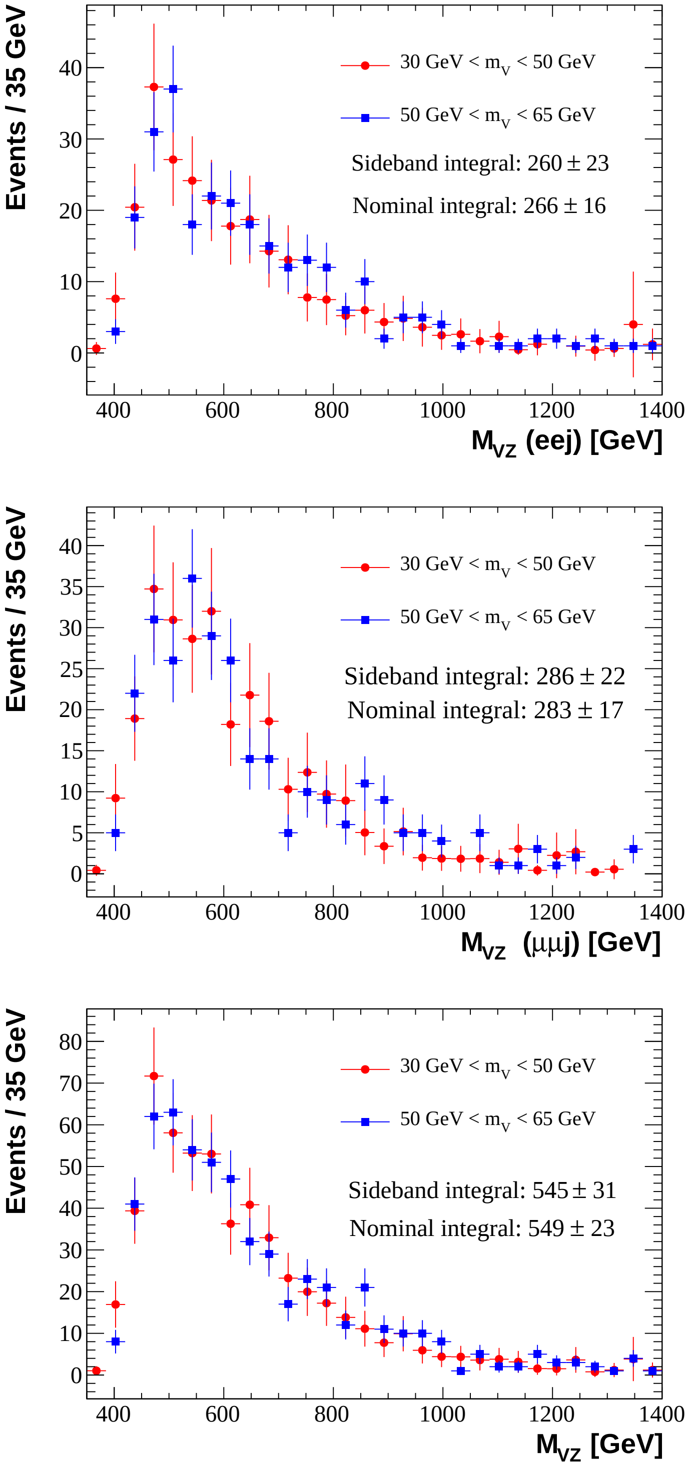

Figure 5.13: Comparison between "higher sideband" ($50 < M_j < 65$ GeV/c^2, blue) and the $\alpha(M_{VZ})$-corrected "lower sideband" ($30 < M_j < 50$ GeV/c^2, red) M_{VZ} data spectra, for electron (top), muon (center) and combined (bottom) channels. The good matching between the two distributions demonstrates that one can use one region of the sideband M_{VZ} region and the $\alpha(M_{VZ})$ ratio to describe another M_{VZ} region.

and data–driven estimates is considered as a systematic uncertainty in the determination of the expected background in the M_{VZ} distributions for each channel individually.

Background Fit - Exponential Function

The choice of the background fit function f_A is motivated by the dijet mass spectrum analysis. However, to cross check, alternative functions were considered. In this section the fit performance of the exponential function is shown. The same procedure employed for the main analysis was followed. Fig. 5.14 shows the results for the electron (left) and muon (right) channels, and should be compared to the baseline fit shown in Figs. 5.11 and 5.12. The performance is similar to the one obtained for the fit carried out with the nominal f_A function — the yields in each mass window considered were compatible within 1σ with the ones obtained using f_A.

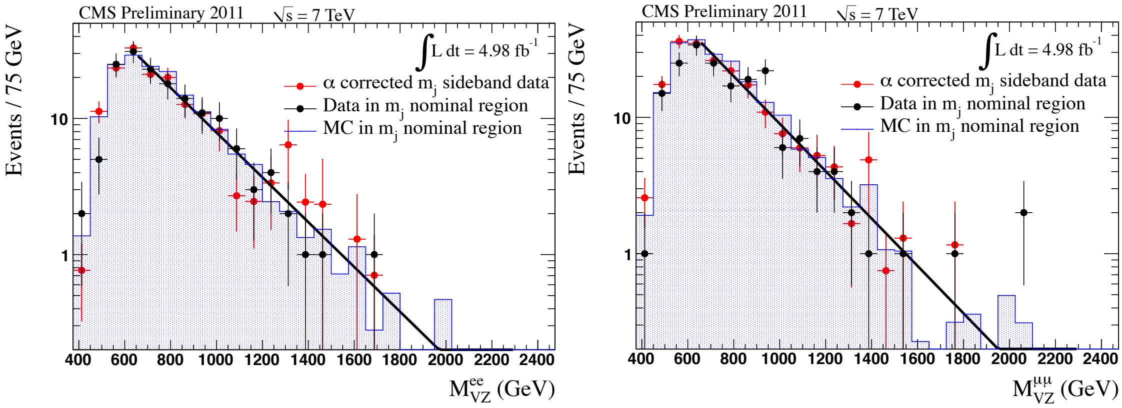

Figure 5.14: Fit on the derived M_{VZ} distribution (red points) as explained in the text for the electron (left) and muon (right) channels. The distributions for the inclusive MC background (blue histogram) and the data (black points) are also shown.

Choice of Sideband Region

The sensitivity on the choice of the sideband region is checked, by performing the background estimation procedure for a different M_j sideband range: $50 < M_j < 65$ GeV/c^2. The event yields are then compared to the ones obtained with the original $30 < M_j < 65$ GeV/c^2 sideband range. The fits for the $50 < M_j < 65$ GeV/c^2 sideband region are shown in Fig. 5.15 for the electron (left) and muon (right) channels. The event yields for the original sideband ($30 < M_j < 65$ GeV/c^2) are compatible within uncertainties with the ones obtained by the alternative range. The $M_j > 120$ GeV/c^2 region was also considered, but does not have enough statistics for a stable fit and a solid background estimate.

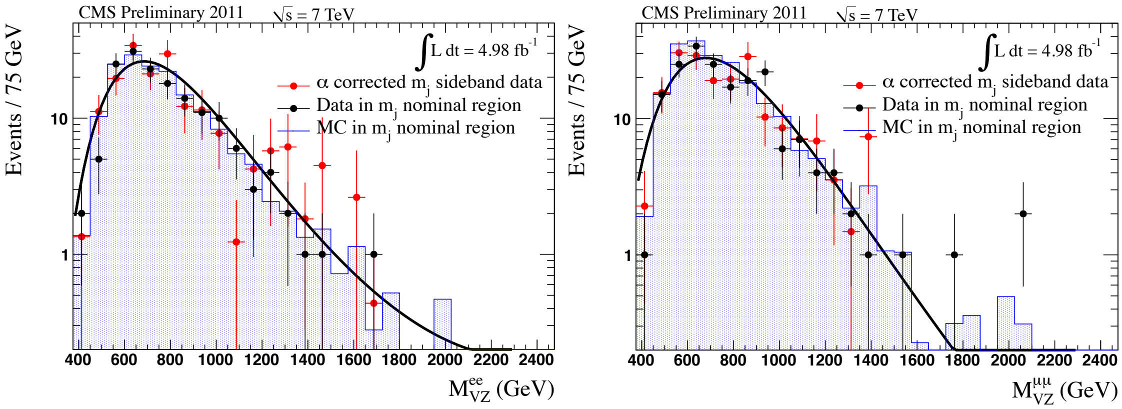

Figure 5.15: Fit on the $\alpha(M_{VZ})$-corrected data spectrum for the alternative $50 < M_j < 65$ GeV/c^2 sideband region. The derived M_{VZ} distribution (red points) was obtained according to the explanation in the text. The distributions for the inclusive MC background (blue histogram) and the data (black points) are also shown.

Choice of Fitting Range

The sensitivity to the fitting range is checked, varying the M_{VZ} region where the fit is performed. To test the sensitivity on the choice of the fitting range, we repeat the data-driven background estimation procedure for a different M_{VZ} range: 600 - 1800 GeV/c^2.

The event yields are then compared to the ones obtained with the nominal fitting range (350 - 2300 GeV/c^2) and found to be consistent within uncertainties. The fit is shown in Fig. 5.16 left (right) for the electron (muon) channel.

A different M_{VZ} fitting range was also tried that covers only partially the turn-on region: 450 - 1800 GeV/c^2.

The event yields are then compared to the ones obtained with the nominal fitting range (350 - 2300 GeV/c^2) and found to be consistent within uncertainties. The fit is shown in Fig. 5.17 left (right) for the electron (muon) channel.

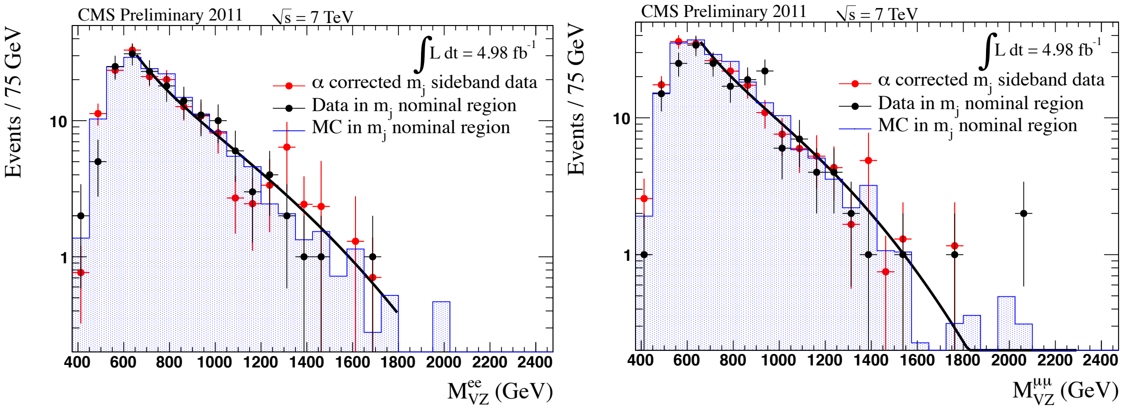

Figure 5.16: Fits on the $\alpha(M_{VZ})$-corrected data M_{VZ} spectra (red points) using an alternative fitting range (650-1800 GeV/c^2) which excludes the turn-on region for the electron (left) and the muon (right) channels. The distributions for the inclusive MC background (blue histogram) and the data (black points) are also shown.

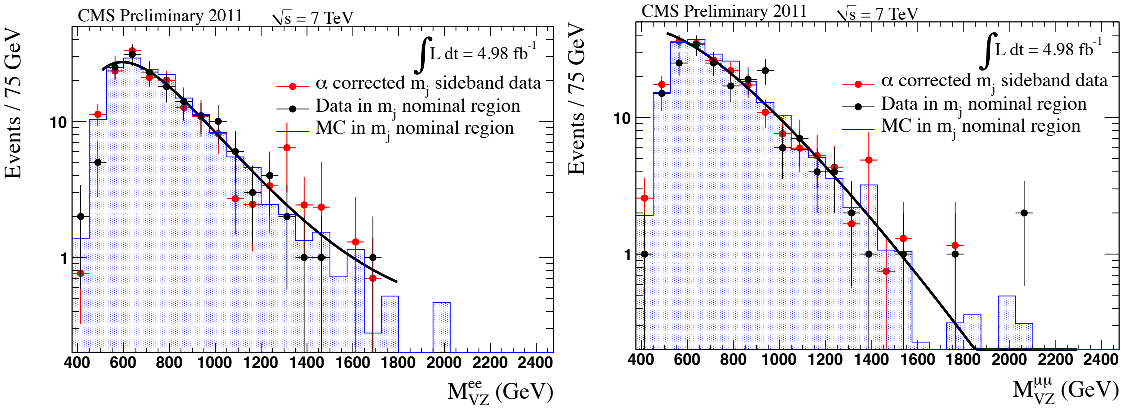

Figure 5.17: Fits on the $\alpha(M_{VZ})$-corrected data M_{VZ} spectra (red points) using an alternative fitting range (450-1800 GeV/c^2) which covers only partially the turn-on region for the electron (left) and the muon (right) channels. The distributions for the inclusive MC background (blue histogram) and the data (black points) are also shown.

5.5 Local Significance of the Excess in the Muon Channel

The discrepancy observed in the muon channel can be quantified by interpreting it as a resonant peak and calculating its local significance. The "signal" is modeled by a Gaussian with a mean of 920 GeV/c^2, being the value of the most significant local excess, and a width of 46 GeV/c^2, corresponding to the reconstructed signal width derived with MC simulation. A simple shape analysis is performed by calculating the binned likelihood of the observed data sample under the pdf given by

$$f(M_{VZ}; R_s, R_b) = R_s * \mathrm{Gauss}(M_{VZ}; M, \Gamma) + R_b * f_A(M_{VZ}) \ , \tag{5.3}$$

where $f_A(M_{VZ})$ is given in Eq. 5.2 with the parameters fixed at the values obtained in the fit to the sideband region, $M = 920$ GeV/c^2 and $\Gamma = 46$ GeV/c^2.

This is computed by first fixing R_b to one and R_s to zero (which corresponds to the background-only hypothesis: H_0), and then by letting R_s float (which corresponds to the signal-plus-background hypothesis: H_1) and performing a maximum likelihood fit to obtain the optimal value of R_s (see Fig.5.18). According to Wilks' theorem, the likelihood ratio $z = -2 \ln \mathcal{L}_{\mathrm{B}} / \mathcal{L}_{\mathrm{S+B}}$ is asymptotically distributed as a χ^2 distribution with number of degrees of freedom equal to the additional numbers of free parameters when going from H_0 to the H_1 model. Given the difference of one parameter, the likelihood ratio can be directly interpreted as "signal significance". For the above test, a value of $z = 3.0$ was obtained.

The calculation is then repeated without fixing the normalization of the background pdf R_b. The fit is performed twice, once with the signal fraction R_s set to zero and then with both parameters free (see Fig.5.19). The significance obtained without imposing background normalization is $z = 1.6$.

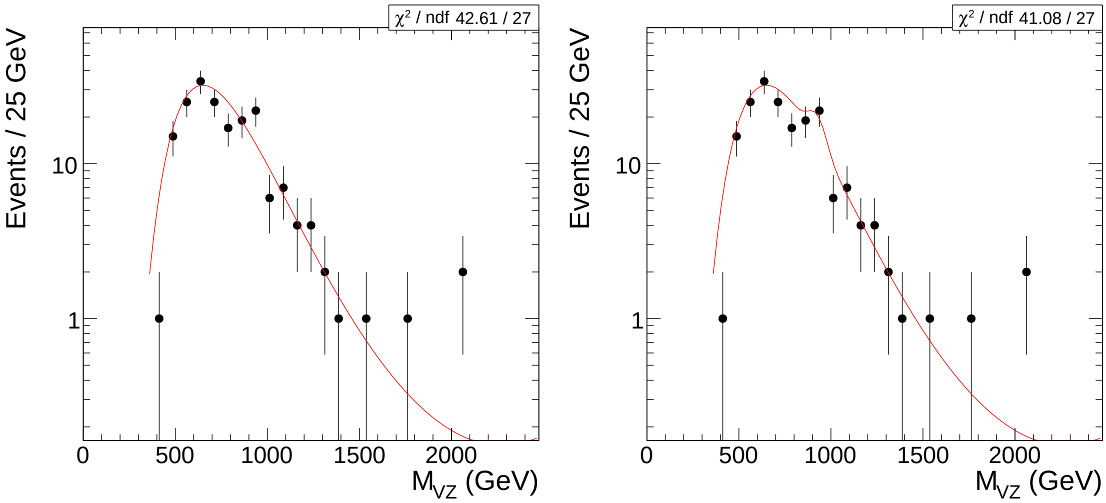

Figure 5.18: Muon channel - Fit on the $\alpha(M_{VZ})$-corrected data on the nominal ($30 < M_j < 65$ GeV/c^2) sideband region, with fixed normalization taken from the sideband. Top plot: fit of the background-only hypothesis (Eq. 5.2). Bottom plot: fit of the signal-plus-background hypothesis, with the signal being modeled by a Gaussian with a mean of 900 GeV/c^2 and a width of 46 GeV/c^2.

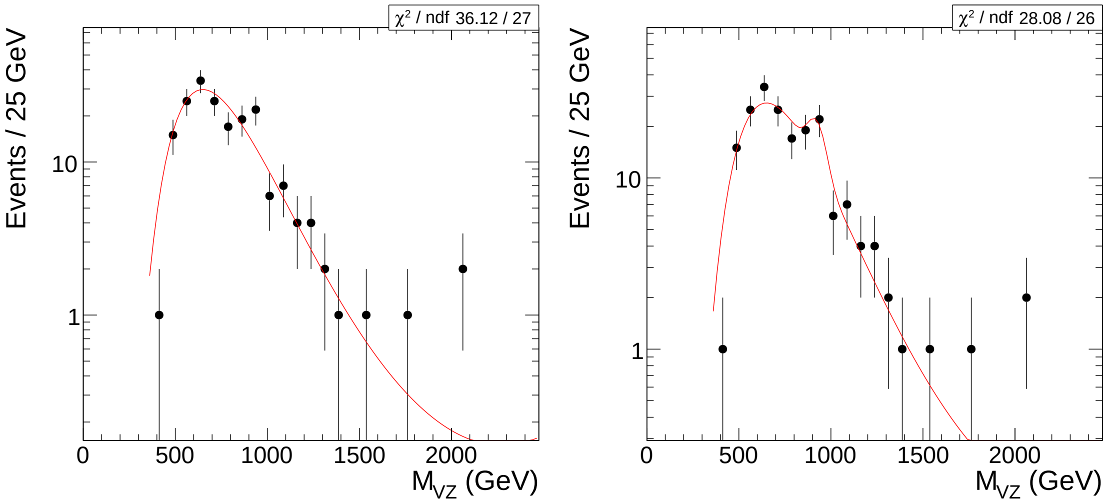

Figure 5.19: Muon channel - Fit on the $\alpha(M_{VZ})$-corrected data on the nominal ($30 < M_j < 65$ GeV/c^2) sideband region, with normalization made free to best fit the data. Top plot: fit of the background-only hypothesis (Eq. 5.2). Bottom plot: fit of the signal-plus-background hypothesis, with the signal being modeled by a Gaussian with a mean of 920 GeV/c^2 and a width of 46 GeV/c^2.

5.6 Event Displays

We present here some event displays of the four data events with the highest VZ candidate mass, two in the electron (Figs. 5.20, 5.21) and two in the muon (Figs. 5.22, 5.23) channel. In these events, only the tracks with momentum greater than 1 $GeV/$c are shown, to avoid the figure to be busy with tracks that are not relevant in the event reconstruction.

The figures show three different views of the event in the CMS detector configuration:

- Top: the view in the $\rho - \phi$ axis. This is the transverse plane view, and it is important to have a picture of how the event objects balance their momentum in the transverse plane.
- Bottom left: the view in the $\rho - z$ axis, where z is the direction of the beam. This view shows central or forward the event objects are located in the detector.
- Bottom right: the 3D view. This view shows the three relevant coordinates and the calorimeter hits in the event. Important for the event overall overview.

The electron channel event with the highest VZ candidate mass is shown in Fig. 5.20. The VZ invariant mass is M_{VZ} = 1.7 TeV/c^2. The event shows a pair of electrons which form a Z candidate of mass M_Z = 101.7 GeV/c^2 and a jet with M_j = 66.8 GeV/c^2. The di-electron system is back to back in $\rho - \phi$ plane with respect to the massive jet.

The electron channel event with the second highest VZ candidate mass is shown in Fig. 5.21. The VZ invariant mass is M_{VZ} = 1.4 TeV/c^2. The event shows a pair of electrons which form a Z candidate of mass M_Z = 88.4 GeV/c^2 and a jet with M_j = 76.7 GeV/c^2. The di-electron system is back to back in $\rho - \phi$ plane with respect to the massive jet, and shows also an extra jet which is not very energetic. One of the electrons forming the Z candidate is extremely boosted - have a p_T^e = 630 GeV/c.

The muon channel event with the highest VZ candidate mass is shown in Fig. 5.22. The VZ invariant mass is M_{VZ} = 2.1 TeV/c^2. The event shows a pair of muons which form a Z candidate of mass M_Z = 89.0 GeV/c^2 and a jet with M_j = 77.8 GeV/c^2. The di-muon system is not back to back in $\rho - \phi$ plane with respect to the massive jet - there is an extra energetic jet (E_T^{jet2} = 560 GeV/c^2) which does not enter in the calculation of the invariant mass of the VZ candidate.

The muon channel event with the second highest VZ candidate mass is shown in Fig. 5.23. The VZ invariant mass is M_{VZ} = 2.1 TeV/c^2. The event shows a pair of muons which form a Z candidate of mass M_Z = 87.0 GeV/c^2 and a jet with M_j = 79.4 GeV/c^2. The di-muon system is back to back in $\rho - \phi$ plane with respect to the massive jet. The two muons forming the Z candidate are very close to each other - they share all the layers in the muon chambers expect the last, and their Z candidate has p_T^Z = 940 GeV/c. This event exemplify the problems working with boosted vector bosons: due to the proximity of the muons, this event could not be triggered by a double muon path, because the second leading muon didn't meet the on-line isolation requirements. This kind of boosted topology require single object triggers (such as the muon triggers used in this analysis) or special double lepton trigger paths with very loose identification requirement and no isolation. The second kind of specialized trigger is present in the 2012 menu, and will be used in the update of this analysis with 2012 dataset.

The events in Figs. 5.22 and 5.23 are very close in VZ candidate mass and correspond to the two events in the same mass bin in the VZ mass distribution in the muon channel, in the bottom plot of Fig. 5.6. However, this two events in the same bin doesn't correspond to a significant excess, because any resonance, even very narrow, would suffer from detector resolution effects. The resolution for the VZ mass in the 2 TeV/c^2 range is $\sim$ 100 GeV/c^2, and the lack of events in the tails of that bin makes the local significance test using shape analysis, similar to that performed on Sec. 5.5, to yield an excess smaller than 1σ.

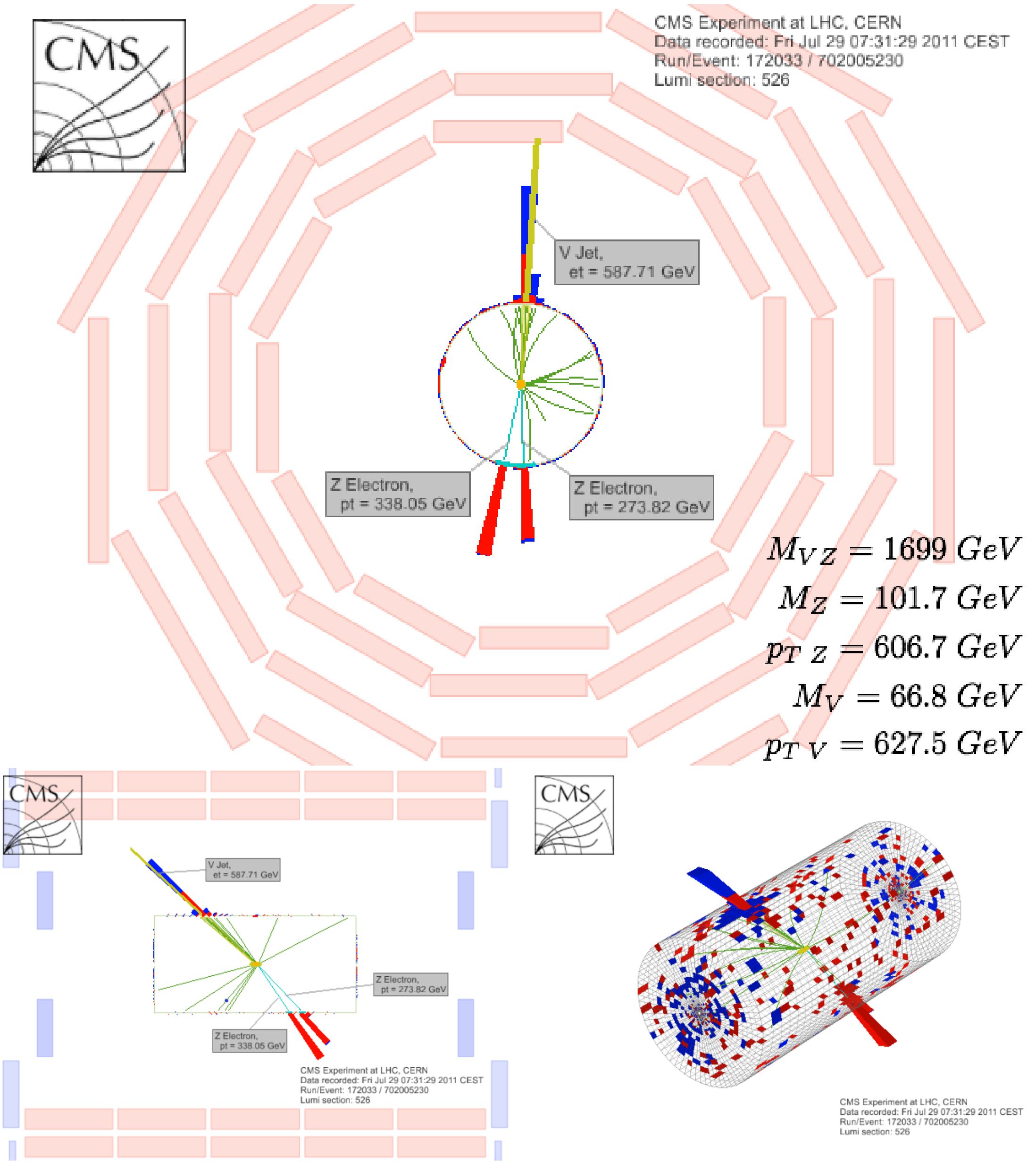

Figure 5.20: Event(172033:702005230:526) passing all baseline analysis cuts. The VZ invariant mass is 1699 GeV/c^2.

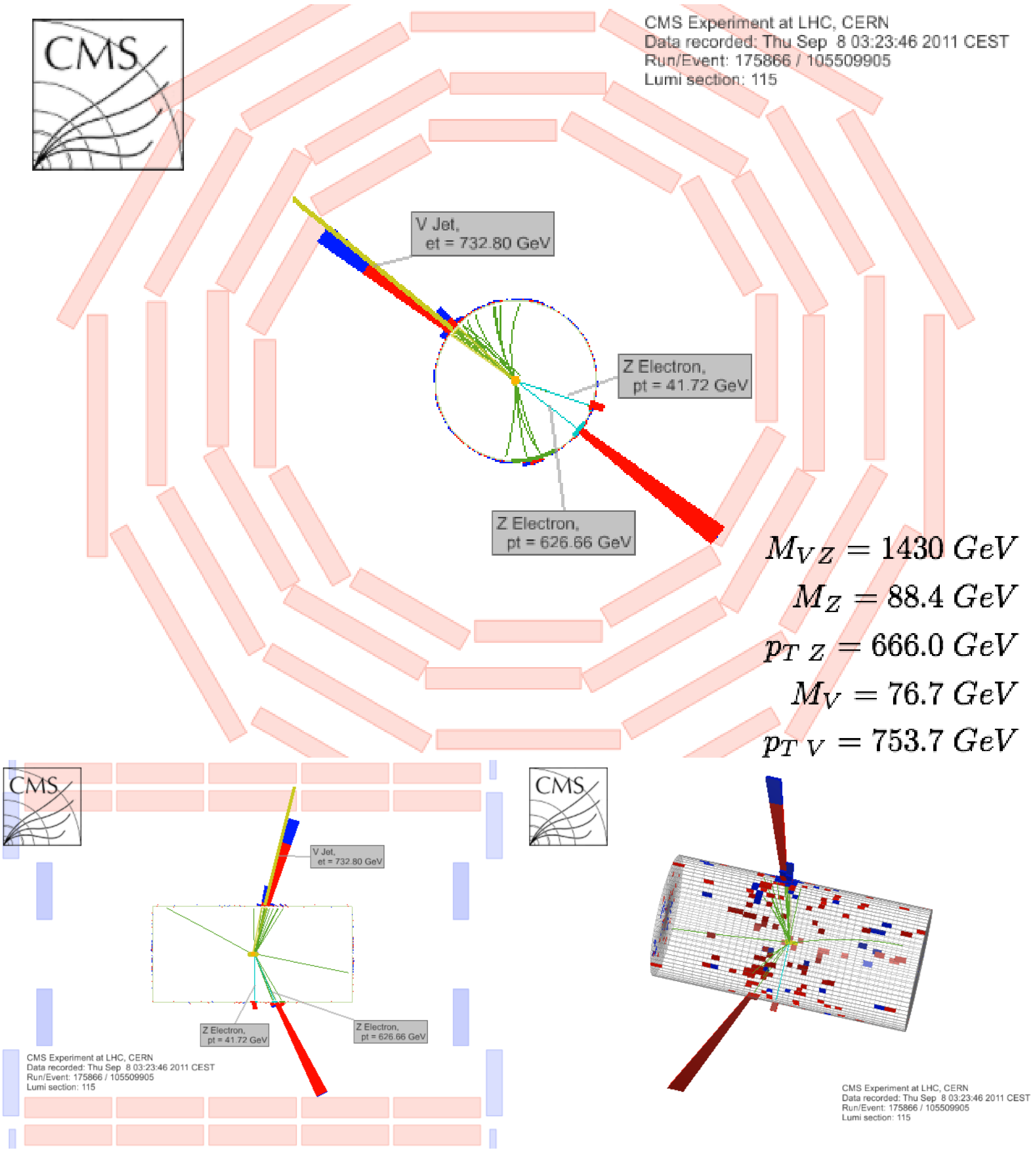

Figure 5.21: Event(175866:105509905:115) passing all baseline analysis cuts. The VZ invariant mass is 1430 GeV/c^2.

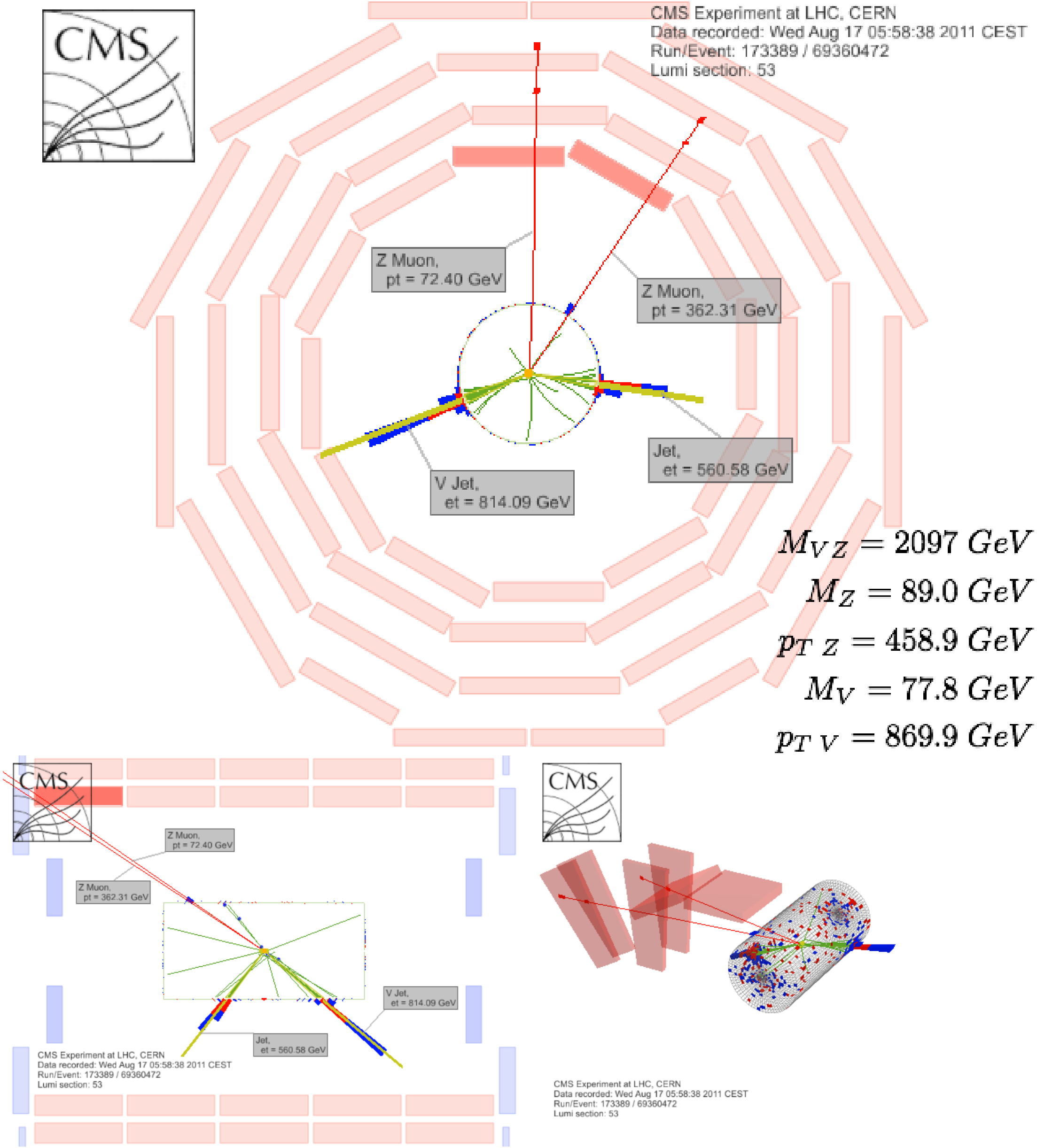

Figure 5.22: Event(173389:69360472:53) passing all baseline analysis cuts. The VZ invariant mass is 2097 GeV/c^2.

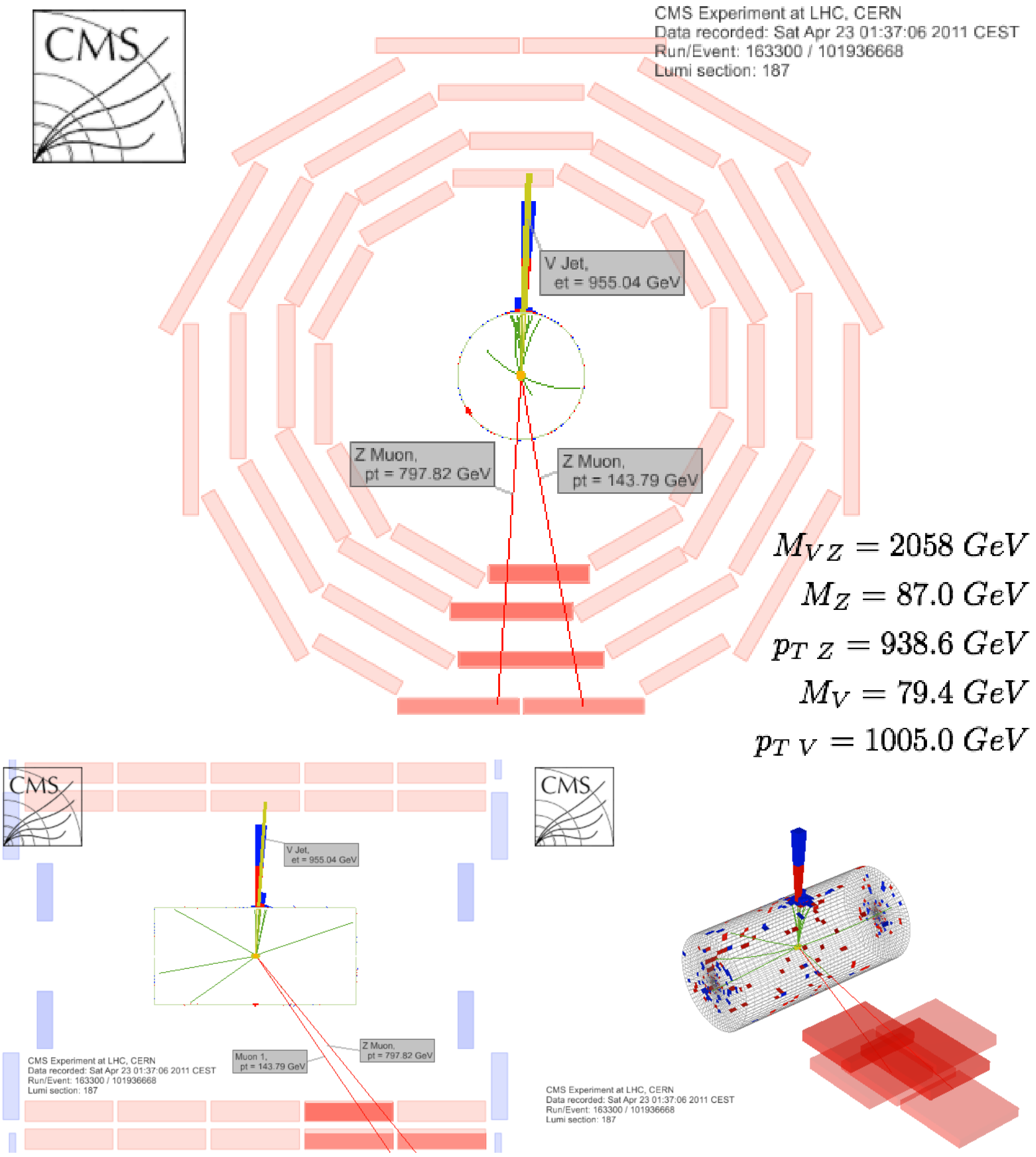

Figure 5.23: Event(163300:101936668:187) passing all baseline analysis cuts. The VZ invariant mass is 2058 GeV/c^2.

5.7 Systematic Uncertainties

The systematic uncertainties considered in this analysis can be divided into two main categories: the uncertainty in the determination of the SM background and the uncertainty in the expected yields of signal events.

5.7.1 Background

The background determination procedure was described in Sec. 5.4. As the method employed for the background determination is derived from data, several of the usual systematic effects (*e.g.* parton density function, integrated luminosity) are eliminated.

The number of expected background events in each mass window is determined by the integral of the function $f_A(M_{VZ})$ in that range. The statistical uncertainty is calculated by employing the full covariance error matrix of the fit parameter errors in the integral of the fitting function in the mass window. Several variations in the fitting procedure (fitting range, functional form and sideband definition) are considered, as well as the difference in the number of expected background events in the mass window as estimated by the data-driven and the MC-based methods. The largest variation observed in each case is taken as the systematic uncertainty in the background determination.

The pile-up and jet energy scale (JES) systematics can potentially affect the background determination through the $\alpha(M_{VZ})$ ratio and were considered separately. The former is found to have a negligible effect. For the latter, the uncertainty is evaluated by scaling up and down every jet p_T by the total uncertainty $\sigma_{JES} = \sigma_{JES}(p_T, \eta)$. For a given jet candidate, its transverse momentum is modified as $p_T' \rightarrow p_T \pm \sigma_{JES}$, and then the full fitting procedure is applied. The yield differences, in each mass window, between the $N_{\mathrm{Bgd/up}}$ and $N_{\mathrm{Bgd/down}}$ with respect to the nominal selection and fit are taken as the $\pm 1\sigma$ estimates for the JES systematic uncertainty.

5.7.2 Signal

For the expected signal yields, the systematic uncertainties considered are:

- Luminosity
- Jet Energy Scale

- Parton Density Function
- Reconstruction efficiencies

All the systematic uncertainties are summarized in Tables 5.11–5.13. For both the background systematic uncertainties in the electron (muon) channels presented in Tables 5.11 (Tables 5.12) it is shown the number of expected background events (column 3) for a given mass point (column 1) and optimized mass window (column 2). The statistical uncertainty as determined by the fit can be found in column 4. The impact of several variations in the fitting procedure is reported in column 5, as well as the difference between the data-driven and MC-based background estimates, which is reported in column 6. Column 7 reports the uncertainty related to JES. The maximum of columns 5, 6 when combined with column 7 give the total systematic uncertainty. The combined statistical and systematic uncertainty is reported in column 8.

In Tables 5.13 the signal systematic uncertainties are presented for a given mass point (column 1) and optimized mass window (column 2), the jet energy scale uncertainties are reported in column 3 (4) for the electron (muon) channel. Column 5 reports the PDF uncertainty. In addition, flat uncertainties are considered on the integrated luminosity (2.2%) and the reconstruction and trigger efficiencies as determined by the tag and probe method (2%) and the V mass cut as determined by a sample of $t\bar{t}$ events (9%).

The total systematic uncertainty is the combination of all the above, assuming they are completely uncorrelated. An uncertainty of 2.2% [80] was assumed in the measurement of the integrated luminosity.

For the jet energy scale, the procedure of scaling up and down every jet p_T by the total uncertainty $\sigma_{JES} = \sigma_{JES}(p_T, \eta)$ is repeated, and then the full analysis selections are reapplied. The differences in the signal yields $N_{\mathrm{sig/up}}$ and $N_{\mathrm{sig/down}}$ with respect to the nominal selection N_{sig} are taken as the $\pm 1\sigma$ estimates for the JES systematic uncertainty. For W' and RS particles with mass in the range [700, 2000] GeV/c^2, this systematic uncertainty is smaller than 1%.

To estimate the systematic uncertainty in the choice of the parton density function (PDF) used for the simulated samples, the software module `PDF Weight Producer` was employed. Three PDF scenarios were considered: CTEQ6.6, MSTW 2008 and NNPDF2.0 [81]. The systematic uncertainty is set to half of the difference between the maximum and the minimum PDF values predicted for each mass point [82]. The studies for the signal PDF systematic uncertainties for W' mass

Table 5.11: Background systematic uncertainties in the electron channel.

Mass point GeV/c^2	Mass Window GeV/c^2	$N_{\rm bgd}$	$\delta N_{\rm bgd}$ (stat)	Fit variations	Diff. w/ MC	$\delta N_{\rm bgd}$ (JES)	$\delta N_{\rm bgd}$ (tot)
W' model							
700	640-760	39.7	3.3	1.3	0.3	1.5	3.9
800	755-845	24.6	2.0	5.2	4.0	1.2	5.7
900	855-945	17.1	1.6	3.6	2.6	1.3	4.2
1000	930-1070	17.1	1.8	2.9	0.9	0.4	3.5
1100	1020-1180	12.0	1.5	2.6	0.5	0.3	3.0
1200	1130-1270	6.2	0.9	1.6	0.4	0.5	1.9
1300	1220-1380	4.4	0.7	2.0	0.3	1.8	2.8
1400	1320-1480	2.7	0.5	1.7	0.7	0.4	1.8
1500	1390-1610	2.5	1.6	1.8	0.7	1.1	2.2
RS model							
750	690-810	37.1	3.0	5.2	1.0	0.6	6.0
1000	940-1060	14.6	1.5	2.5	0.7	1.1	3.1
1250	1180-1320	4.9	0.8	1.7	0.1	0.4	1.9
1500	1390-1610	2.5	0.6	1.8	0.7	0.6	2.0
1750	1540-1960	2.0	0.6	1.3	0.2	1.0	1.7
2000	1760-2240	1.3	0.5	0.5	0.3	1.4	1.6

points in the range of 300 – 3500 GeV/c^2 are documented in [83]. The values for the signal PDF systematic uncertainties for Randall-Sundrum mass points in the range of 750 – 2000 GeV/c^2 can be found in [77].

The expected signal yields are calculated by using simulated W' and RS samples and the analysis cuts discussed in Sec. 5.3. To account for differences in trigger and reconstruction efficiencies between Monte Carlo and data, scaling factors were determined by employing the standard "tag and probe" technique [69, 84] using samples of $Z \to \mu\mu$ and $Z \to ee$ candidate events. Corrections were derived for the muon (0.974 ± 0.001) and the electron (0.960 ± 0.004) channels and applied on the expected signal yields. Even though these numbers assume a flat efficiency, a small decrease (increase) in the efficiency in the asymptotic high-p_T(high-$E_{\rm T}$) region for muons (electrons) of about 2% is observed. This small difference is used

Table 5.12: Background systematic uncertainties in the muon channel.

Mass point GeV/c^2	Mass Window GeV/c^2	$N_{\rm bgd}$	$\delta N_{\rm bgd}$ (stat)	Fit variations	Diff. w/ MC	$\delta N_{\rm bgd}$ (JES)	$\delta N_{\rm bgd}$ (tot)
W' model							
700	640-760	48.7	3.6	5.0	1.1	2.0	8.9
800	755-845	28.6	2.2	5.3	0.3	1.6	6.9
900	855-945	19.2	1.6	3.1	1.0	0.2	4.3
1000	930-1070	18.7	1.9	2.8	0.2	1.5	3.7
1100	1020-1180	12.9	1.5	2.5	0.2	1.1	3.1
1200	1130-1270	6.7	0.9	1.9	0.9	1.4	2.2
1300	1220-1380	4.6	0.7	2.0	1.0	1.4	2.1
1400	1320-1480	2.9	0.5	1.4	1.7	2.0	2.0
1500	1390-1610	2.6	0.6	1.2	1.1	1.4	1.7
RS model							
750	690-810	44.1	3.2	6.3	0.7	3.0	9.2
1000	940-1060	15.9	1.6	2.4	1.0	1.2	3.4
1250	1180-1320	5.2	0.8	1.9	0.2	0.0	2.1
1500	1390-1610	2.6	0.6	1.2	1.4	0.6	1.6
1750	1540-1960	2.1	0.6	0.7	0.7	1.1	1.4
2000	1760-2240	1.3	0.5	0.8	0.3	1.6	1.9

as the systematic uncertainty in the expected number of signal events for each mass point considered in this study.

Finally, a 9% systematic uncertainty on the V mass cut efficiency is assigned. This is determined by studying an independent sample of boosted $t\bar{t} \rightarrow WbWb$ events in which one of the W bosons decays into leptons and the other into hadrons. The procedure is as follows.

The monojet $V \rightarrow q\bar{q}$ reconstruction technique is efficient for boosted VZ topologies (see Fig. 5.3). For less boosted topologies, the V boson decays tend to give two distinct jets. Picking the leading-p_T jet and calling it a V boson candidate results in a mass distribution with two distinct peaks (see Fig. 5.3 top). The first one at the nominal V mass ($\sim$ 90 GeV/c^2) corresponds to the events for which the monojet approach is successful. The second one (at $\sim$ 30 GeV/c^2) corresponds to

Table 5.13: Signal systematic uncertainties.

		Electron	Muon	
Mass point GeV/c^2	Mass Window GeV/c^2	JES (%)	JES (%)	PDF (%)
W' model				
700	640-760	0.8	0.8	4.2
800	755-845	0.7	0.6	4.6
900	855-945	0.3	0.5	5.1
1000	930-1070	0.1	0.6	5.7
1100	1020-1180	0.5	0.6	6.1
1200	1130-1270	0.5	0.7	6.5
1300	1220-1380	0.6	0.6	7.3
1400	1320-1480	0.8	0.4	7.8
1500	1390-1610	0.8	0.3	8.5
RS model				
750	690-810	0.8	0.8	4.4
1000	940-1060	0.1	0.6	5.7
1250	1180-1320	0.3	0.7	6.9
1500	1390-1610	0.8	0.4	8.5
1750	1540-1960	0.4	0.2	10.2
2000	1760-2240	0.4	0.3	11.1

the traditional topology, with two distinct jets for which the monojet approach is not optimal.

Another way to visualize the above statement is to consider the efficiency of the V candidate mass cut as a function of its p_T. Figure 5.24 made with signal MC demonstrates the expected turn-on curve and a plateau efficiency value of more than 90% for $p_T(V) > 300$ GeV/c.

In order to evaluate this plateau value with real data, $t\bar{t}$ events were considered, in which one W decays into leptons and the other one into hadrons. The idea was to evaluate the $W \to q\bar{q}'$ mass cut efficiency from the hadronic leg of the $t \to W(q\bar{q}')b$

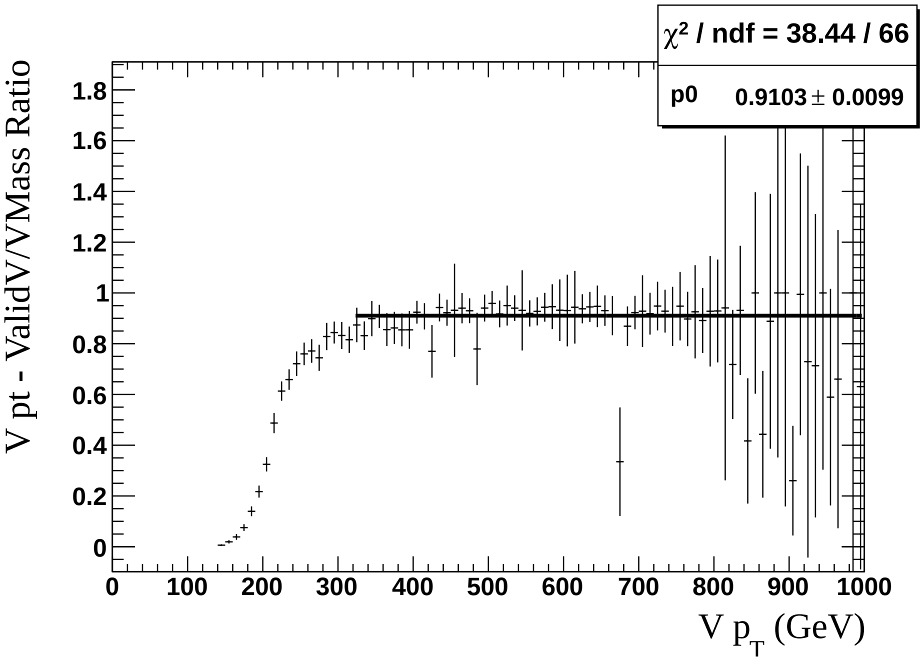

Figure 5.24: The turn on curve for efficiency on the V mass selection as a function of the V p_T, for MC signal samples.

decay. After identifying the $t \longrightarrow W(\ell\nu)b$ and $t \longrightarrow W(q\bar{q}')b$ candidates, the mass distribution of the hadronic W candidate was considered for:

- $p_T(W) > 150$ GeV/c (Fig. 5.25 top);
- $p_T(W) > 200$ GeV/c (Fig. 5.25 center);
- $p_T(W) > 250$ GeV/c (Fig. 5.25 bottom).

Two points can be made with these plots: the nominal W mass peak in the spectrum is observed as expected, which becomes more prominent for higher W p_T values; there is only a handful of events surviving the $t\bar{t}$ selection for high $p_T(W)$ thresholds. A sample of N events with an expected efficiency of 90% would give a (statistical–only) uncertainty of $\sqrt{0.9 * (1 - 0.9)/N}$, or 3% for 100 events and 7% for 20 events.

As an example, for the $p_T(W) > 250$ GeV/c sample, the following efficiencies are found for the $t\bar{t}$ dataset:

- MC: (70.2 ± 7.7) %
- Data: (72.0 ± 9.0) %

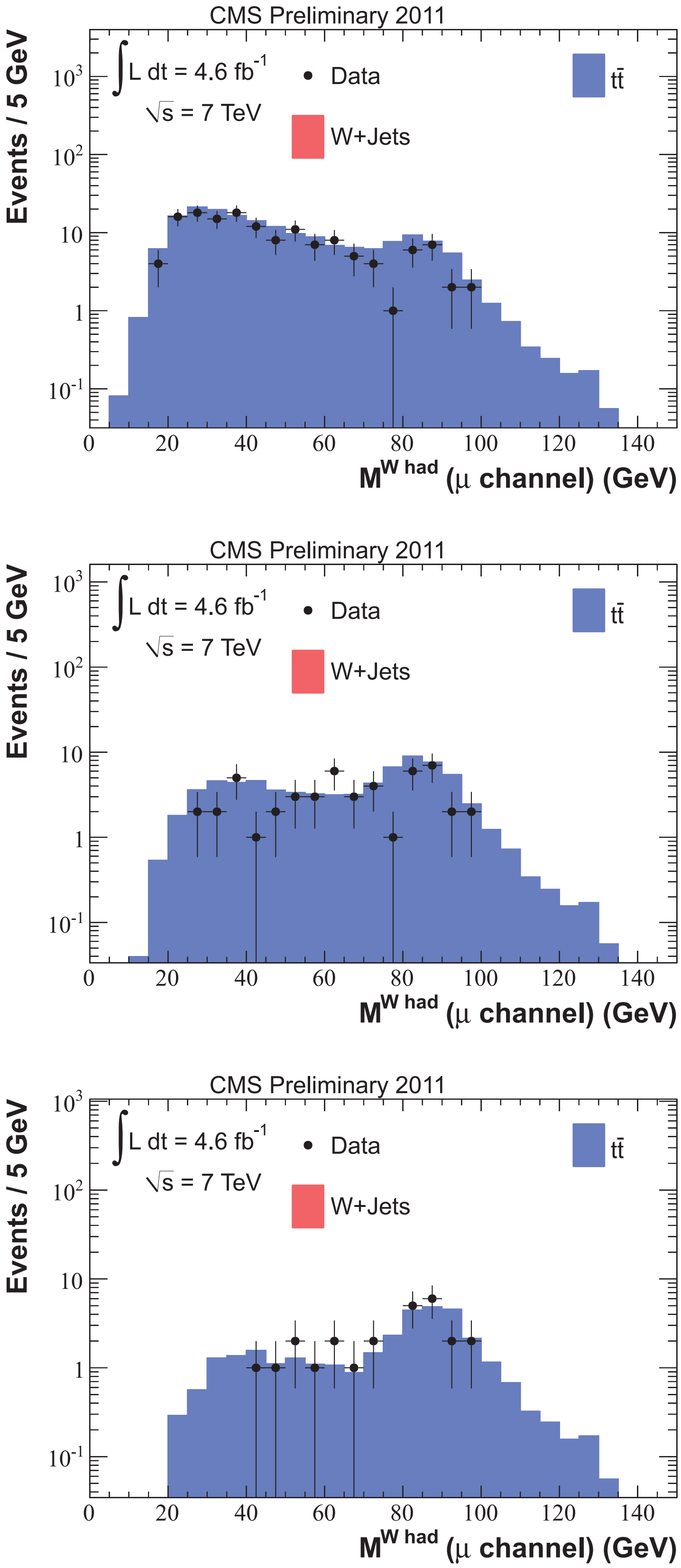

Figure 5.25: The hadronic W mass distribution, reconstructed with the monojet approach, in semileptonic $t\bar{t}$ events, for W p_T greater than 150 GeV/c (top), 200 GeV/c (center), and 250 GeV/c (bottom).

which are consistent with the V mass cut efficiency as a function of V p_T plot shown in Fig. 5.24.

Even though the method is in principle very promising, the statistics is not enough to produce a precise measurement of a potential data/MC scaling factor. This scaling factor should be very close to 1. A compromise, adopted in this analysis, is not shifting the central value in the signal reconstruction efficiency (since it cannot be determined with good precision with the current dataset), but assign a systematic uncertainty of 9%.

5.8 Results

The top plot in Fig. 5.11 (Fig. 5.12) shows the comparisons between the expected background and observed M_{VZ} distributions in the electron (muon) channel. The largest excess is observed in the muon channel in the $M_{VZ} \sim 900$ GeV/c^2 region. This is better visualized in the bottom plot of Fig. 5.26 where the ratio of the data over the expected background is shown as a function of M_{VZ}. The local significance of this excess is $z = 3.0$, as discussed in Sec. 5.5. No similar excess is observed in the electron channel (top plots of Figs. 5.26 and 5.27).

The muon excess in the $M_{VZ} \sim 900$ GeV/c^2 region is not consistent with a Z decay — an excess coming from new heavy particles decaying to VZ would have to show consistent discrepancy in both electron and muons channels. The muon-only discrepancy does not bear on the limit setting for the Randall-Sundrum gravitons or the SSM W'. That said, the following step is the limit calculation.

The modified frequentist CL$_S$ statistical method [85, 86] and a series of search windows corresponding to different mass hypotheses to search for exotic VZ resonances are employed. Each mass window is optimized to give the best exclusion limit, a procedure which is also appropriate for establishing a new resonance discovery. The results are based on the data driven background estimation described in Sec. 5.4.

The 95% confidence level exclusion limits on the combined $\sigma(VZ) \times \mathcal{B}(V \rightarrow q\bar{q},\ Z \rightarrow \ell^+\ell^-,\ \ell = e, \mu)$ product for the two final states under study (separately and combined) are calculated as a function of the mass of the hypothetical resonance. These exclusion limits are interpreted in two benchmark models: Sequential Standard Model W' and RS Graviton.

The limit setting is performed by looking for an excess over the expected background in the VZ mass distributions for the two channels separately. Tables 5.14

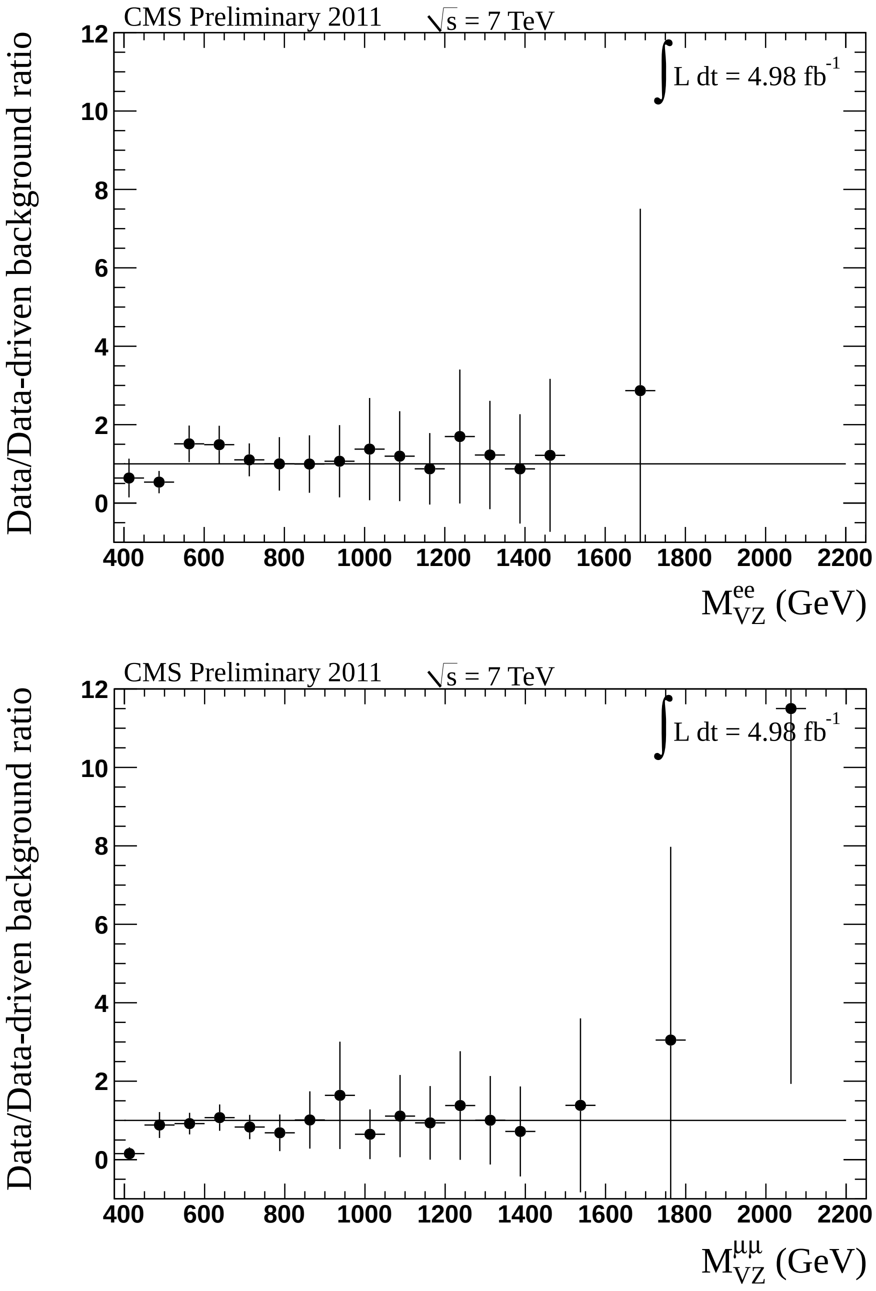

Figure 5.26: Data to expected background ratio as a function of M_{VZ} for the electron (top) and the muon (bottom) channels. The expected background is estimated with the data-driven sideband method, as discussed in Sec. 5.4.1. The error bars include both statistic and systematic uncertainties.

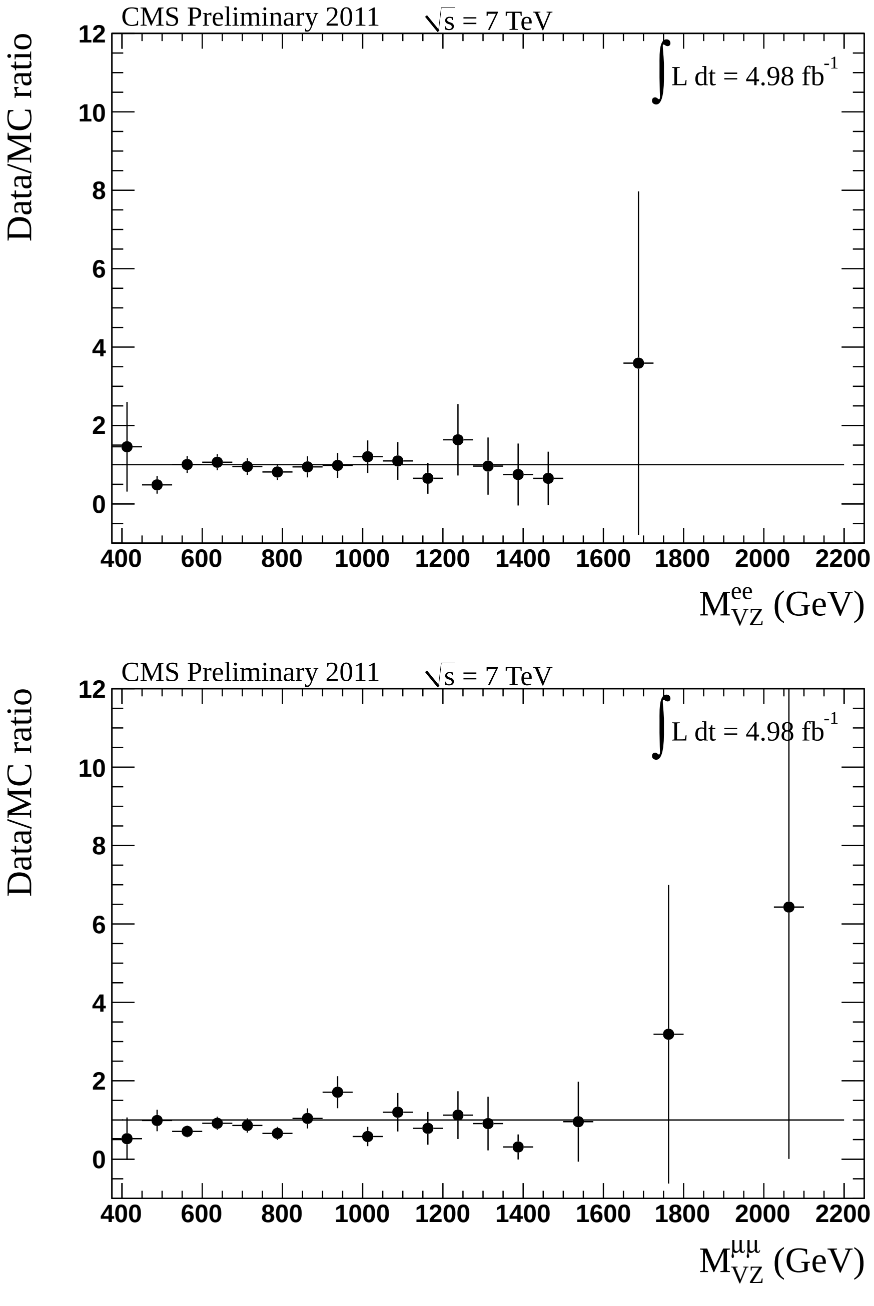

Figure 5.27: Data to expected background ratio as a function of M_{VZ} for the electron (top) and the muon (bottom) channels. The expected background is estimated with the simulated background processes. The error bars include only statistic uncertainty.

and 5.15 show the search window for each mass point with the corresponding signal efficiency and the numbers of expected background and observed events in the electron and muon channels, respectively. The combined results are reported in Table 5.16. These numbers are used as input for the calculation of the expected and observed exclusion limits on $\sigma \times \mathcal{B}$ at 95% C.L. that are also reported in the same tables.

The exclusion limits as a function of the VZ resonance mass can be seen in Fig. 5.28, where a linear interpolation is used between the benchmark mass values. These limits can be interpreted in the theoretical framework of the W' and RS graviton models. We exclude SSM W' bosons with masses between 700 and 938 (889) GeV in the SSM at NNLO (LO) at 95% C.L. This result is comparable to the limit obtained in the same model for the tri-lepton analysis ($M_{W'} > 1143$ GeV [87]). The exclusion limit calculated in the RS graviton model is for masses (m_G) between 750 and 933 (845) GeV for $k/\overline{M}_{Pl}$ = 0.05 at NLO (LO). Assuming the resonance width is much smaller than the experimental resolution for the range of $k/\overline{M}_{Pl}$ considered here, the limit can be extended in the $m_G \times k/\overline{M}_{Pl}$ plane. This is done by using a quadratic dependence of the cross section on $k/\overline{M}_{Pl}$, and by assuming that the signal efficiency remains the same. The result is shown in Fig. 5.29.

These results are not as competitive as the ones derived in the $\gamma\gamma$ and $\ell^+\ell^-$ channel searches ($m_G > 1500$ GeV) [56]. However, one should consider that those are derived assuming the usual RS model with similar branching fractions for final states containing fermion, photon, and V pairs. In more recent studies [57], RS models with SM fields propagating in the extra dimension have been proposed, in which case the RS graviton coupling to light fermions is strongly suppressed. This opens the possibility to an enhancement of the branching fractions for final states with V pairs, as well as the interest to study large values of $k/\overline{M}_{Pl}$ [57]. In this scenario, the current results provide important constraints that are complementary to the ones from the search of resonances decaying to boosted top pairs [88]. The results derived in this analysis are currently the most stringent in the V pair channel.

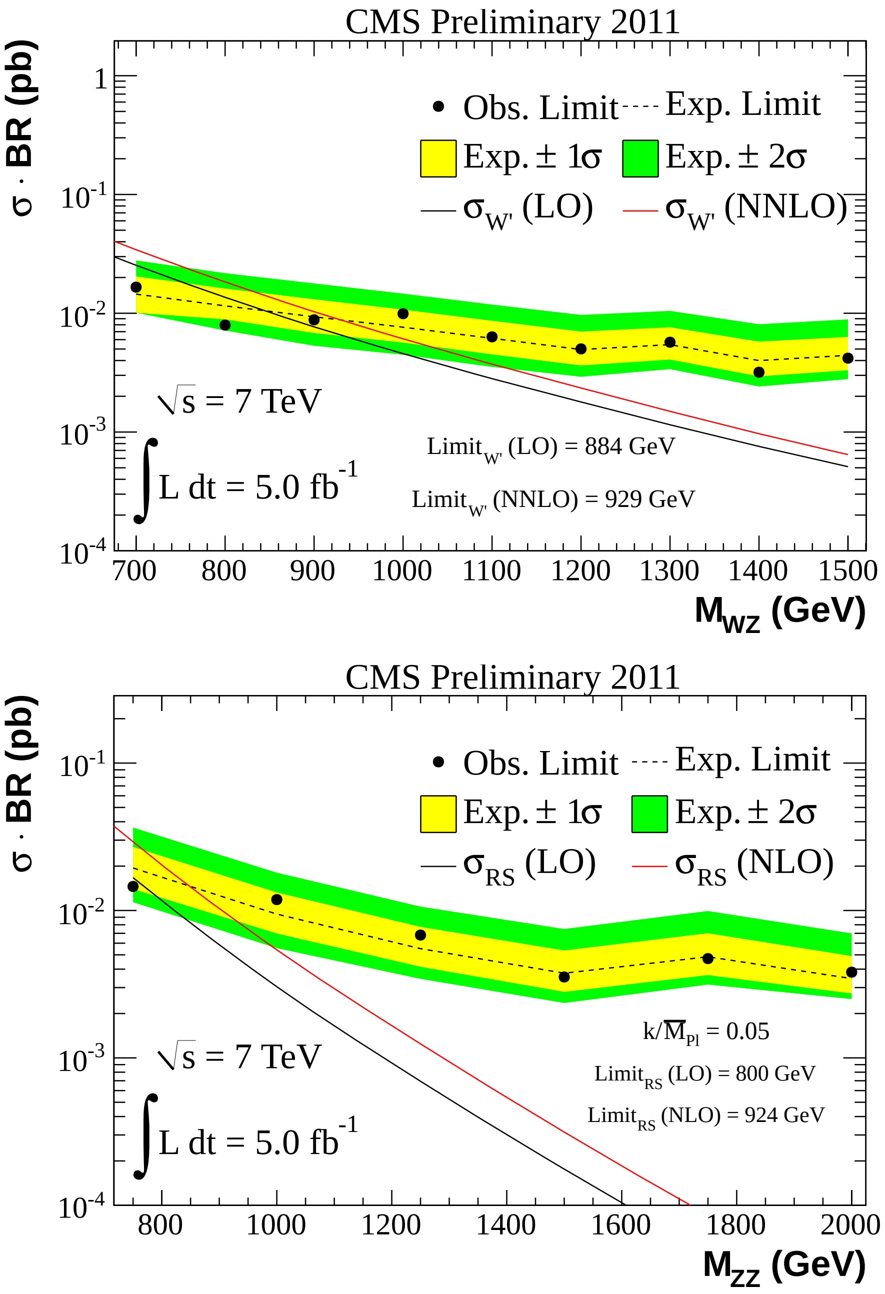

Figure 5.28: Observed and expected 95% C.L exclusion limits for a counting experiment and comparison with the theoretical predictions in W' (top) and RS Graviton (bottom) models for the combination of electron and muon channels. The limits are calculated with the frequentist CLs statistical method.

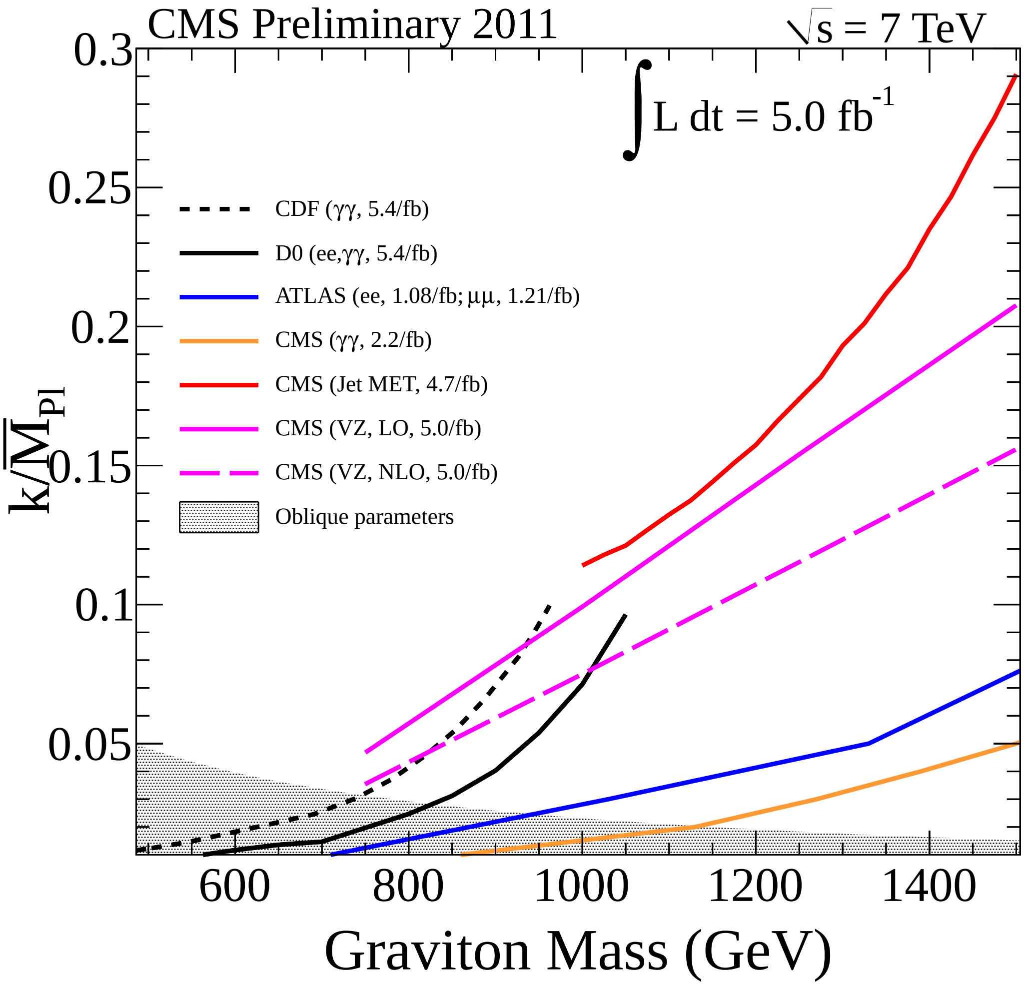

Figure 5.29: Observed and expected 95% C.L. exclusion limits for a counting experiment and comparison with the theoretical predictions in RS Graviton models for the combination of electron and muon channels. The limits are calculated with the frequentist CLs statistical method. The resonance of the hypothetical particle is considered narrow with respect to the experimental resolution.

Table 5.14: Electron channel: Search window for each mass point with the corresponding signal efficiency and the numbers of expected background ("N_{bgd}") and observed ("N_{obs}") events. These numbers are used as input for the calculation of the expected and observed exclusion limits on $\sigma(VZ) \times \mathcal{B}(V \rightarrow qq, Z \rightarrow ee)$ at 95% C.L. which are reported in the last two columns.

Mass point	Window	N_{bgd}	N_{obs}	ϵ_{sig} (%)	Obs. Limit (pb)	Exp. Limit (pb)
W' model						
700	640-760	39.7 ± 3.9	43	37.2	0.0100	0.0085
800	755-845	24.6 ± 5.7	23	35.8	0.0074	0.0079
900	855-945	17.1 ± 4.2	12	39.7	0.0040	0.0054
1000	930-1070	17.1 ± 3.5	17	48.8	0.0046	0.0046
1100	1020-1180	12.0 ± 3.0	13	47.8	0.0045	0.0041
1200	1130-1270	6.3 ± 1.9	5	40.5	0.0030	0.0034
1300	1220-1380	4.4 ± 2.8	6	31.5	0.0056	0.0046
1400	1320-1480	2.7 ± 1.8	2	23.3	0.0040	0.0043
1500	1390-1610	2.5 ± 2.2	2	19.4	0.0050	0.0051
RS model						
750	690-810	37.1 ± 6.0	32	27.2	0.0098	0.0119
1000	940-1060	14.6 ± 3.1	16	35.3	0.0068	0.0060
1250	1180-1320	4.9 ± 1.9	7	35.4	0.0051	0.0039
1500	1390-1610	2.5 ± 2.0	2	27.3	0.0036	0.0036
1750	1540-1960	2.0 ± 1.7	1	15.9	0.0048	0.0055
2000	1760-2240	1.3 ± 1.6	0	16.7	0.0026	0.0022

Table 5.15: Muon channel: Search window for each mass point with the corresponding signal efficiency and the numbers of expected background ("N_{bgd}") and observed ("N_{obs}") events. These numbers are used as input for the calculation of the expected and observed exclusion limits on $\sigma(VZ) \times \mathcal{B}(V \to qq, Z \to \mu\mu)$ at 95% C.L. which are reported in the last two columns.

Mass point	Window	N_{bgd}	N_{obs}	ϵ_{sig} (%)	Obs. Limit (pb)	Exp. Limit (pb)
W' model						
700	640-760	48.7 ± 8.9	45	39.9	0.0092	0.0102
800	755-845	28.6 ± 6.9	21	39.8	0.0057	0.0077
900	855-945	19.2 ± 4.3	23	41.3	0.0084	0.0067
1000	930-1070	18.7 ± 3.7	26	50.5	0.0077	0.0051
1100	1020-1180	12.9 ± 3.1	12	51.8	0.0038	0.0040
1200	1130-1270	6.7 ± 2.2	8	43.7	0.0041	0.0035
1300	1220-1380	4.6 ± 2.1	4	42.0	0.0029	0.0030
1400	1320-1480	2.9 ± 2.0	1	38.9	0.0019	0.0024
1500	1390-1610	2.6 ± 1.7	2	39.7	0.0024	0.0025
RS model						
750	690-810	44.1 ± 9.2	34	29.9	0.0091	0.0124
1000	940-1060	15.9 ± 3.4	20	38.2	0.0080	0.0061
1250	1180-1320	5.2 ± 2.1	6	40.5	0.0039	0.0034
1500	1390-1610	2.6 ± 1.6	2	43.5	0.0022	0.0023
1750	1540-1960	2.1 ± 1.4	2	32.2	0.0030	0.0029
2000	1760-2240	1.3 ± 1.9	2	42.2	0.0026	0.0022

Table 5.16: Combined channels: Expected and observed exclusion limits on $\sigma(VZ) \times \mathcal{B}(V \to qq, Z \to \ell\ell, \ell = e, \mu)$ at 95% C.L. for the electron and muon channels combined for each mass point and search window.

Mass point	Window	Obs. Limit (pb)	Exp. Limit (pb)
W' model			
700	640-760	0.0166	0.0145
800	755-845	0.0079	0.0115
900	855-945	0.0088	0.0093
1000	930-1070	0.0099	0.0076
1100	1020-1180	0.0063	0.0062
1200	1130-1270	0.0050	0.0050
1300	1220-1380	0.0057	0.0054
1400	1320-1480	0.0032	0.0040
1500	1390-1610	0.0042	0.0044
RS model			
750	690-810	0.0146	0.0194
1000	940-1060	0.0119	0.0095
1250	1180-1320	0.0068	0.0055
1500	1390-1610	0.0035	0.0038
1750	1540-1960	0.0047	0.0049
2000	1760-2240	0.0038	0.0035

Chapter 6

Conclusions

The beginning of the Large Hadron Collider operations in 2010 started a new era in high energy physics. The data collected by the experiments in the last couple of years provided further means to test the Standard Model as the theory which explains the particle and its interactions up to the 1 TeV scale.

The CMS experiment is having an outstanding performance so far. It includes new results and measurements in a broad spectra of analysis aiming to probe the Standard Model: precise measurements in b-physics, including the inclusive b-jet production cross section, and a comparison of various b-hadron production rates; the search for the rare $B_{s/d} \to \mu\mu$ decays, setting limits on its branching fraction; the total inelastic pp cross section at 7 and 8 TeV; precision tests of QCD and electroweak theory; measurement of associated production of Z boson with one or two b-jets, as well as angular correlations between the b-hadrons produced in association with a Z boson; the W charge asymmetry measurement in the $W \to e\nu$ channel; W production cross section in the $W \to \tau\nu$ channel; Drell–Yan cross section; studies of dijets produced in association with a W boson where the CDF experiment saw a peak structure with dijet mass $\sim$ 150 GeV/c^2, not confirming the CDF result; precision measurements of the top production cross section and properties, including the most precise measurement of the top mass in the dilepton channel as well as in the lepton+jets channel; differential measurement of the top quark-antiquark forward-backward asymmetry; and many other interesting results.

The primary focus, however, has been on the search for the Higgs boson. Besides significant strides in limiting the allowed mass region for the minimal SM Higgs, it was announced on July 4th 2012 the discovery of a previously unknown boson of mass $\sim$ 125 GeV/c^2, whose behavior so far has been consistent with the Higgs boson. The discovery was made combining the $H \to \gamma\gamma$ channel (with 4.0σ local significance), the $H \to ZZ \to 4\ell$ channel (3.2σ local significance) and $H \to WW \to \ell\nu\ell\nu$ (1.6σ local significance), adding up to 5.0σ combined local significance.

Further studies are being performed with the remaining 2012 datasets, and by the end of the year, before the first long shut down planned for 2013, approximately 25–30 fb^{-1} of 7 plus 8 TeV data will be collected and used to determine the properties of the new boson. This will help to enlighten some current questions, such as the lack of an excess in the $H \to \tau\tau$ channel, the $H \to \gamma\gamma$ rate and the branching fractions in all the sensitive channels, and its compatibility to the SM Higgs boson.

Besides the exciting discovery of the new Higgs–like boson, the searches for physics beyond the Standard Model are producing several new results. The SUSY searches in CMS are shifting their focus from light gluino pair production to more complicated SUSY scenarios, such as light third generation, compressed mass spectrum scenarios, and chargino–neutralino production. The SUSY group produced a number of limits in the CMSSM plane, constraining the parameter space for supersymmetric models. Exotic particles searches include pair–produced dark matter, new vector bosons (Z', W'), extra dimensions (ADD, RS), black–holes, heavy neutrinos, right handed W, fourth generation, leptoquarks, compositeness, to name a few.

The main reason to search for VV resonances at high masses has been historically connected to electroweak symmetry breaking models. However, the discovery of a SM Higgs boson at $M_H = 125$ GeV/c^2 does not exclude all the models being considered — it is possible to accommodate this resonance within the theoretical framework.

In this thesis, a search for new exotic particles decaying to the VZ final state was performed, where V is either a W or a Z decaying hadronically and the Z decays to a pair of electrons or muons. The analysis uses a data sample of proton–proton collisions corresponding to an integrated luminosity of 5 fb^{-1} collected by the Compact Muon Solenoid experiment at the Large Hadron Collider at a center–of–mass energy of 7 TeV in 2011. No significant excess was observed in the mass distribution of the VZ candidates compared to the background expectation from Standard Model processes. Lower bounds at the 95% confidence level were set on the mass of hypothetical particles decaying to the VZ final state in two theoretical models. In the Randall–Sundrum model, graviton resonances with masses between 700 and 924 GeV/c^2 for $k/\overline{M}_{Pl}$ =0.05 were excluded. We also investigated the possible existence of heavy charged vector bosons, as the ones predicted by the Sequential Standard Model, and arrived to the conclusion that the W' bosons were excluded in the mass interval between 700 and 929 GeV/c^2.

Appendix A

Detailed calculation of invariant amplitudes

A.1 Fermions

The Feynman rule for fermions is given by Fig. A.1 and Eq. A.1.

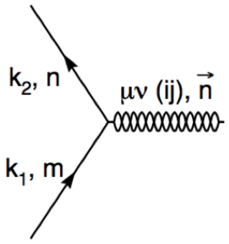

Figure A.1: Vertice for the graviton coupling to a fermion pair.

$$h_{\mu\nu}\bar{\psi}\psi : \quad \frac{-i\kappa}{8}\left[\gamma^{\mu}(k_1^{\nu}+k_2^{\nu})+\gamma_{\nu}(k_1^{\mu}+k_2^{\mu})-2\eta_{\mu\nu}(k_1+k_2-2m)\right] \tag{A.1}$$

For the decay $G_{KK}(q) \to \psi(k_1) + \bar{\psi}(k_2)$, the invariant amplitude is written as:

$$\begin{aligned} \mathcal{M} = & \left(\frac{-i\kappa}{8}\right)\epsilon_{\mu\nu}(q)\ . \\ & .\ \bar{u}(k_1)\left[\gamma^{\mu}(k_1^{\nu}-k_2^{\nu})+\gamma^{\nu}(k_1^{\mu}-k_2^{\mu})-2\eta^{\mu\nu}(k_1-k_2-2m)\right]v(k_2) \end{aligned}$$

Because $\epsilon_{\mu}{}^{\mu}(q) = 0$, the last term is null. Thus,

$$\mathcal{M} = \left(\frac{-i\kappa}{8}\right)\epsilon_{\mu\nu}(q)\bar{u}(k_1)\left[\gamma^{\mu}(k_1-k_2)^{\nu}+\gamma^{\nu}(k_1-k_2)^{\mu})\right]v(k_2)$$

Defining $K \equiv k_1 - k_2$, the amplitude can be rewritten as:

$$\mathcal{M} = \left(\frac{-i\kappa}{8}\right) \epsilon_{\mu\nu}(q)\bar{u}(k_1) \left(\gamma^\mu K^\nu + \gamma^\nu K^\mu\right) v(k_2)$$

And then, finally:

$$\begin{aligned} |\mathcal{M}|^2 = &\left(\frac{\kappa}{8}\right)^2 \frac{1}{5} \sum_{pol} \epsilon^\dagger_{\mu\nu}(q)\epsilon_{\alpha\beta}(q) \\ &\times \mathrm{Tr}\left[\left(\not{k}_2 + m\right)\left(\gamma^\mu K^\nu + \gamma^\nu K^\mu\right)\left(\not{k}_1 - m\right)\left(\gamma^\alpha K^\beta + \gamma^\beta K^\alpha\right)\right] \end{aligned}$$

Using the sum over all the states of the massive graviton to define $B^{\mu\nu,\alpha\beta}$ as,

$$\sum_{pol} \epsilon^\dagger_{\mu\nu}(q)\epsilon_{\alpha\beta}(q) \equiv B^{\mu\nu,\alpha\beta} = \left(Q^{\mu\alpha}Q^{\nu\beta} + Q^{\mu\beta}Q^{\nu\alpha} - \frac{2}{3}Q^{\mu\nu}Q^{\alpha\beta}\right)$$

where,

$$Q^{\mu\nu} = -\eta^{\mu\nu} + \frac{1}{M^2}q^\mu q^\nu$$

The invariant matrix element can be written as,

$$\begin{aligned} |\mathcal{M}|^2 = &\left(\frac{\kappa}{8}\right)^2 \frac{1}{5} B^{\mu\nu,\alpha\beta} \\ &\times 4\Big\{ \left[k_2^\mu k_1^\alpha + k_2^\alpha k_1^\mu - \eta^{\mu\alpha}(k_1.k_2)\right] K^\nu K^\beta \\ &+ \left[k_2^\mu k_1^\beta + k_2^\beta k_1^\mu - \eta^{\mu\beta}(k_1.k_2)\right] K^\nu K^\alpha \\ &+ \left[k_2^\nu k_1^\alpha + k_2^\alpha k_1^\nu - \eta^{\alpha\nu}(k_1.k_2)\right] K^\mu K^\beta \\ &+ \left[k_2^\nu k_1^\beta + k_2^\beta k_1^\nu - \eta^{\nu\beta}(k_1.k_2)\right] K^\mu K^\alpha \\ &- m^2\left[\eta^{\mu\alpha}K^\nu K^\beta + \eta^{\mu\beta}K^\nu K^\alpha + \eta^{\nu\alpha}K^\mu K^\beta + \eta^{\nu\beta}K^\mu K^\alpha\right]\Big\} \end{aligned}$$

Defining

$$(X, Y, Z, T) \equiv B^{\mu\nu,\alpha\beta}X_\mu Y_\nu Z_\alpha T_\beta$$

and

$$(X, \nu, \nu, T) \equiv \eta_{\nu,\alpha}X_\mu B^{\mu\nu,\alpha\beta}T_\beta$$

one can rewrite $\mathcal{M}$ as:

$$
\begin{aligned}
|\mathcal{M}|^2 = &\left(\frac{\kappa}{8}\right)^2 \frac{4}{5} \\
&\times \left\{ \Big[(k_2, K, k_1, K) + (k_1, K, k_2, K) + (k_2, K, K, k_1) + (k_1, K, K, k_2) \right. \\
&+ (K, k_2, k_1, K) + (K, k_1, k_2, K) + (K, k_2, K, k_1) + (K, k_1, K, k_2) \Big] \\
&\left. - \Big[(k_1.k_2) + m^2 \Big] \Big[(\mu, K, \mu, K) + (\mu, K, K, \mu) + (K, \mu, \mu, K) + (K, \mu, K, \mu) \Big] \right\}
\end{aligned}
$$

Using the symmetry of $B^{\mu\nu,\alpha\beta}$,

$$
\begin{aligned}
|\mathcal{M}|^2 &= \left(\frac{\kappa}{8}\right)^2 \frac{4}{5} \times 4 \left\{ 2(K, k_1, K, k_2) - \Big[(k_1.k_2) + m^2 \Big] (K, \mu, K, \mu) \right\} \\
&= \left(\frac{\kappa}{8}\right)^2 \frac{32}{5} \times \left\{ (K, k_1, K, k_2) - \frac{M^2}{4} (K, \mu, K, \mu) \right\}
\end{aligned}
$$

But, in the other hand,

$$
(K, k_1, K, k_2) = \left[(K.Q.K)(k_1.Q.k_2) + \frac{1}{3} (K.Q.k_1)(K.Q.k_2) \right]
$$

Note that $K.q = (k_1 - k_2)(k_1 + k_2) = 0$. All the terms can then be written as:

$$
\begin{aligned}
(K.Q.K) &= -K^2 \\
(K.Q.k_1) &= -(K.k_1) = (k_1.k_2) - m^2 = -\frac{1}{2} K^2 \\
(K.Q.k_2) &= -(K.k_2) = -(k_1.k_2) + m^2 = -(K.Q.k_1) = \frac{1}{2} K^2 \\
(k_1.Q.k_2) &= -(k_1.k_2) + \frac{[(k_1.k_2) + m^2]^2}{M^2} = -\frac{M^2}{4} (1 - 4r)
\end{aligned}
$$

Where:

$$
K^2 = -M^2 (1 - 4r) \ \text{ and } \ (k_1.k_2) = \frac{M^2}{2} (1 - 2r)
$$

Thus,

$$
\begin{aligned}
(K, k_1, K, k_2) &= \left[(K.Q.K)(k_1.Q.k_2) + (K.Q.k_1)(K.Q.k_2) - \frac{2}{3} (K.Q.k_1)(K.Q.k_2) \right] \\
&= \frac{-M^4 (1 - 4r)^2}{3}
\end{aligned}
$$

Now,

$$\begin{aligned}(K,\mu,K,\mu) &= \left[-K^2(-4+1) + K^2 - \frac{2}{3}K^2\right] = \frac{10}{3}K^2 \\ &= -\frac{10}{3}M^2(1-4r)\end{aligned}$$

and,

$$\begin{aligned}|\mathcal{M}|^2 &= \left(\frac{\kappa}{8}\right)^2 \frac{32}{5} \times \left\{(K,k_1,K,k_2) - \frac{M^2}{4}(K,\mu,K,\mu)\right\} \\ &= \left(\frac{\kappa^2 M^4}{20}\right)(1-4r)[1+(8/3)r]\end{aligned}$$

Putting everything together, the expression for the decay width $\Gamma(G_{KK} \to f\bar{f})$ is given by,

$$\begin{aligned}\Gamma(G_{KK} \to f\bar{f}) &= \frac{(1-4r)^{1/2}}{16\pi M}|\mathcal{M}|^2 \\ &= \left(\frac{\kappa^2 M^3}{320\pi}\right)(1-4r)^{3/2}[1+(8/3)r]\end{aligned}$$

A.2 Bosons

The Feynman rule for vector bosons is given by Fig. A.2 and Eq. A.2.

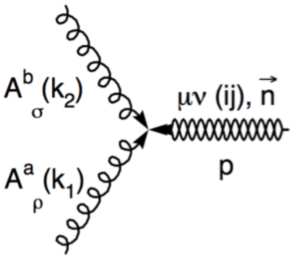

Figure A.2: Vertice for the graviton coupling to a gauge boson pair.

$$h_{\mu\nu}VV: \quad \frac{-i\kappa}{2}\left[(k_1.k_2 + m^2)C_{\mu\nu,\alpha\beta} + D_{\mu\nu,\alpha\beta}\right] \tag{A.2}$$

In the unitary gauge ($\xi \to \infty$), C and D are given by:

$$C_{\mu\nu,\alpha\beta} = \eta_{\mu\alpha}\eta_{\nu\beta} + \eta_{\mu\beta}\eta_{\nu\alpha} - \eta_{\mu\nu}\eta_{\alpha\beta}$$

and,

$$D_{\mu\nu,\alpha\beta} = \eta_{\mu\nu}k_{1\beta}k_{2\alpha} - \left[\eta_{\mu\beta}k_{1\nu}k_{2\alpha} + \eta_{\mu\alpha}k_{1\beta}k_{2\nu} - \eta_{\alpha\beta}k_{1\mu}k_{2\nu} + (\mu \leftrightarrow \nu)\right]$$

For the decay $G_{KK}(q, \epsilon^{\mu\nu}) \longrightarrow V(k_1, \epsilon^{\alpha}) + V(k_2, \epsilon^{\beta})$, the invariant amplitude is written as:

$$\mathcal{M} = \frac{-i\kappa}{2}\left[\frac{M^2}{2}C_{\mu\nu,\alpha\beta} + D_{\mu\nu,\alpha\beta}\right]\epsilon^{\mu\nu}(q)\epsilon^{\alpha}(k_1)\epsilon^{\beta}(k_2)$$

Taking into account the polarization transversality,

$$C_{\mu\nu,\alpha\beta} = \eta_{\mu\alpha}\eta_{\nu\beta} + \eta_{\mu\beta}\eta_{\nu\alpha}$$

and

$$D_{\mu\nu,\alpha\beta} = -\left[\eta_{\mu\beta}k_{1\nu}k_{2\alpha} + \eta_{\mu\alpha}k_{1\beta}k_{2\nu} - \eta_{\alpha\beta}k_{1\mu}k_{2\nu} + (\mu \leftrightarrow \nu)\right]$$

Therefore,

$$\begin{aligned}
|\mathcal{M}|^2 &= \frac{1}{5}\left(\frac{\kappa}{2}\right)^2\left[\frac{M^2}{2}C_{\mu\nu,\alpha\beta} + D_{\mu\nu,\alpha\beta}\right]\left[\frac{M^2}{2}C_{\rho\sigma,\delta\lambda} + D_{\rho\sigma,\delta\lambda}\right] \\
&\times \sum_{pol}\epsilon^{\dagger\mu\nu}(q)\epsilon^{\rho\sigma}(q)\sum_{pol}\epsilon^{\dagger\alpha}(k_1)\epsilon^{\delta}(k_1)\sum_{pol}\epsilon^{\dagger\beta}(k_2)\epsilon^{\lambda}(k_2) \\
&= \frac{1}{5}\left(\frac{\kappa}{2}\right)^2\left[\frac{M^2}{2}C_{\mu\nu,\alpha\beta} + D_{\mu\nu,\alpha\beta}\right]\left[\frac{M^2}{2}C_{\rho\sigma,\delta\lambda} + D_{\rho\sigma,\delta\lambda}\right] \\
&\times B^{\mu\nu,\rho\sigma}(q)(K_1^{\alpha\delta})(K_2^{\beta\lambda})
\end{aligned}$$

Defining:

$$K_i^{\mu\nu} = -\eta^{\mu\nu} + \frac{1}{M^2}k_i^{\mu}k_i^{\nu}$$

we have

$$\begin{aligned}
|\mathcal{M}|^2 = \frac{1}{5}\left(\frac{\kappa}{2}\right)^2 \Bigg\{ & \frac{M^4}{4}C_{\mu\nu,\alpha\beta}C_{\rho\sigma,\delta\lambda}B^{\mu\nu,\rho\sigma}K_1^{\alpha\delta}K_2^{\beta\lambda} + \frac{M^2}{2}C_{\mu\nu,\alpha\beta}D_{\rho\sigma,\delta\lambda}B^{\mu\nu,\rho\sigma}K_1^{\alpha\delta}K_2^{\beta\lambda} \\
& + \frac{M^2}{2}D_{\mu\nu,\alpha\beta}C_{\rho\sigma,\delta\lambda}B^{\mu\nu,\rho\sigma}K_1^{\alpha\delta}K_2^{\beta\lambda} + D_{\mu\nu,\alpha\beta}D_{\rho\sigma,\delta\lambda}B^{\mu\nu,\rho\sigma}K_1^{\alpha\delta}K_2^{\beta\lambda}\Bigg\}
\end{aligned}$$

For a massless vector boson, the invariant amplitude becomes,

$$|\mathcal{M}|^2 = \frac{1}{5}\left(\frac{\kappa}{2}\right)^2 \left\{ \frac{M^4}{4} C_{\mu\nu,\alpha\beta} C_{\rho\sigma,\alpha\beta} B^{\mu\nu,\rho\sigma} + \frac{M^2}{2} C_{\mu\nu,\alpha\beta} D_{\rho\sigma,\alpha\beta} B^{\mu\nu,\rho\sigma} \right.$$
$$\left. + \frac{M^2}{2} D_{\mu\nu,\alpha\beta} C_{\rho\sigma,\alpha\beta} B^{\mu\nu,\rho\sigma} + D_{\mu\nu,\alpha\beta} D_{\rho\sigma,\alpha\beta} B^{\mu\nu,\rho\sigma} \right\}$$

Defining

$$(k_1.k_2) = (q.k_1) = (q.k_2) = \frac{M^2}{2} \equiv x$$

we notice that,

$$Q^{\mu\nu} k_{1\nu} = -\frac{1}{2} K^\mu \text{ and } Q^{\mu\nu} k_{2\nu} = \frac{1}{2} K^\mu$$

with $K \equiv k_1 - k_2$, and,

$$C_{\mu\nu,\alpha\beta} B^{\mu\nu,\rho\sigma} = \left(Q^{\alpha\rho} Q^{\beta\sigma} + Q^{\alpha\sigma} Q^{\beta\rho} - \frac{2}{3} Q^{\alpha\beta} Q^{\rho\sigma} + Q^{\beta\rho} Q^{\alpha\sigma} + Q^{\beta\sigma} Q^{\alpha\rho} - \frac{2}{3} Q^{\beta\alpha} Q^{\rho\sigma} \right)$$

and

$$C_{\mu\nu,\alpha\beta} C_{\rho\sigma,\alpha\beta} B^{\mu\nu,\rho\sigma} = \left(Q^{\alpha\alpha} Q^{\beta\beta} + Q^{\alpha\beta} Q^{\beta\alpha} - \frac{2}{3} Q^{\alpha\beta} Q^{\alpha\beta} + Q^{\beta\alpha} Q^{\alpha\beta} \right.$$
$$+ Q^{\beta\beta} Q^{\alpha\alpha} - \frac{2}{3} Q^{\beta\alpha} Q^{\alpha\beta} + Q^{\alpha\beta} Q^{\beta\alpha} + Q^{\alpha\alpha} Q^{\beta\beta}$$
$$\left. - \frac{2}{3} Q^{\alpha\beta} Q^{\beta\alpha} + Q^{\beta\beta} Q^{\alpha\alpha} + Q^{\beta\alpha} Q^{\alpha\beta} - \frac{2}{3} Q^{\beta\alpha} Q^{\beta\alpha} \right)$$

Since $Q^{\mu\mu} = -3$ and

$$Q^{\mu\nu} Q^{\nu\mu} = (-\eta^{\mu\nu} + \frac{1}{M^2} q^\mu q^\nu)(-\eta^{\nu\mu} + \frac{1}{M^2} q^\nu q^\mu) = 3$$

we have,

$$C_{\mu\nu,\alpha\beta} C_{\rho\sigma,\alpha\beta} B^{\mu\nu,\rho\sigma} = 40$$

And the tensor products become,

$$C_{\mu\nu,\alpha\beta} D_{\rho\sigma,\alpha\beta} = -\{ \eta_{\rho\nu} k_{1\sigma} k_{2\mu} + \eta_{\rho\mu} k_{1\nu} k_{2\sigma} - \eta_{\mu\nu} k_{1\rho} k_{2\sigma} + (\rho \leftrightarrow \sigma)$$
$$+ \eta_{\rho\mu} k_{1\sigma} k_{2\nu} + \eta_{\rho\nu} k_{1\mu} k_{2\sigma} - \eta_{\nu\mu} k_{1\rho} k_{2\sigma} + (\rho \leftrightarrow \sigma) \Big\}$$

and,

$$\begin{aligned}
&C_{\mu\nu,\alpha\beta}D_{\rho\sigma,\alpha\beta}B^{\mu\nu,\rho\sigma} = \\
&= -\Big\{ k_{2\mu}Q^{\mu\nu}k_{1\sigma}Q^{\nu\sigma} + k_{2\mu}Q^{\mu\sigma}k_{1\sigma}Q^{\nu\nu} - \frac{2}{3}k_{2\mu}Q^{\mu\nu}k_{1\sigma}Q^{\nu\sigma} + \\
&+ Q^{\mu\mu}k_{1\nu}k_{2\sigma}Q^{\nu\sigma} + k_{2\sigma}Q^{\mu\sigma}k_{1\nu}Q^{\nu\mu} - \frac{2}{3}k_{1\nu}Q^{\mu\nu}k_{2\sigma}Q^{\mu\sigma} \\
&- k_{1\rho}Q^{\mu\rho}k_{2\sigma}Q^{\mu\sigma} - k_{2\sigma}Q^{\mu\sigma}k_{1\rho}Q^{\mu\rho} + \frac{2}{3}Q^{\mu\mu}k_{1\rho}Q^{\rho\sigma}k_{2\sigma} \\
&+ Q^{\mu\mu}k_{1\sigma}Q^{\nu\sigma}k_{2\nu} + k_{1\sigma}Q^{\mu\sigma}k_{2\nu}Q^{\nu\mu} - \frac{2}{3}k_{2\nu}Q^{\mu\nu}k_{1\sigma}Q^{\mu\sigma} \\
&+ k_{1\mu}Q^{\mu\nu}k_{2\sigma}Q^{\nu\sigma} + k_{1\mu}Q^{\mu\sigma}k_{2\sigma}Q^{\nu\nu} - \frac{2}{3}k_{1\mu}Q^{\mu\nu}Q^{\nu\sigma}k_{2\sigma} \\
&- k_{1\rho}Q^{\mu\rho}k_{2\sigma}Q^{\mu\sigma} - k_{2\sigma}Q^{\mu\sigma}k_{1\rho}Q^{\mu\rho} + \frac{2}{3}Q^{\mu\mu}k_{1\rho}k_{2\sigma}Q^{\rho\sigma} \\
&+ (\rho \leftrightarrow \sigma)\Big\}
\end{aligned}$$

And, after some algebra,

$$C_{\mu\nu,\alpha\beta}D_{\rho\sigma,\alpha\beta}B^{\mu\nu,\rho\sigma} = -\frac{40}{3}x$$

Since,

$$\begin{aligned}
D_{\mu\nu,\alpha\beta}D_{\rho\sigma,\alpha\beta} = \Big\{ &\eta_{\rho\mu}k_{1\sigma}k_2^2k_{1\nu} + k_{1\mu}k_{1\nu}k_{2\sigma}k_{2\rho} - k_{2\mu}k_{1\nu}k_{2\sigma}k_{1\rho} \\
&+ k_{2\mu}k_{2\nu}k_{1\sigma}k_{1\rho} + \eta_{\rho\mu}k_{2\nu}k_1^2k_{2\sigma} - k_{1\mu}k_{2\nu}k_{2\sigma}k_{1\rho} \\
&- k_{1\mu}k_{2\nu}k_{1\sigma}k_{2\rho} - k_{1\mu}k_{2\nu}k_{2\sigma}k_{1\rho} + 4k_{1\mu}k_{2\nu}k_{2\sigma}k_{1\rho} + (\mu \leftrightarrow \nu) + (\rho \leftrightarrow \sigma)\Big\}
\end{aligned}$$

we have

$$D_{\mu\nu,\alpha\beta}D_{\rho\sigma,\alpha\beta}B^{\mu\nu,\rho\sigma} = \frac{8}{3}x^2$$

The invariant amplitude becomes,

$$|\mathcal{M}|^2 = \frac{\kappa^2 M^4}{5}$$

Thus,

$$\Gamma(G \to \gamma\gamma) = \frac{S}{16\pi M}|\mathcal{M}|^2 = \frac{\kappa^2 M^3}{160\pi}$$

Because there are two identical particles in the final state, $S = 1/2$.

Appendix B

Sequential Standard Model Vector Bosons

The simple reference model represented by Sequential Standard Model for new massive vector bosons proposed in Ref. [58] is obtained by taking for the heavy $V^{\pm}$ and V^0 the same couplings as for the ordinary $W^{\pm}$ and Z in the standard model. This refers to couplings to fermions ($Vq\bar{q}$ and $V\ell\bar{\ell}$) and the vertices $V^0W^+W^-$ or $V^{\pm}W^{\mp}Z$. This assumption gives rise to both large couplings to fermions (high production cross-sections) and large branching ratios into WW or WZ, leading to production rates for the lepton(s) plus two-jets modes which are larger than in extended gauge models or in natural models with a strongly interacting Higgs sector.

Within the reference model, the three-vector boson vertex V_{abc} is given by,

$$V_{W^-W^+V^0} = V_{W^{\mp}V^{\pm}Z} = ie\ \mathrm{cotg}\theta_W \left[g_{\mu\nu}(q-p)_\lambda + g_{\mu\lambda}(p-r)_\nu + g_{\nu\lambda}(r-q)_\mu\right] \ ,$$

where all momenta are incoming, the momentum index pairs (p,μ), (q,ν) and (r,λ) correspond to the vector bosons of charges 0, + and -, respectively, e is the electron charge ($\alpha = e^2/4\pi = 1/128$, valid at $Q^2 = M_W^2$) and θ_W is the weak angle. The decay widths into WW or WZ are given in this model by:

$$\begin{aligned}\Gamma(V^{\pm} \to ZW^{\pm}) = \frac{\alpha}{48}\ \mathrm{cotg}\theta_W\ M_{V^{\pm}} \frac{M_{V^{\pm}}^4}{M_Z^2 M_W^2} \cdot \left[\left(1 - \frac{M_Z^2 - M_W^2}{M_{V^{\pm}}^2}\right) - 4\frac{M_W^2}{M_{V^{\pm}}^2}\right] \\ \left[1 + 10\left(\frac{M_W^2 + M_Z^2}{M_{V^{\pm}}^2}\right) + \frac{M_W^4 + M_Z^4 + 10 M_W^2 M_Z^2}{M_{V^{\pm}}^4}\right]\end{aligned} \tag{B.1}$$

and,

$$\Gamma(V^{\pm} \to W^{+}W^{-}) = \frac{\alpha}{48}\,\mathrm{cotg}\theta_W\, M_{V^0}\left(\frac{M_{V^0}}{M_W}\right)^4\left(1-4\frac{M_W^2}{M_{V^0}^2}\right)^{3/2} \cdot \left[1+20\left(\frac{M_W}{M_{V^0}}\right)^2+12\left(\frac{M_W}{M_{V^0}}\right)^4\right]. \tag{B.2}$$

The characteristic feature of the reference model is the increase of the WW or WZ widths as M_V^5, which produces rapidly increasing branching ratios into WW or WZ modes when $M_V$is increased above $2M_{W,Z}$. Since the couplings $V_{V^{\pm}f\bar{f}'}$ and $V_{V^0 f\bar{f}}$ are taken as in the standard model,the corresponding widths are given by:

$$\Gamma(V^{\pm} \to f\bar{f}') = \frac{\alpha}{12}N_C\frac{M_{V^{\pm}}}{\sin^2\theta_W} \tag{B.3}$$

$$\Gamma(V^0 \to f\bar{f}) = \frac{\alpha}{12}N_C\frac{M_{V^0}}{\sin^2\theta_W\cos^2\theta_W}\cdot\left[1+\left(1-4|Q_f|\sin^2\theta_W\right)^2\right] \tag{B.4}$$

where $N_C = 1$ for leptons, $N_C = 3$ for quarks, and Q_f is the fermion electric charge. Further calculations can be found elsewhere [58].

In summary, the reference model has as the main features the large coupling to the fermions and large branching ratios into WW or WZ. If the second assumption is relaxed while the first is kept, the rates for $\ell\bar{\ell}jj$, important for large V masses, are lost. This loss is compensated to a large extend by the corresponding increase in the branching ratios $B(V \to \ell\bar{\ell})$ into the purely leptonic modes. Thus, provided that the coupling to fermions remain of the same order as for the ordinary W and Z, the discovery range of the LHC extends to large V masses.

Appendix C

LO vs NLO comparisons for $V + jets$: MC as a tool for background determination for NP searches at LHC

This work was performed in 2010, with University College London researchers Prof. Emily Nurse and Dr. Gavin Hesketh. Although it is not directly related to the thesis analysis, the techniques studied are closely related to Monte Carlo generation, fundamental not only for the thesis work but also for any other high energy physics data analysis. This work was developed before the start of the LHC at $\sqrt{s} = 7$ TeV, and the LHC prospects used an integrated luminosity of 1 fb^{-}1, dataset equivalent to the statistics available in July 2011.

C.1 Introduction

The leptonic decays of the heavy gauge bosons W and/or Z accompanied by jets, $W \rightarrow \ell\nu +$ jets and $Z \rightarrow \ell\ell +$ jets, offer search channels for new interactions of particles in high energy collisions. Many extensions of the Standard Model predict new particles with electroweak (EWK) couplings that decay into the SM gauge bosons W, Z, and γ, accompanied by jets. Searches have been made in the W or $Z +$ jets channels for supersymmetric particles such as stop and sbottom, technicolored hadrons, or heavy W' and Z' bosons that might arise in extended gauge groups or from excitations in extra spatial dimensions and charged Higgs bosons among others. Any production of new heavy particles with quantum numbers conserved by the strong interaction and EWK couplings is likely to contribute to signatures with one or more EWK gauge bosons; additional jets will always be present at some level from initial-state radiation, and may also be products of cascade decays of new heavy particles. $W + N$ jets and $t\bar{t} +$ jets are backgrounds to most supersymmetry searches in final states with leptons, jets and missing transverse energy. The $Z(\rightarrow \nu\bar{\nu}) +$ jets is an irreducible background to inclusive hadronic searches of Dark Matter, based on jets and missing energy (MET).

In the context of the SM, the study of the production of electroweak bosons with N jets allows for tests of perturbative QCD. The production cross section scales approximately with the strong coupling constant for each additional jet. While current theoretical predictions at leading order (LO) and next to leading order (NLO) are in good agreement with data at the Tevatron, comparison at the higher energy of the LHC, and at higher jet multiplicities are needed. Inclusive and differential cross sections access the parameters of the perturbative expansion, such as the renormalization and the factorization scales, as well as the parton density functions (`PDFs`), through the p_T and η distributions of the vector bosons and the associated jets. Predicting all these quantities and comparing them to the Tevatron data has already produced several improvements in the calculation and generation techniques, such as the introduction of generators based on the LO calculations of matrix-element (ME) for the associated jet production, and the definition of several matching procedures to the parton-shower generators.

In this paper we make a comparative study of ME+PS Monte Carlo generators (`SHERPA` and `HERWIG` $++$) with an available NLO calculations as applicable (`POWHEG`), validated with Tevatron D0 and CDF data, and generated at the LHC energy. This will serve as preparatory MC study of the major SM backgrounds for the regions that are relevant to New Physics searches.

C.2 Matrix Elements Corrections / Parton Shower

The Parton Shower (PS) technique is a collinear approximation of the description of parton splittings in QCD radiation that accompanies hard scattering processes. However, although it provides a good description of low $p_\perp$ observables, it usually fails to fill the phase space of hard radiation. One way to improve the description of kinematical observables is to add a Matrix Element (ME) correction for the extra emissions. This can be implemented in different ways, as will be described in each generator session.

C.2.1 `SHERPA`

The `SHERPA` generator uses the improved CKKW Matrix Element - Parton Shower merging [89] that relies on a separation of the event phase space in two separated regions, defined by a choice of scale. Above the chosen scale, all radiation must be produced by the Matrix Elements, and below the chosen scale all radiation produced by the Parton Shower. In matching these two regions to provide full phase space coverage, overlaps such as a parton shower emission in the scale range covered by the Matrix Element, must be removed [90].

The basic steps in the algorithm implementation are [90]:

- Events are generated based on the matrix elements for W/Z + k jets, where k = 1, ... N. The Matrix Element jets are required to be above the merging scale, Q_{cut}.
- Events are then passed to the parton shower, which is allowed to generate radiation from any part of the process (including between two ME emissions).
- The event is then reconstructed back from the final state particles. Particles are combined in the most likely combinations according to the parton shower probabilities.
- The reconstructed shower is then analyzed, and any events which contain splittings above the scale Q_cut are vetoed (called a "truncated shower")

The `SHERPA` generator automatizes the generation of inclusive samples, combining ME for different parton multiplicities with PS and hadronization. Some parameters related to the ME and PS calculations have to be set accordingly.

C.2.2 `HERWIG`$++$

The aim of the ME corrections in the PS on `HERWIG`$++$ is to correct for two deficiencies in the shower algorithm: to populate the uncovered region of high $p_\perp$ in the phase space (non-soft non-collinear), and to correct the populated region, where the extrapolation away from the soft and collinear limits is not perfect. These corrections are called the hard and soft matrix element corrections respectively [91].

Soft Matrix Element Corrections

The soft correction is derived by comparing the probability density that the i^{th} resolvable parton is emitted into a region of the phase space in the PS approximation (quasi-collinear limit), and the exact ME calculation. A simple veto algorithm is then be applied to the parton shower to reproduce the matrix element distribution, which relies on there always being more parton shower emissions than matrix element emissions. This is ensured simply by enhancing the emission probability of the parton shower with a constant factor [91].

The correction is applied to the hardest emission so far in the shower, to ensure that the leading order expansion of the shower distribution agrees with the leading order matrix element, and that the hardest (i.e. furthest from the soft and collinear limits) emission reproduces it [92].

Hard Matrix Element Corrections

The hard ME corrections aim to populate the high $p_\perp$ region that the PS leaves uncovered. This domain of the phase space should have radiation distributed according to the exact tree level ME for this extra emission, and as the Parton Shower does not populate this region, a different approach is needed to achieve this. Prior to any showering, the algorithm checks if the required ME is available for the hard process. Then, a point is generated in the appropriate region of phase space, with a probability based on a sampling of the integrand. The differential cross section associated with this point is then calculated and multiplied by a phase space volume factor, giving the event weight. The emission is accepted if the weight is less than a uniformly distributed random number in the [0,1] interval, and the momenta of the new parton configuration is processed by the shower as normal [91].

C.3 Next to Leading Order Methods

Both `SHERPA` and `HERWIG` $++$ described above include dominant QCD effects with leading order matrix elements combined with a leading logarithmic parton shower. However, higher order calculations are required to match the precision of current data measurements. Going even one step beyond the leading order is already a complex task: the initial hard process should be implemented in NLO; and shower development would have to be improved in next to leading logarithmic accuracy in collinear and soft structure. An intermediate step has already been developed: keeping the leading logarithmic order for the shower approximation, while improving the treatment of the hard emission to NLO accuracy (NLO+PS approach). We test one such generator: `POWHEG`.

C.3.1 `POWHEG`

In the `POWHEG` (Positive Weight Hardest Emission Generator) formalism, the generation of the hardest emission is performed first, using full NLO accuracy, and using the `HERWIG` $++$ parton shower to generate subsequent radiation. The `POWHEG` cross section for the generation of the hardest event has the following properties:

- At large k_T (momentum of incoming particle) it coincides with the NLO cross section up to NNLO terms (O(α_S^2)).
- It reproduces correctly the value of infrared safe observables at the NLO. Thus, also its integral around the small k_T region has NLO accuracy.
- At small k_T it behaves as well as standard shower Monte Carlo generators.

The `POWHEG` formula can be used as an input to any parton shower program to perform all subsequent (softer) showers and hadronization. However, as k_T is used to define the matrix element scale, the parton shower must also be ordered in $p_\perp$. The shower is then initiated with an upper limit on the scale equal to the k_T of the `POWHEG` event, and fills in all radiation below that scale (a truncated shower). For the case of a virtuality or angular ordered shower, emissions at higher k_T may be produced, and must subsequently be vetoed to avoid double counting with the ME emission: a vetoed truncated shower, which is not possible with current parton shower programs like `PYTHIA` and `HERWIG`. We point out, however, that the need of vetoed truncated showers is not specific to the `POWHEG` method. It also emerges naturally when interfacing standard matrix element calculations with parton shower. At present, there is no evidence that the effect of vetoed truncated showers may have any practical importance [93].

The `POWHEG` method solves the problem of negative event weights that arise in other NLO methods, such as in `MC@NLO`. It also defines how the highest $p_\perp$ emission may be modified to include the logarithmically enhanced effects of soft wide-angle radiation. In the `POWHEG` framework, positive weight events distributed with NLO accuracy can be showered to resume further logarithmically enhanced corrections by [91]:

- Generating an event according to the `POWHEG` formula;
- Hadronizing non-radiating events directly;
- Mapping the radiative variables parametrizing the emission into the evolution scale, momentum fraction and azimuthal angle, from which the parton shower would reconstruct identical momenta;
- Evolve, using the original LO configuration, the leg emitting the extra radiation from the default initial scale, determined by the colour structure of the N-body process, down to the hardest emission scale such that the $p_\perp$ is less than that of the hardest emission, the radiation is angular-ordered and branchings do not change the flavour of the emitting parton;
- When the evolution scale reaches the hardest emission scale, insert a branching with parameters into the shower;
- From all external legs, generate $p_\perp$ vetoed showers.

This procedure allows the generation of the truncated shower with only a few changes to the normal `HERWIG` $++$ shower algorithm [91].

C.4 Standard Analyses - Comparisons to Tevatron Data

The inclusion of Matrix Elements is only one component of the simulation. In order to describe real data, the more phenomenological aspects of the generators must also be accurate: the Parton Shower (PS), and the model of Multiple Parton Interactions (`MPI`) and Underlying Event (UE). The choice of Parton Distribution Function (`PDF`) may also play a role, or at least be highly coupled to the tuning of these phenomenological models. Finally, there are some settings unique to the generators themselves, such as the choice of matching scale between the parton shower and matrix elements. So, in order to isolate the impact of using LO or NLO matrix elements, we must also constrain all the other aspects of these models.

C.4.1 Selection of Events and Kinematic Cuts

We use the most recent data from the Tevatron experiments, CDF and D0, to test the generator performance. The Tevatron is a proton anti-proton collider with a center of mass energy $\sqrt{s}$ =1.96 TeV, located at Fermilab, USA.

For each of the analyses, events are selected according to their corresponding data selection, described in their papers. But, in general, the lepton pair invariant mass is required to be between some mass range (around Z mass peak) to enhance the contribution of pure Z exchange over $\gamma*$ exchange and $Z/\gamma*$ interference terms, and pseudorapidity cuts on the (CDF or D0) detector acceptance.

The generators were configured to produce inclusive $Z/\gamma*$ particles decaying into lepton pairs (electrons or muons), with the invariant mass constraint. Also some specific parameters, like Multiple Parton Interactions (`MPI`), Parton Distribution Functions (`PDFs`) and the mean intrinsic transverse momentum of the beams (`K_PERP`) were changed, to check which values would give a better description of the physics observables studied.

The comparison plots were made using the `RIVET` framework [94], version 1.2.1. The `RIVET` project (Robust Independent Validation of Experiment and Theory) allows validation of Monte Carlo event generators. It uses computational efficient model for observable variables and provides a set of experimental standard validated analyses useful for generator sanity checks, as well as a convenient infrastructure for adding user's own analyses.

C.4.2 *Z* Transverse Momentum

The main benefit to using Z events to probe the underlying process is that the Z can be fully and unambiguously reconstructed. The Z $p_\perp$ is generated by the momentum balance against initial state radiation (ISR) and the primordial/intrinsic $p_\perp$ of the Z's parent partons in the incoming hadrons. Within an event generator, this recoil may be generated by a hard matrix element at high $p_\perp$, or by the parton shower or underlying event at low $p_\perp$. The Z $p_\perp$ is important in generator tuning to fix the interplay of ISR and multi-parton interactions (`MPI`) in generating UE activity. The inclusive Z $p_\perp$ is therefore an excellent first test for the generators, before looking at more exclusive Z + jet final states.

We look at three measurements of the Z $p_\perp$: the Run I measurement by CDF, and two Run II measurements by D0, in the electron and muon channels.

Plot from Run I The `RIVET` standard Z $p_\perp$ analysis from CDF Run I [95] is a measurement of the cross section as a function of the transverse momentum of e^+e^- pairs in the Z boson mass region of 66 GeV $< m_{ee} <$ 116 GeV from $p\bar{p}$ collisions at $\sqrt{s}$ = 1.8 TeV, with the measured lepton acceptance extrapolated to 4π with no $p_\perp$ cut. The analysis is also subject to ambiguities in the experimental Z $p_\perp$ definition [95].

Fig. C.1 shows that the MC description in the region observed by the CDF detector in Run I, the MC description for both `HERWIG` $++$ Z NLO generation in `POWHEG` formalism and `SHERPA` Z+3 jets in the PS+ME formalism agree with CDF data, inside the experimental uncertainties, except for the low Z $p_\perp$ region for `HERWIG` $++$.

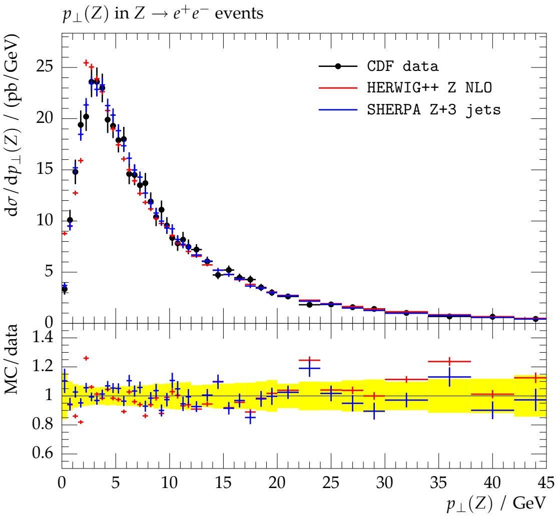

Figure C.1: Z $p_\perp$ analysis for Tevatron Run I. The yellow band in the ratio plot correspond to the uncertainty of the data.

Plots from RunII The D0 Z ($\to e^+e^-$) $p_\perp$ analysis [96] is based on $p\bar{p}$ collisions at $\sqrt{s}$ = 1.96 TeV, with a looser lepton pair mass cut of 40 $< m_{ee} <$ 200 GeV. The measured differential spectrum is normalized to the total Z cross section, to reduce overall systematics uncertainties. The electrons were measured in $|\eta| < 1.1$ or $1.5 < |\eta| < 2.5$, with $p_\perp > 25$ GeV. The result was extrapolated to 4π with no $p_\perp$ cut.

We can see in Fig. C.2, in the left, that the D0 analysis in the electron Z decay channel has a systematic behaviour in the region of medium Z $p_\perp$, for both `HERWIG` $++$ Z NLO (`POWHEG` formalism), `HERWIG` $++$ Z LO with ME formalism and `SHERPA` $Z+3$ jets. The NLO plot shows slightly better behaviour in the mid region (30-60 GeV) than the LO with ME corrections, but no significative differences in the low region. The high $p_\perp$ region lacks the statistics to make a detailed comparison.

The middle regions suggests a problem with the formalism used to treat the Monte Carlo, or something in the analysis that could not be reproduced by the Monte Carlo. So, following this reasoning, we took a closer look in a new D0 Z $p_\perp$ analysis [97] in the muon channel. The muons were measured in $|\eta| < 1.7$ and $p_\perp > 15$ GeV. This new analysis has as an important development the definition of the final observable at the level of particles entering the detector, while previous measurements have applied theoretical factors correcting for any undetected final state radiation and from the measured lepton acceptance to full 4π coverage. This approach minimises the dependence on theoretical models, and therefore any biases in comparisons. The differential cross section is normalized to the total Z cross section, to reduce overall systematics uncertainties, as in the electron channel analysis [96].

We can see in Fig. C.2, in the right, that in the muon channel the discrepancy in the medium Z transverse momentum region is gone, and the ratio of MC to data does not show significant systematic discrepancies, with small fluctuations, for both generators. So the Monte Carlo can better reproduce the analysis with the more limited lepton acceptance and without the model dependent corrections. For `HERWIG`$++$ LO without ME corrections, the expected behaviour is to produce less events in the high transverse momentum region, as this is not fully populated by the PS formalism alone.

`PDF` **and** `K_PERP` **choice on** `SHERPA`

For the sake of using the best parameters for the description of Tevatron data, some other parameters were studied in `SHERPA` generator: the impact of the use of different `PDF`s and different values for intrinsic transverse momentum of the beams (`K_PERP_MEAN`) and its gaussian width (`K_PERP_SIGMA`).

The same Z $(\to \mu^+\mu^-)$ $p_\perp$ analysis [97] of the previous section is used, as this shows a better agreement with MC data than the electron channel analysis.

Intrinsic Transverse Momentum of Beams In Fig. C.3, in the left, we show the transverse momentum of the Z boson in Z+3 jets production with different values for the transverse momentum of the beams. We can see that the `K_PERP_MEAN` = 1.4 (the default value is 0.8) and `K_PERP_SIGMA` = 0.8 (default value) shows a better agreement in the low Z $p_\perp$ region.

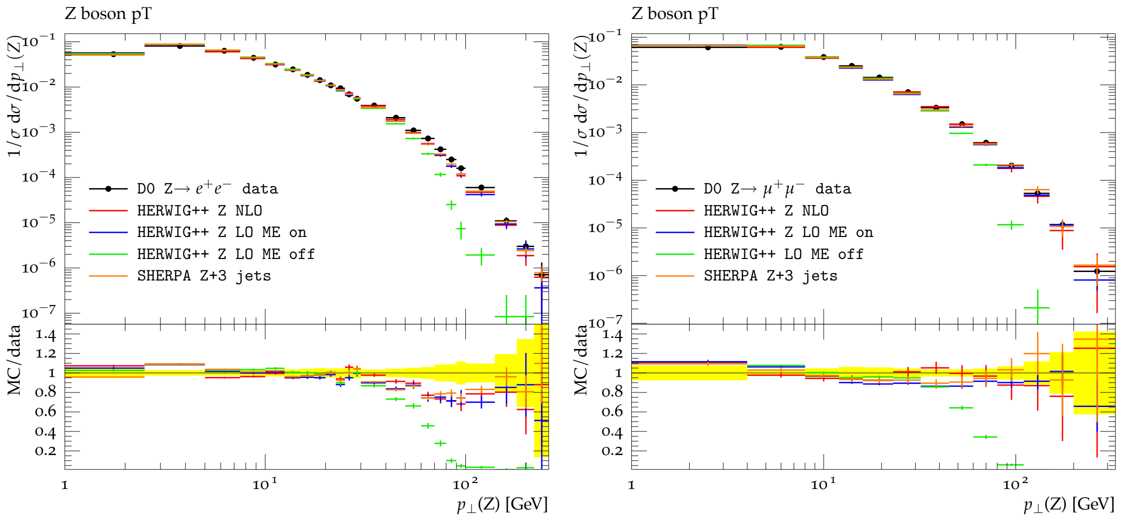

Figure C.2: Comparison of boson transverse momentum for Z production at: NLO `HERWIG` + + (`POWHEG` formalism), LO `HERWIG` + + (ME corrections on and off) and LO `SHERPA` Z + 3 jets, in the $Z \longrightarrow e^+e^-$ channel (left) and $Z \longrightarrow \mu^+\mu^-$ channel (right). Both plots are normalized to the total number of Z events, to reduce systematic uncertainties.

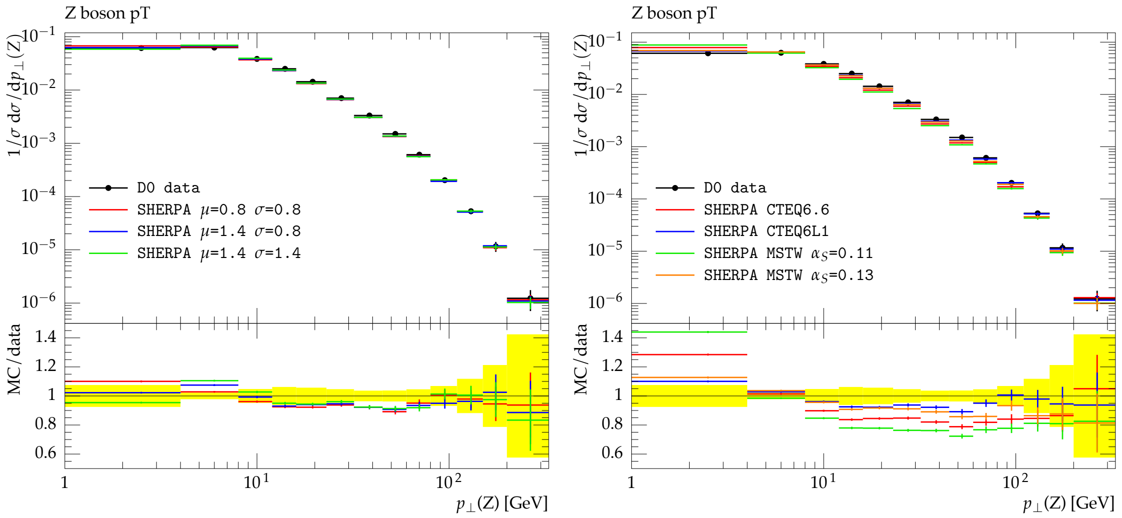

Figure C.3: The Z $p_\perp$ in `SHERPA` for several different parameters of `K_PERP` and its gaussian width (left), using `CTEQ6L1` `PDF`, and for different `PDF`s (right), using default values of `K_PERP` (0.8) and its width (0.8), equivalent to the blue curve on the left graphic. In this plots, no `MPI` model was simulated. The plots are normalized to the total number of Z events, to reduce systematic uncertainties.

`PDF` **Set With Different α_S Values** For showing the impact of changing the `PDF` in the shape of the Z $p_\perp$, the analysis was run with the `MSTW08` [98] set, that is a set of `PDF`s fitted with different values of the strong coupling constant in the Z mass pole, $\alpha_S(M_Z) = 0.11,\ 0.13$. The Fig. C.3 shows the change in the α_S introduces differences in the description. These were compared to other two `PDF`s: the default on `SHERPA`, `CTEQ6.6`, and to `CTEQ6L1`. The last provides a better description of the $Z\ p_\perp$ data, specially in the low transverse momentum region. For `HERWIG` $++$, a NLO PDF is necessary, and all the simulations used the default one, `MRST NLO` [99].

C.4.3 Multiple Parton Interaction

With both generators providing a reasonable description of the $Z\ p_\perp$, we can study the rest of the event in more detail. However, before looking at the jets recoiling against the Z, we must first constrain the other sources of hadronic activity: Multiple Parton Interactions (`MPI`) and the Underlying Event (UE).

Constraining UE/`MPI`

To study the model of the `MPI` in each of the generators used, the CDF underlying event analysis [100] was performed in both `HERWIG` $++$ and `SHERPA` generators.

The analysis was made for Drell-Yan events with $Z/\gamma* \to e^+e^-$ and $Z/\gamma* \to \mu^+\mu^-$. A mass cut $m_{ll} > 70$ GeV and $m_{ll} < 110$ GeV was applied on generator level. The analysis is based on the observation that the hard interaction in an event typically falls along an axis, and activity from `MPI` is completely uncorrelated with this axis. Each event is therefore decomposed into regions in the azimuthal angle, ϕ. The "toward" region defined by the direction of the Z, which is used to set $\phi = 0$. The opposite direction, the "away" region, is then dominated by the recoil to the Z. The "transverse" regions, defined by $60 < \phi < 120$, generally have little activity from the hard interaction, and so are most sensitive to `MPI` and the underlying event. In the analysis, the transverse region is defined for $|\eta| < 1$, and the $p_\perp$ ranges of the leading reconstructed jet is used to divide the data into two samples: "min bias" for $p_\perp < 20$, and "JET20" for $18 < p_\perp < 49$ GeV [100].

Fig. C.4 shows the comparison of `HERWIG` $++$ to CDF data for both using `MPI` model turned on and off . There seem to be a disagreement in the UE observed, with `HERWIG` $++$ always producing less activity than the data in the transverse region. The default settings for the `MPI` model in `HERWIG` $++$ were tuned to provide the best fit to the jet data from Run I and Run II. Adjusting some of these parameters does not yield a significant improvement in the description of the Z data, however [91].

For `SHERPA` generator, the comparisons were for the default settings for the

MPI [101]. Changing PDF to CTEQ6L1, which provided the best description of the $Z\ p_\perp$, significantly degrades the MPI model performance, most probably due to the different value of $\alpha_S\ (M_Z)$ and running of α_s between the two PDF sets. The most important parameter in tuning the MPI model is the scale of the transverse momentum cutoff, and three values are tested with the CTEQ6L1 PDF: 2.1, 2.3 and 2.5 GeV. The plots on Fig. C.5 show that the best parameters for the SHERPA MPI run is the CTEQ6L1 PDF with the scale 2.5.

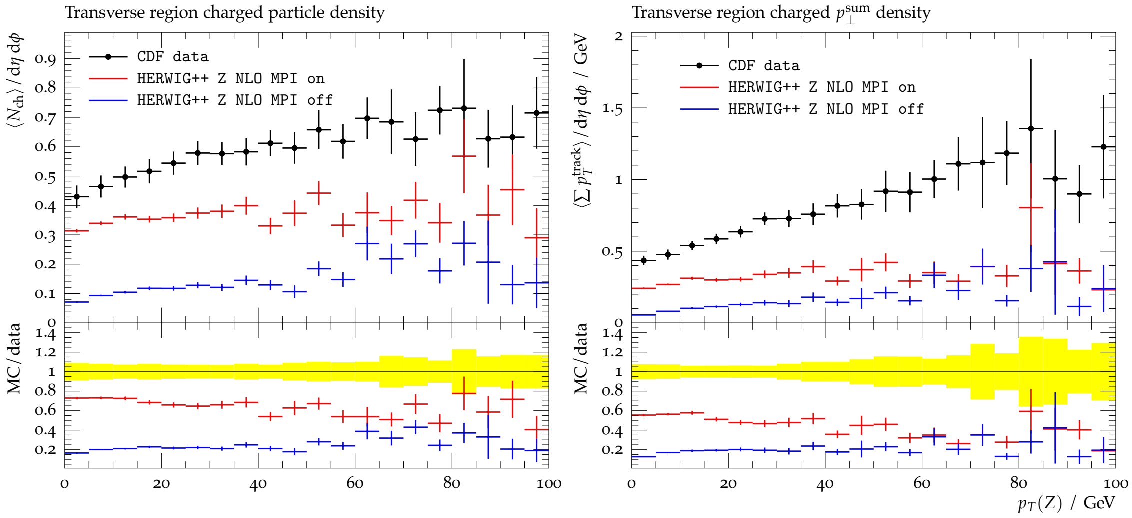

Figure C.4: The transverse region charged particle density (left) and the transverse region charged $p_\perp^{sum}$ density (right) in Underlying Event analysis for HERWIG + + Z NLO with MPI on and off.

C.4.4 *Z* + jets - HERWIG + + and SHERPA LO vs POWHEG NLO

We now return to our main aim: to assess the impact of NLO matrix elements in the simulation of Z (+ jets) events. We use the following generator configurations: LO without ME correction, LO with ME correction and NLO (POWHEG formalism), for HERWIG + + generator; and Z + 3 jets at LO in SHERPA.

The table C.1 shows a comparison of the total Z cross section measured in Tevatron CDF experiment (analysis CDF Z ($\rightarrow e^+e^-$) cross section [102]). The NLO simulation has a better prediction of the cross section, while in LO, HERWIG + + has a better performance than SHERPA generator. Further comparisons between the ME+PS merging in HERWIG + + and SHERPA (besides ALPGEN and PYTHIA) can be found in reference [103].

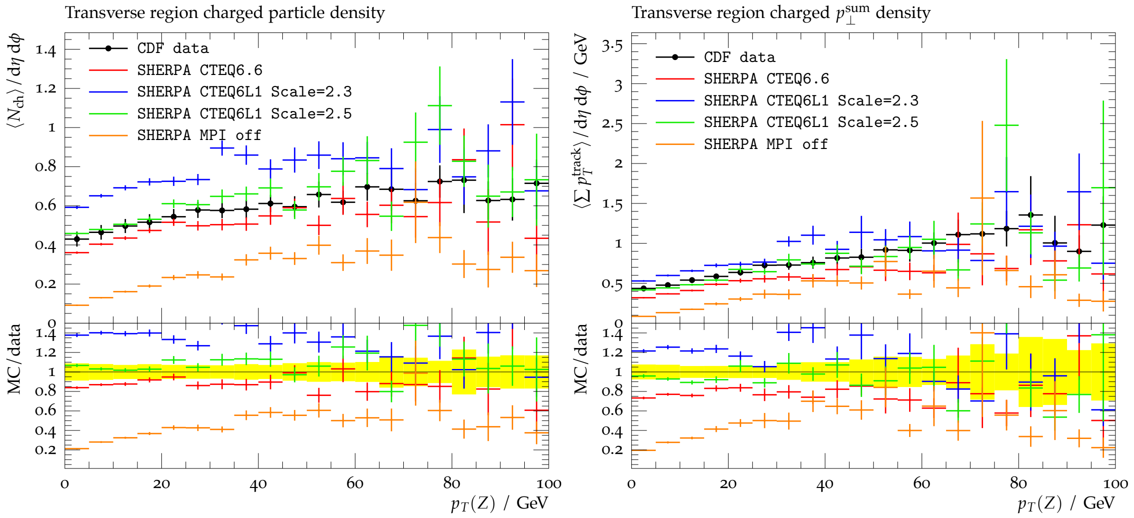

Figure C.5: The transverse region charged particle density (left) and the transverse region charged $p_\perp^{sum}$ density (right) in Underlying Event analysis for `SHERPA` Z + 3 jets with `MPI` on, and different `PDF`s: `CTEQ6.6` with standard `MPI` scale tuning or `CTEQ6L1` with scale parameter equals to 2.1, 2.3 and 2.5 GeV. It also shows the performance when the `MPI` is turned off.

	Total σ_Z [pb]	Uncertainty [pb]
CDF data	256.0	2.1
`HERWIG` + + LO ME on	185.1	0.7
`HERWIG` + + LO ME off	185.2	0.7
`HERWIG` + + NLO	230.4	0.9
`SHERPA` Z + 1 jet	171.5	0.3
`SHERPA` Z + 3 jets	172.6	0.4

Table C.1: The total cross sections for the Z production in data, `SHERPA` and `HERWIG` + + Monte Carlo generators. The parameters for `HERWIG` + + are the default, with `MPI` simulation. For `SHERPA`, `PDF` `CTEQ6L1`, `MPI` with scale 2.5 GeV, and optmized `K_PERP` parameters.

***Z* boson rapidity** The plot on Fig. C.7 top left is from a standard analysis D0 $Z\ (\rightarrow e^+e^-)$ [104], that measures the cross sections as a function of Z boson rapidity. All generator configuration does it in a good way, compatible with the data measurements. The differential cross section is also normalized by the total cross section for Z production.

Jet multiplicity In Fig. C.6 top left, the CDF Z ($\rightarrow e^+e^-$) [98] analysis shows the cross sections as a function of jet multiplicity. The cut on the jet transverse momentum is $p_\perp > 30$ GeV, and in the detector rapidity, $|y_{jet}| < 2.1$. This analysis shows that the cross section for one jet production is well reproduced by the NLO matrix element, but higher jet multiplicities are underestimated. The ME correction improves the number of jets that passes the analysis cuts, so it does better than PS without the ME correction. However, as one can check in the table C.1, the ME correction doesn't affect the Z total cross section, as it is expected. For `SHERPA` Z+3 jets, the addition on LO matrix elements for further emissions, although still makes the bin for the first jet lower than the NLO prediction, is able to predict better the second and the third jets cross sections.

The same analysis was performed, normalizing the plot to the first bin, which is useful to test the relative fraction of two and three jets events, as in Fig. C.6 top right. We can see that, normalizing the first jet cross section to the one found in data, the `SHERPA` Z+3 jets generator can describe, inside data uncertainties, the expected number of events with two and three jets, while `HERWIG` $++$ fails for jet multiplicities higher than one.

The D0 ($\rightarrow e^+e^-$) analysis [105] shows the n-jet cross section ratios (Fig. C.6 down), and is normalized to the total Z cross section (i.e., the bin of zero or more jets). Here we can see that the `HERWIG` $++$ Z NLO prediction for the first jet is according to the data, as well as the prediction for `SHERPA` Z + 3 jets. For higher jet multiplicities, the `SHERPA` Z + 3 jets generator predicts the data with more accuracy, however it still fails for four jets. `HERWIG` $++$ LO with ME corrections does the one jet prediction consistent with data inside uncertainties, but not higher jet multiplicities. When ME corrections are not applied, none of the predictions are good.

Jets transverse momentum and rapidity The standard analysis Z ($\rightarrow e^+e^-$) on D0 [106] measures the differential cross section as a function of the transverse momentum, and normalized to the total cross section of Z production, of the three leading jets in the production of $Z/\gamma* \rightarrow e^+e^- +$jets $+ X$. In Fig. C.7, up left right, and down left and right, there are the comparisons for `HERWIG` $++$ generator in NLO (POWHEG formalism) and in LO with and without ME corrections, and `SHERPA` Z + 3 jets. The LO without ME corrections shows the expected failure of the parton shower alone to populate the high $p_\perp$ region, because it corresponds to the phase space where the PS can't fill properly. When the ME correction is

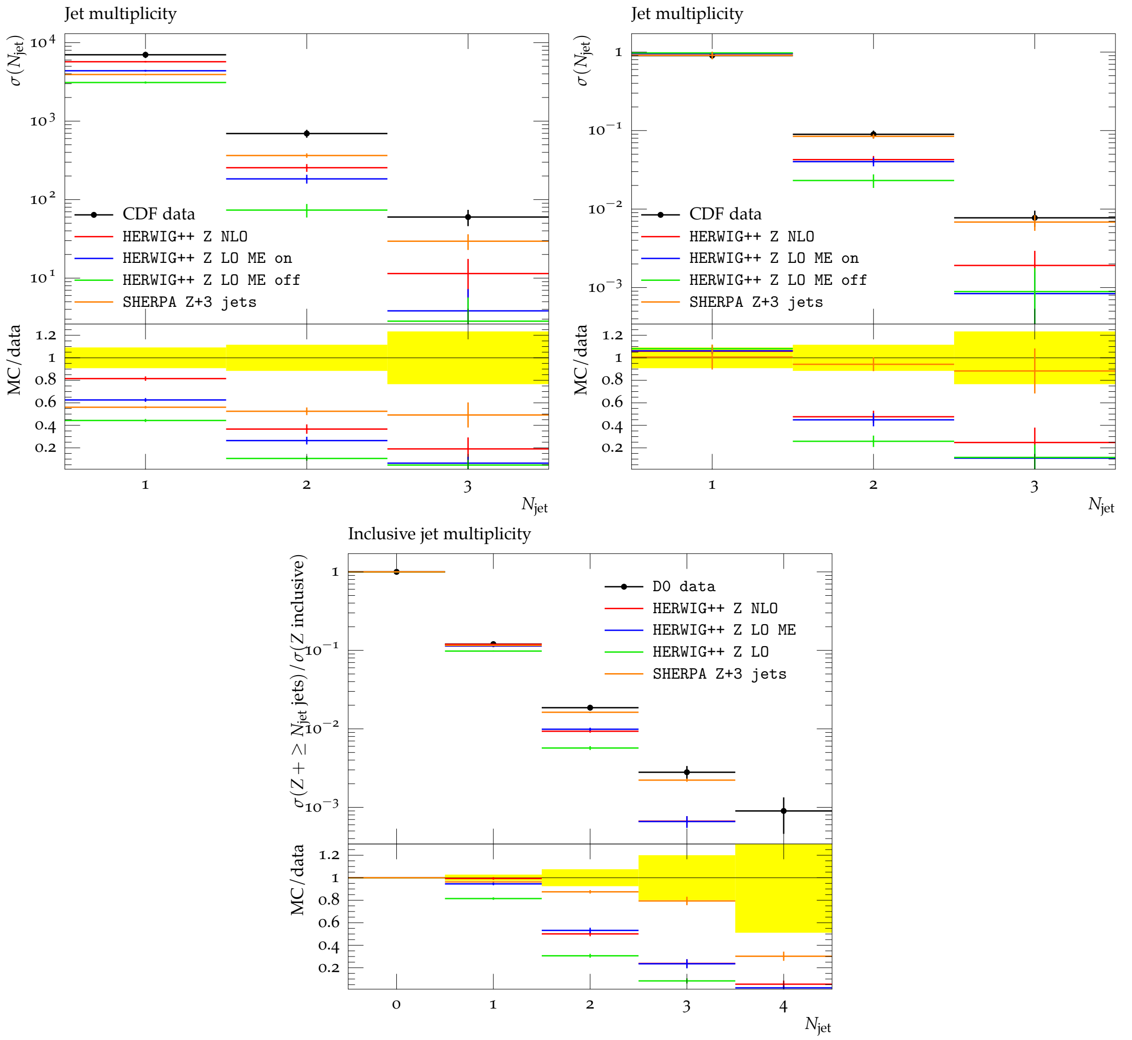

Figure C.6: Comparison plots for Z production at: LO (ME correction off), LO (ME correction on) and NLO, on `HERWIG` + +, and Z+3 jets LO on `SHERPA`. In the top left, the cross section prediction as a function of jet multiplicities. In the top right, the same plot, but normalized to the first bin (the data cross section for one or more jets in the event). The bottom plot shows the ratios of the expected n-jets cross sections to the Z total production cross section (first bin). The parameters for `HERWIG` + + are the defaults, with `MPI` simulation. For `SHERPA`, `PDF CTEQ6L1`, `MPI` with scale 2.5 GeV, and optmized `K_PERP` parameters.

turned on, the effect in correcting the high transverse momentum region can be seen. The behaviour for the NLO plot is more close to the data in higher $p_\perp$ region (above 130 GeV), while it has similar results to LO with ME corrections at lower $p_\perp$. However, for the second and third leading jets, the description is also not good - NLO Z production includes the LO matrix element for one jet production, but the second and third jets are produced only by the parton shower, which again underestimates the data. For the `SHERPA` Z + 3 jets, the matrix element for the further jet emissions allows for a description similar to the NLO curve for the leading jet, and does a greater job for the second and third leading jets. The plots are normalized to the total Z cross section.

D0 Z $\rightarrow \mu^+\mu^-$ Analysis To further study the jet recoil and Z boson $p_\perp$, the standard D0 analysis Z ($\rightarrow$ $\mu^+\mu^-$) + jets [107] was used. It measures the cross sections as a function of the boson momentum, and as a function of momentum and rapidity of the leading jet in Tevatron D0 experiment. This analysis doesn't normalize the data by the Z total cross section production - the shape of the plots are normalized their integral.

As can be seen in Fig. C.8, the cross section in leading jet rapidity is well behaved inside the uncertainties, however `HERWIG` $++$ Z NLO tends to produce a wider distribution. The Z $p_\perp$ shows imprecisions in the low momentum region: for `HERWIG` $++$ Z NLO the production in low Z $p_\perp$ is around 40% lower than data, and in `SHERPA` it's greater than data. This region is particularly sensitive to jets produced by `MPI`, which are not recoiling against the Z boson.

The leading jet $p_\perp$ does not show any discrepancy in both cases, inside the uncertainties. However, a behaviour that is a bit more accentuated in `HERWIG` $++$ Z NLO, is the deficit of events in the Monte Carlo compared to the data in the range of $50 < p_\perp < 120$GeV. The Z $p_\perp$ shows no such deficit (see Fig. C.2), suggesting the MC is not fully describing the hadronic recoil of the Z, and this is studied in detail in the appendix.

The `HERWIG` $++$ LO with ME corrections show similar behaviour than the NLO, and without the ME corrections has a completely different shape in all plots, due to the previously discussed issues in populating the high $p_\perp$ regions.

C.5 LHC Analyses Cuts

After choosing the Monte Carlo parameters for the `HERWIG` $++$ Z NLO (in `POWHEG` formalism) and `SHERPA` Z + 3 jets (LO), comparison plots for $Z \rightarrow e^+e^-$ in the LHC energy (first Run - 7 TeV) were performed, using the following kinematic cuts (taken from [108]):

- Transverse momentum of the lepton $p_\perp(l) > 15$ GeV;
- Absolute value of the lepton pseudorapidity $|\eta(l)| < 2.4$;

- Transverse momentum of the jet $p_\perp(j) > 20$ GeV;
- Absolute value of the jet pseudorapidity $|\eta(j)| < 4.5$;
- Lepton isolation criteria: $\Delta R_{ll} > 0.2$; $\Delta R_{lj} > 0.4$;

The jets are reconstructed with the $antik_T$ clustering algorithm, with cone radius R=0.7. A mass cut on the leptons invariant mass $60 < M_{ll} < 110$ GeV was applied. The events generated correspond to a integrated luminosity of 1 fb^{-1}.

The kinematic variables plotted are shown in Figs. C.9 to C.14: the transverse momentum of the first, second and third leading jets, and the inclusive $p_\perp$ for 1 and 2 or more jets in the event; the transverse momentum of the two leptons used to reconstructed the Z boson, and of the Z; The pseudorapidity of Z and jets; the invariant mass of the Z; the jet multiplicity in the event. All the plots are normalized to their integral, except the jet multiplicity, that is the cross section of production of the event with n-jets.

The Z $p_\perp$ (Fig. C.9 left) shows a discrepancy in the low transverse momentum region: `SHERPA` simulates less events in this region, compared to `HERWIG`$++$. However, for the leading electrons $p_\perp$ of the event (Fig. C.9 center and right), both generators agree inside the Monte Carlo uncertainties.

For the leading jet $p_\perp$ (Fig. C.10 left), the behaviour is the opposite of that from the Z $p_\perp$ - the `SHERPA` generator simulates more events in the low transverse momentum region, and less events in medium and high transverse momentum, although in the later ones it agrees with `HERWIG`$++$ inside the statistical uncertainties. For the second and third leading jets $p_\perp$ (Fig. C.10 center and right), there is good agreement inside MC uncertainties.

The jet inclusive $p_\perp$ for $N_{jet} \geq 1$ and $N_{jet} \geq 2$ (Fig. C.11 left and center, respectively) agree in both generators inside the errors, as well as the invariant mass of the Z boson (Fig. C.11 right).

The pseudorapidity for the Z boson and leading electrons (Fig. C.12) agree for the generators, inside the errors. However, for the leading jets, the behaviour is different: while for the leading jet (Fig. C.13 left) the region in which $|\eta| \leq 3$ is agreed, the region in the range $3 < |\eta| \leq 5$ shows fewer events for the `HERWIG`$++$ generator than for `SHERPA`. For the second leading jet (Fig. C.13 center), `SHERPA` has more events in the central region and fewer events in the range $3 \leq |\eta| \leq 5$. For the third leading jet (Fig. C.13 right), due to high statistical errors, both generators agree in full range. In the jet inclusive η for $N_{jet} \geq 1$ (Fig. C.14 left) the range of

$3 < |\eta| \leq 5$ shows more events for `SHERPA` generator, while for $N_{jet} \geq 2$ (Fig. C.14 center) the generators agree inside errors.

For the cross section as a function of jet multiplicity (Fig. C.14 right), the simulation of Z production at NLO (`POWHEG` formalism) has a greater cross section than `SHERPA` Z+3 jets at LO for the production of one and two jets. However, because `SHERPA` takes into account matrix elements up to 3 jets, the description for higher jet multiplicities have a greater cross section for `SHERPA` generator. The data will always have greater cross sections than the predicted with the generators, because for having equal cross sections one should simulate up to infinite orders of QCD.

C.6 Conclusions

We studied the effects of adding a next to leading order term in the Monte Carlo simulation for Z production in hadron colliders. In addition, the influence of adding a matrix element correction in the leading order calculations for improving the showering in the parton shower formalism, and the influence of some theoretical parameters that enter as input in the Monte Carlo programs.

We could see that the use of the NLO term, studied here in the `POWHEG` formalism as implemented in `HERWIG` $++$ generator, improves the prediction of the cross sections of the processes, as well as the behaviour of the physics observables, specially in the region of higher transverse momentum. The implementation of the matrix element correction in the parton shower formalism also improves the description of the data in the region of high transverse momentum, compared to the calculations in leading order without the correction.

It was also seen that both `SHERPA` ans `HERWIG` $++$ generators show a systematic behaviour lower than the Tevatron data in the region of mid-range transverse momentum of the Z boson. The D0 analysis performed in the muon channel has a better Monte Carlo description than the one performed in the electron channel, and doesn't use any kind of correction based in theory. According to the new muon analysis, if the same theory based corrections are applied, the muon data agree with the electron channel data. So, these theoretical dependent corrections could be responsible for the disagreement and the systematic behaviour between the Monte Carlo and the Tevatron data in mid range transverse momentum of the Z.

The underlying event analysis showed that it is possible to choose a good tune for the parameters in the multiple parton interactions model (Amisic) for the `SHERPA` generator, using the `PDF` that best describes the Z $p_\perp$ data (`CTEQ6L1`). However, for the `HERWIG` $++$ generator, there was no parameter selection that could describe well the underlying event data, and the setup use was the standard one, based in the best description of other physics observables by the authors.

In the analysis of the balance of the Z $p_\perp$ against the leading jet $p_\perp$ and the sum of $p_\perp$ of all jets in the event was possible to see the effects that the `MPI` model make in the region of low transverse momentum.

The analysis for LHC first run energy (7 TeV) shows that some kinematic quantities have a different prediction on `HERWIG` $++$ Z NLO and on `SHERPA` Z+3 jets simulation, such as the low region of the Z boson transverse momentum and leading jet $p_\perp$ and leading jets pseudorapidity in the high absolute value of η range. For the cross section of jet production, the `HERWIG` $++$ Z NLO generator predicts a higher cross section for the first and second jets, while the `SHERPA` Z+3 jets show higher cross sections for higher jet multiplicities. A full comparison once LHC has enough luminosity will show some features that the Monte Carlo generators will have to be able to deal with, implementing in their processes new information that the new data will provide.

Acknowledgements

We would like to thank Frank Siegert, Prof. F. Krauss, Prof. Peter Richardson, for many useful discussions.

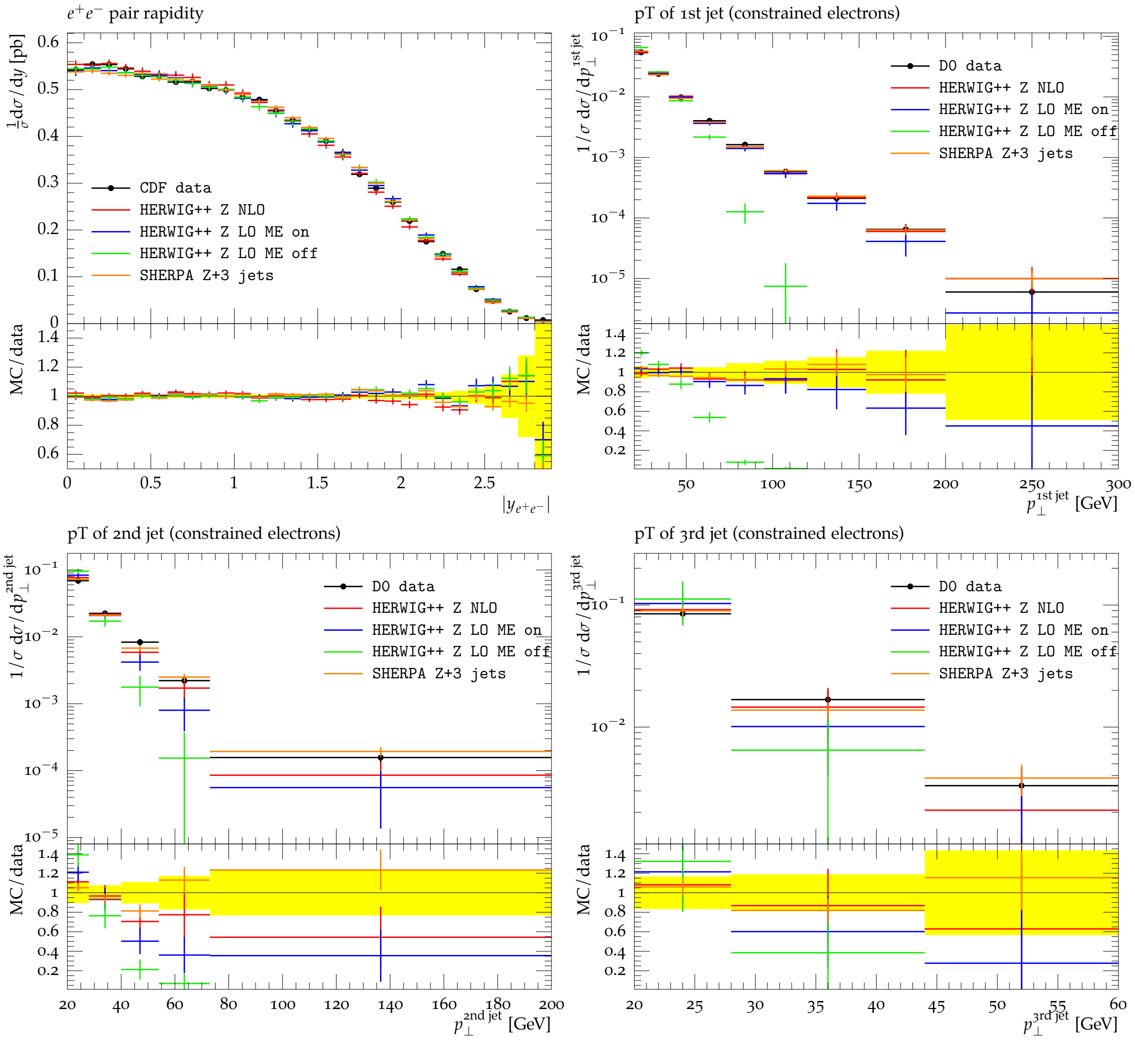

Figure C.7: Comparison plots for Z production at: LO (ME correction off), LO (ME correction on) and NLO, on `HERWIG` $++$, and Z+3 jets LO on `SHERPA`. Up left, the cross section as a function of the Z boson rapidty. Up right and down left and right, the transverse momentum of the leading, second and third leading jet. All the plots are normalized to their integrals. The parameters for `HERWIG` $++$ are the defaults, with `MPI` simulation. For `SHERPA`, `PDF CTEQ6L1`, `MPI` with scale 2.5 GeV, and optmized `K_PERP` parameters.

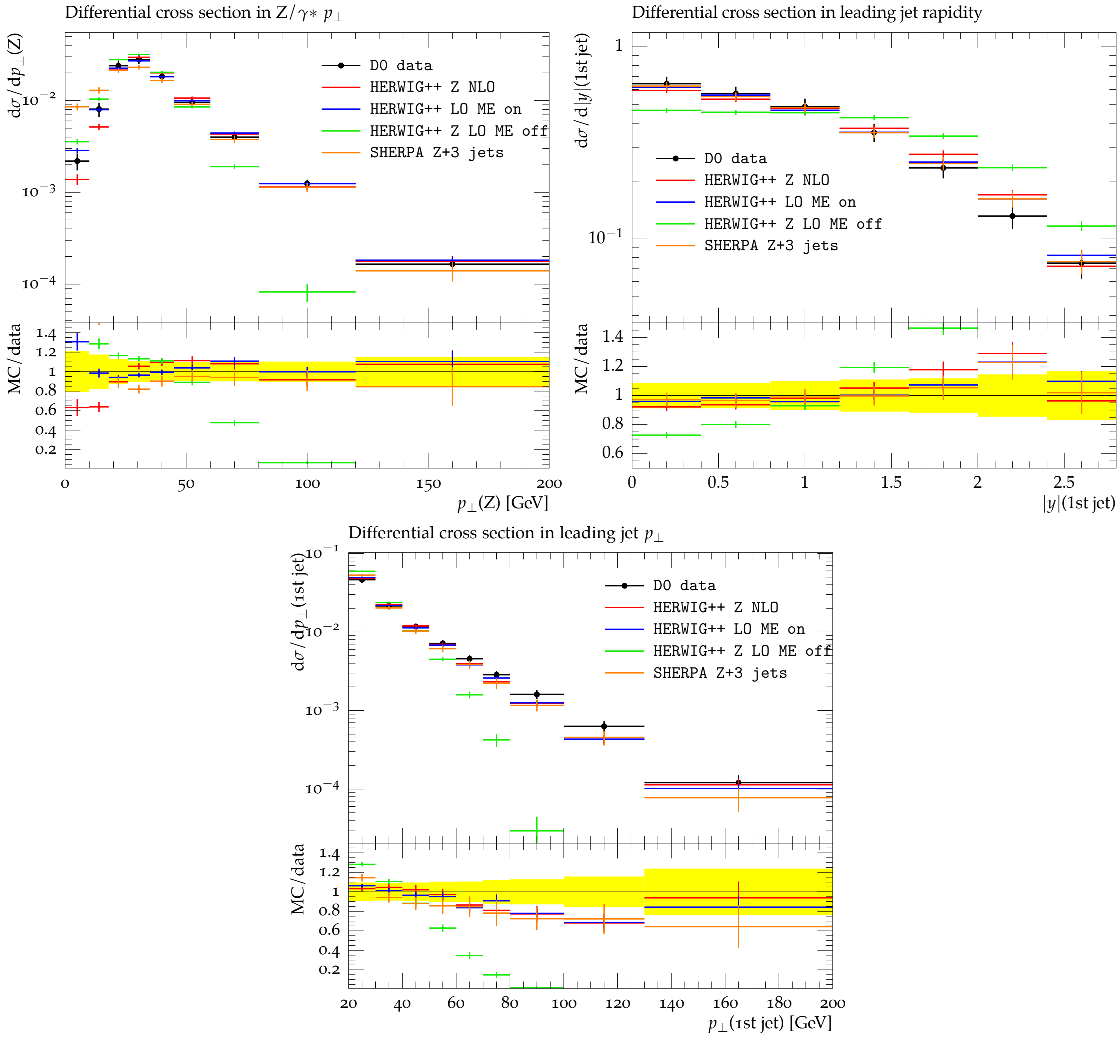

Figure C.8: Comparisons plots for Z production at LO and NLO on `HERWIG` $++$ and LO in `SHERPA` Z+3 jets, in the muon channel: up left, the Z $p_\perp$, up right, the leading jet rapidity, and down, the leading jet $p_\perp$. All plots are normalized to their integrals. For both generators there is the simulation of the `MPI` model. `HERWIG` $++$ has default parameters. `SHERPA` `PDF` is `CTEQ6L1`, scale parameter is 2.5 GeV, and optmized values of `K_PERP`.

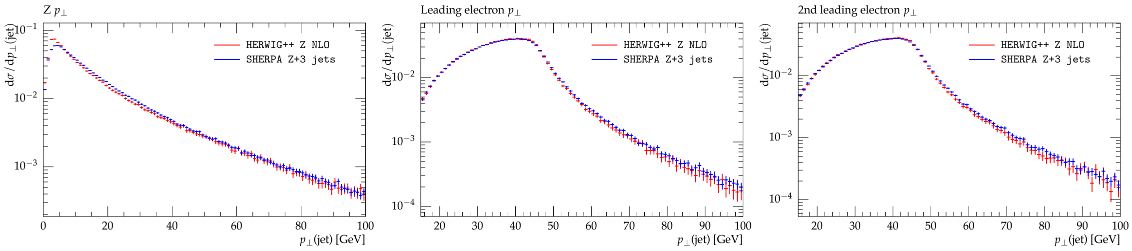

Figure C.9: Comparison plots for LHC (7 TeV) energy, for Z production in electron channel: the Z $p_\perp$ (left), leading electron $p_\perp$ (center) and 2nd leading electron $p_\perp$ (right), for `HERWIG` $++$ Z NLO and `SHERPA` Z+3 jets, both with `MPI` simulation, and `SHERPA` with optimized `K_PERP` and `CTEQ6L1 PDF`, scale parameter 2.5 GeV.

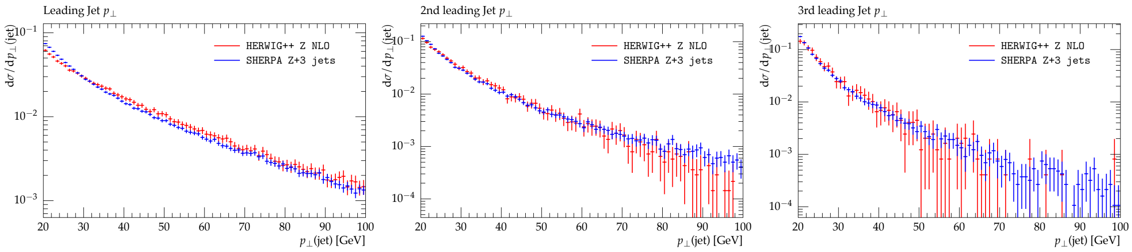

Figure C.10: Comparison plots for LHC (7 TeV) energy, for Z production in electron channel: the leading (left), second (center) and third (right) leading jet $p_\perp$, for `HERWIG` $++$ Z NLO and `SHERPA` Z+3 jets, both with `MPI` simulation, and `SHERPA` with optimized `K_PERP` and `CTEQ6L1 PDF`, scale parameter 2.5 GeV.

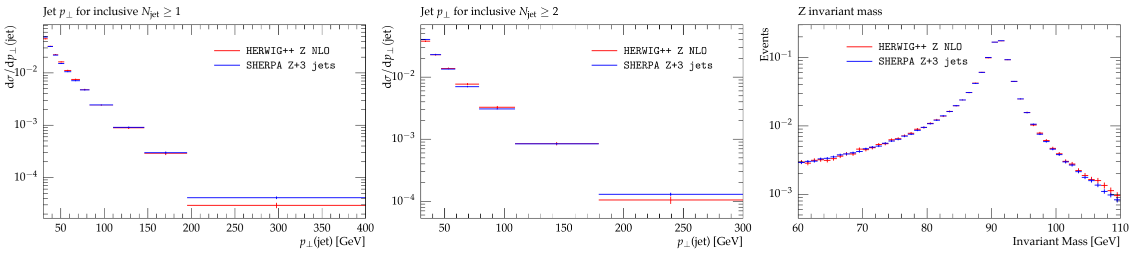

Figure C.11: Comparison plots for LHC (7 TeV) energy, for Z production in electron channel: the jet $p_\perp$ for inclusive $N_{jet} \geq 1$ (left), jet $p_\perp$ for inclusive $N_{jet} \geq 2$ (center) and Z invariant mass (right), for `HERWIG` $++$ Z NLO and `SHERPA` Z+3 jets, both with `MPI` simulation, and `SHERPA` with optimized `K_PERP` and `CTEQ6L1 PDF`, scale parameter 2.5 GeV.

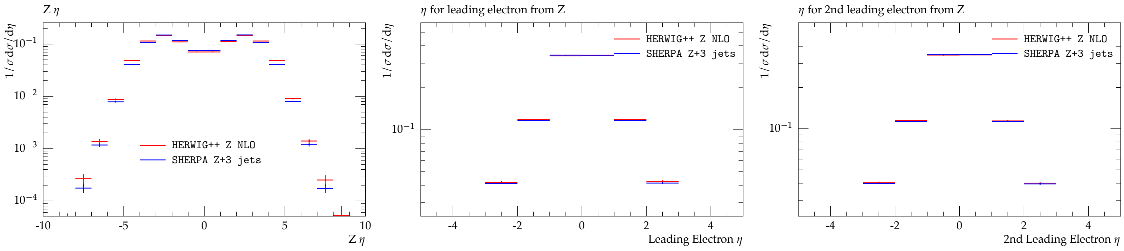

Figure C.12: Comparison plots for LHC (7 TeV) energy, for Z production in electron channel: the Z η (left), leading electron η (center) and 2nd leading electron η (right), for HERWIG++ Z NLO and SHERPA Z+3 jets, both with MPI simulation, and SHERPA with optimized K_PERP and CTEQ6L1 PDF, scale parameter 2.5 GeV.

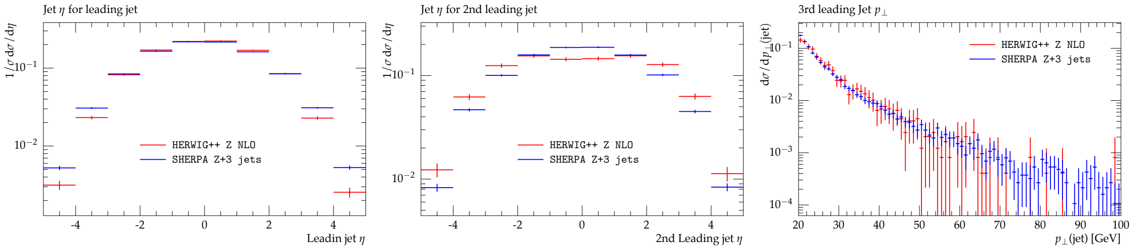

Figure C.13: Comparison plots for LHC (7 TeV) energy, for Z production in electron channel: the leading (left), second (center) and third (right) leading jet η, for HERWIG++ Z NLO and SHERPA Z+3 jets, both with MPI simulation, and SHERPA with optimized K_PERP and CTEQ6L1 PDF, scale parameter 2.5 GeV.

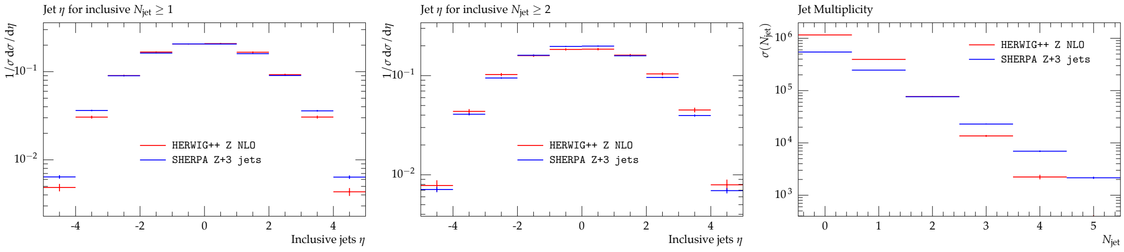

Figure C.14: Comparison plots for LHC (7 TeV) energy, for Z production in electron channel: the jet η for inclusive $N_{jet} \geq 1$ (left), jet η for inclusive $N_{jet} \geq 2$ (center) and jet multiplicity (right), for HERWIG++ Z NLO and SHERPA Z+3 jets, both with MPI simulation, and SHERPA with optimized K_PERP and CTEQ6L1 PDF, scale parameter 2.5 GeV.

Appendix D

Collaboration Services

D.1 Trigger Validation

The trigger system is responsible to decide which events in the hadronic collisions are relevant and should be recorded and stored in the Tier0, to be further processed, reconstructed and made available for analysis by the collaboration members. The decision is based in kinematic characteristics of physics objects (lepton, jets, E_T^{miss}, etc) to separate events with high momentum final states from ordinary QCD events.

As part of my service work for the CMS collaboration, I perform trigger validation for SUSY paths, which purpose is to assure the proper performance of the trigger system in order to avoid losses of interesting events during the collision data taking.

The validation consists of the comparison, for each CMSSW release, of the global efficiency (the ratio of selected events over the total number of simulated events) of each trigger path in the list, using Monte Carlo samples of signal events in the Minimal Supersymmetric Standard Model. Besides the validation reports and discussion of the problematic paths, I also develop and restructure the employed software, to adequate it to the trigger menu for high instantaneous luminosity collisions.

D.2 ALPGEN Monte Carlo Generator

An important contribution given to the CMS Collaboration is the production of Monte Carlo simulated events within the framework of the ALPGEN generator [109]. ALPGEN is a code based on FORTRAN77, used to calculate the matrix elements of $2 \rightarrow N$ processes, which is then combined with general purposes Monte Carlo softwares, such as PYTHIA [59] or HERWIG [110], for the events to undergo hadronization and parton shower. The final events describe accurately some processes observed at the LHC.

Due to the software architecture, the ALPGEN execution in a computational cluster is a hard task. My collaboration service work includes the integration and support of the generator into the CMSSW software, and the collaboration-wide sample production. The Standard Model samples I produced include W+jets, Z+jets, $t\bar{t}$+jets, QCD multijets, W/Z+heavy quarks+jets, γ+jets, totalizing about 2 billion events for each production era I took part on.

D.3 CMS Data Analysis School

The CMS Data Analysis School takes place every year at the LHC Physics Center at Fermilab. It is a workshop which enables CMS physicists beginning analysis to easily join an ongoing analysis in a productive way, by teaching the methods and software framework through a series of tutorials, supervised by more experienced members of the collaboration.

Besides learning, the students also develop their own analyzers, in order to be able to tackle more realistic problems at the tutorial sessions, with a "hands-on" emphasis. I tutored the group in the "Search for new W' bosons" long exercise, leading the students to get to run a state-of-the-art search for new physics with the full collision dataset.

The participation as a tutor in this event is considered important inside the collaboration and formally counts as a service work activity.

D.4 Trigger Shifts

The LHC experiments run 24 hours a day for almost the full year. For this schedule to be possible, every experimental aspect needs monitoring, from the detectors subsystems to the functioning of the computing system. This monitoring is done by the members of the experiment, in a shift schedule. I took part on the CMS "trigger shifts", having as duty to assure the proper performance of both the Level-1 and the High-Level-Trigger systems during data-taking.

Bibliography

[1] S. Weinberg, "Implications of Dynamical Symmetry Breaking", *Phys. Rev. D* **13(4)** (1976) 974, `doi:10.1103/PhysRevD.13.974`.

[2] S. Weinberg, "Implications of Dynamical Symmetry Breaking: An Addendum", *Phys. Rev. D* **19** (1979) 1277, `doi:10.1103/PhysRevD.19.1277`.

[3] L. Susskind, "Dynamics of Spontaneous Symmetry Breaking in the Weinberg-Salam Theory", *Phys. Rev. D* **20** (1979) 2619, `doi:10.1103/PhysRevD.20.2619`.

[4] L. Randall and R. Sundrum, "Large Mass Hierarchy from a Small Extra Dimension", *Phys.Rev.Lett.* **83** (1999) 3370–3373, `doi:10.1103/PhysRevLett.83.3370`, `arXiv:hep-ph/9905221`.

[5] L. Randall and R. Sundrum, "An Alternative to Compactification", *Phys.Rev.Lett.* **83** (1999) 4690–4693, `doi:10.1103/PhysRevLett.83.4690`, `arXiv:hep-th/9906064`.

[6] D. B. Kaplan and H. Georgi, "SU(2) x U(1) Breaking by Vacuum Misalignment", *Phys. Lett. B* **136** (1984) 183, `doi:10.1016/0370-2693(84)91177-8`.

[7] K. Agashe, R. Contino, and A. Pomarol, "The Minimal composite Higgs model", *Nucl. Phys. B* **719** (2005) 165, `doi:10.1016/j.nuclphysb.2005.04.035`, `arXiv:hep-ph/0412089`.

[8] M. Gonzalez-Garcia, O. Eboli, T. Corbett et al., "Constraining anomalous Higgs interactions", (2012). `arXiv:1207.1344`.

[9] R. Contino, D. Marzocca, D. Pappadopulo et al., "On the effect of resonances in composite Higgs phenomenology", *JHEP* **10** (2011) 081, `doi:10.1007/JHEP10(2011)081`, `arXiv:1109.1570`.

[10] E. Eichten and K. Lane, “Low-scale technicolor at the Tevatron and LHC”, *Physics Letters B* **669** (2008), no. 3-4, 235 – 238, `doi:10.1016/j.physletb.2008.09.047`.

[11] E. Eichten, K. Lane, A. Martin et al., “Testing the Technicolor Interpretation of CDF’s Dijet Excess at the LHC”, *FERMILAB-PUB-12-015-T, LAPTH-003-12* (2012) `arXiv:1201.4396`.

[12] CMS Collaboration, “Search for exotic resonances decaying into V+Z using final states with a jet and a lepton pair”, *CMS Physics Analysis Summary* **EXO-11-081** (2012).

[13] CMS Collaboration, “Search for exotic resonances decaying into WZ/ZZ using final states with a jet and a lepton pair or missing transverse energy”, *JHEP* (2012). In preparation.

[14] CMS Collaboration, “The CMS experiment at the CERN LHC”, *JINST* **3** (2008) S08004, `doi:10.1088/1748-0221/3/08/S08004`.

[15] M. L. Mangano, “The super-LHC”, *CERN-PH-TH-2009-164* (2009) `arXiv:0910.0030`.

[16] CMS Collaboration, “CMS Physics Technical Design Report Volume I: Detector Performance and Software”, *CERN-LHCC-2006-021, CMS-TDR-008-2* (2006).

[17] CMS Collaboration, “CMS, tracker technical design report”, *CERN-LHCC-98-06, CMS-TDR-5* (1998).

[18] CMS Collaboration, “CMS: The electromagnetic calorimeter. Technical design report”, *CERN-LHCC-97-33* (1997).

[19] CMS Collaboration, “CMS, the Compact Muon Solenoid. Muon technical design report”, *CERN-LHCC-97-32* (1997).

[20] CMS Collaboration, “CMS. The TriDAS project. Technical design report, vol. 1: The trigger systems”, *CERN-LHCC-2000-038* (2000).

[21] C. Grandi, D. Stickland, L. Taylor et al., “CMS Computing Model”, *CERN-CMS-NOTE-2004-031* (2004).

[22] Particle Data Group Collaboration, “Review of Particle Physics (RPP)”, *Phys.Rev.* **D86** (2012) 010001, doi:10.1103/PhysRevD.86.010001.

[23] F. Englert and R. Brout, “Broken Symmetry and the Mass of Gauge Vector Mesons”, *Phys. Rev. Lett.* **13** (1964) 321–323, doi:10.1103/PhysRevLett.13.321.

[24] P. W. Higgs, “Broken Symmetries and the Masses of Gauge Bosons”, *Phys. Rev. Lett.* **13** (1964) 508–509, doi:10.1103/PhysRevLett.13.508.

[25] G. S. Guralnik, C. R. Hagen, and T. W. B. Kibble, “Global Conservation Laws and Massless Particles”, *Phys. Rev. Lett.* **13** (1964) 585–587, doi:10.1103/PhysRevLett.13.585.

[26] B. W. Lee, C. Quigg, and H. B. Thacker, “Weak interactions at very high energies: The role of the Higgs-boson mass”, *Phys. Rev. D* **16** (1977) 1519–1531, doi:10.1103/PhysRevD.16.1519.

[27] ATLAS Collaboration, “Observation of a new particle in the search for the Standard Model Higgs boson with the ATLAS detector at the LHC”, *Phys.Lett.* **B716** (2012) 1–29, doi:10.1016/j.physletb.2012.08.020, arXiv:1207.7214.

[28] CMS Collaboration, “Observation of a new boson at a mass of 125 GeV with the CMS experiment at the LHC”, *Phys.Lett.* **B716** (2012) 30–61, doi:10.1016/j.physletb.2012.08.021, arXiv:1207.7235.

[29] CDF and D0 Collaboration, “Standard Model Higgs Searches at the Tevatron”, *Int.J.Mod.Phys.* **A27** (2012) 1230023, arXiv:1209.4118.

[30] D. J. Gross and F. Wilczek, “Ultraviolet Behavior of Non-Abelian Gauge Theories”, *Phys. Rev. Lett.* **30** (1973) 1343–1346, doi:10.1103/PhysRevLett.30.1343.

[31] H. D. Politzer, “Reliable Perturbative Results for Strong Interactions?”, *Phys. Rev. Lett.* **30** (1973) 1346–1349, doi:10.1103/PhysRevLett.30.1346.

[32] F. Hasert, S. Kabe, W. Krenz et al., “Observation of neutrino-like interactions without muon or electron in the gargamelle neutrino experiment”, *Physics Letters B* **46** (1973) 138 – 140, doi:10.1016/0370-2693(73)90499-1.

[33] G. Arnison, A. Astbury, B. Aubert et al., "Observation of the muonic decay of the charged intermediate vector boson", *Physics Letters B* **134** (1984) 469 – 476, doi:10.1016/0370-2693(84)91387-X.

[34] G. Arnison, A. Astbury, B. Aubert et al., "Experimental observation of isolated large transverse energy electrons with associated missing energy at $\sqrt{s} = 540$ GeV", *Physics Letters B* **122** (1983) 103 – 116, doi:10.1016/0370-2693(83)91177-2.

[35] G. Arnison, A. Astbury, B. Aubert et al., "Experimental observation of lepton pairs of invariant mass around 95 GeV/c2 at the CERN SPS collider", *Physics Letters B* **126** (1983) 398 – 410, doi:10.1016/0370-2693(83)90188-0.

[36] P. Bagnaia, M. Banner, R. Battiston et al., "Evidence for $Z^0 \rightarrow e^+e^-$ at the CERN anti-p p collider", *Physics Letters B* **129** (1983) 130 – 140, doi:10.1016/0370-2693(83)90744-X.

[37] M. Banner, R. Battiston, P. Bloch et al., "Observation of single isolated electrons of high transverse momentum in events with missing transverse energy at the CERN anti-p p collider", *Physics Letters B* **122** (1983) 476 – 485, doi:10.1016/0370-2693(83)91605-2.

[38] J. R. Ellis, "Testing the standard model and beyond", *CERN-TH-95-317* (1995) arXiv:hep-th/9512133.

[39] ALEPH, DELPHI, L3, OPAL, and SLD Collaborations, LEP Electroweak Working Group, SLD Electroweak Group, SLD Heavy Flavour Group Collaboration, "Precision electroweak measurements on the Z resonance", *Phys.Rept.* **427** (2006) 257–454, doi:10.1016/j.physrep.2005.12.006, arXiv:hep-ex/0509008.

[40] M. Baak, M. Goebel, J. Haller et al., "The Electroweak Fit of the Standard Model after the Discovery of a New Boson at the LHC", *DESY-12-154* (2012) arXiv:1209.2716.

[41] M. Bustamante, L. Cieri, and J. Ellis, "Beyond the Standard Model for Montaneros", *CERN-PH-TH-2009-225* (2009) arXiv:0911.4409.

[42] R. Bousso, “The Cosmological Constant Problem, Dark Energy, and the Landscape of String Theory”, `arXiv:1203.0307`.

[43] WMAP Collaboration Collaboration, “Five-Year Wilkinson Microwave Anisotropy Probe (WMAP) Observations: Likelihoods and Parameters from the WMAP data”, *Astrophys.J.Suppl.* **180** (2009) 306–329, `doi:10.1088/0067-0049/180/2/306`, `arXiv:0803.0586`.

[44] A. Pilaftsis, “The Little Review on Leptogenesis”, *J.Phys.Conf.Ser.* **171** (2009) 012017, `doi:10.1088/1742-6596/171/1/012017`, `arXiv:0904.1182`.

[45] J. H. Gundlach, “Laboratory tests of gravity”, *New Journal of Physics* **7** (2005) 205.

[46] P. Candelas, G. T. Horowitz, A. Strominger et al., “Vacuum configurations for superstrings”, *Nuclear Physics B* **258** (1985), no. 0, 46 – 74, `doi:10.1016/0550-3213(85)90602-9`.

[47] H. Davoudiasl, J. L. Hewett, and T. G. Rizzo, “Phenomenology of the Randall-Sundrum Gauge Hierarchy Model”, *Phys. Rev. Lett.* **84** (2000) 2080, `doi:10.1103/PhysRevLett.84.2080`, `arXiv:hep-ph/9909255`.

[48] W. D. Goldberger and M. B. Wise, “Bulk fields in the Randall-Sundrum compactification scenario”, *Phys.Rev.* **D60** (1999) 107505, `doi:10.1103/PhysRevD.60.107505`, `arXiv:hep-ph/9907218`.

[49] J. Bijnens, P. Eerola, M. Maul et al., “QCD signatures of narrow graviton resonances in hadron colliders”, *Phys.Lett.* **B503** (2001) 341–348, `doi:10.1016/S0370-2693(01)00238-6`, `arXiv:hep-ph/0101316`.

[50] T. Han, J. D. Lykken, and R.-J. Zhang, “On Kaluza-Klein states from large extra dimensions”, *Phys.Rev.* **D59** (1999) 105006, `doi:10.1103/PhysRevD.59.105006`, `arXiv:hep-ph/9811350`.

[51] H. Davoudiasl, J. L. Hewett, and T. G. Rizzo, “Experimental probes of localized gravity: on and off the wall”, *Phys. Rev.* **D63** (2001) 075004, `doi:10.1103/PhysRevD.63.075004`, `arXiv:hep-ph/0006041`.

[52] B. Allanach, K. Odagiri, M. A. Parker et al., "Searching for narrow graviton resonances with the ATLAS detector at the Large Hadron Collider", *JHEP* **0009** (2000) 019, `arXiv:hep-ph/0006114`.

[53] D0 Collaboration, "Search for Randall-Sundrum gravitons in the dielectron and diphoton final states with 5.4 fb^{-1} of data from $p\bar{p}$ collisions at $\sqrt{s}$ =1.96 TeV", *Phys. Rev. Lett.* **104** (2010) 241802, `doi:10.1103/PhysRevLett.104.241802`, `arXiv:1004.1826`.

[54] CDF Collaboration, "Search for Randall-Sundrum gravitons in the diphoton channel at CDF", *Phys. Rev.* **D83** (2011) 011102, `doi:10.1103/PhysRevD.83.011102`, `arXiv:1012.2795`.

[55] ATLAS Collaboration, "Search for dilepton resonances in pp collisions at sqrt(s) = 7 TeV with the ATLAS detector", *Phys.Rev.Lett.* **107** (2011) 272002, `arXiv:1108.1582`.

[56] CMS Collaboration, "Search for signatures of extra dimensions in the diphoton mass spectrum at the Large Hadron Collider", *Phys. Rev. Lett.* **108** (2012) 111801, `doi:10.1103/PhysRevLett.108.111801`, `arXiv:1112.0688`.

[57] K. Agashe, H. Davoudiasl, G. Perez et al., "Warped Gravitons at the LHC and Beyond", *Phys.Rev.* **D76** (2007) 036006, `doi:10.1103/PhysRevD.76.036006`, `arXiv:hep-ph/0701186`.

[58] G. Altarelli, B. Mele, and M. Ruiz-Altaba, "Searching for New Heavy Vector Bosons in p anti-p Colliders", *Z.Phys.* **C45** (1989) 109, `doi:10.1007/BF01556677`.

[59] T. Sjöstrand, S. Mrenna, and P. Z. Skands, "PYTHIA 6.4 Physics and Manual", *JHEP* **05** (2006) 026, `doi:10.1088/1126-6708/2006/05/026`, `arXiv:hep-ph/0603175`.

[60] CMS Collaboration, "Measurement of the Underlying Event Activity at the LHC with $\sqrt{s} = 7$ TeV and Comparison with $\sqrt{s} = 0.9$ TeV", *JHEP* **1109** (2011) 109, `doi:10.1007/JHEP09(2011)109`, `arXiv:1107.0330`.

[61] GEANT4 Collaboration, "GEANT4: A Simulation toolkit", *Nucl. Instrum. Meth.* **A506** (2003) 250–303, `doi:10.1016/S0168-9002(03)01368-8`.

[62] M. Kumar, P. Mathews, V. Ravindran et al., "Diphoton signals in theories with large extra dimensions to NLO QCD at hadron colliders", *Physics Letters B* **672** (2009) 45, `doi:10.1016/j.physletb.2009.01.002`.

[63] M. Kumar, P. Mathews, V. Ravindran et al., "Direct photon pair production at the LHC to in TeV scale gravity models", *Nucl. Phys. B* **818** (2009) 28, `doi:10.1016/j.nuclphysb.2009.03.022`.

[64] R. Gavin, Y. Li, F. Petriello et al., "FEWZ 2.0: A code for hadronic Z production at next-to-next-to-leading order", *Comput. Phys. Commun.* **182** (2011) 2388, `doi:10.1016/j.cpc.2011.06.008`, `arXiv:1011.3540`.

[65] J. Alwall et al., "MadGraph/MadEvent v4: the new web generation", *JHEP* **09** (2007) 028, `doi:10.1088/1126-6708/2007/09/028`, `arXiv:0706.2334v1`.

[66] M. Herquet and F. Maltoni, "MadGraph/MadEvent : A multipurpose event generator", *Nucl.Phys.Proc.Suppl.* **179-180** (2008) 211–217, `doi:10.1016/j.nuclphysbps.2008.07.026`.

[67] J. Pumplin, D. R. Stump, J. Huston et al., "New Generation of Parton Distributions with Uncertainties from Global QCD Analysis", *Journal of High Energy Physics* **2002** (2002) 012.

[68] M. L. Mangano, M. Moretti, F. Piccinini et al., "Matching matrix elements and shower evolution for top-quark production in hadronic collisions", *JHEP* **0701** (2007) 013, `doi:10.1088/1126-6708/2007/01/013`, `arXiv:hep-ph/0611129`.

[69] CMS Collaboration, "Performance of muon identification in 2010 data", *CMS Physics Analysis Summary* **CMS-PAS-MUO-10-004** (2011).

[70] W. Adam, R. Fruhwirth, A. Strandlie et al., "Reconstruction of electrons with the Gaussian-sum filter in the CMS tracker at LHC", *ECONF* **C0303241** (2003) TULT009, `doi:10.1088/0954-3899/31/9/N01`, `arXiv:physics/0306087`.

[71] M. Cacciari and G. P. Salam, "Pileup subtraction using jet areas", *Phys. Lett.* **B659** (2008) 119–126, `doi:10.1016/j.physletb.2007.09.077`.

[72] M. Cacciari, G. P. Salam, and G. Soyez, "The Catchment Area of Jets", *JHEP* **04** (2008) 005, `doi:10.1088/1126-6708/2008/04/005`.

[73] CMS Collaboration, "Particle-Flow Event Reconstruction in CMS and Performance for Jets, Taus, and MET", *CMS Physics Analysis Summary* **CMS-PAS-PFT-09-001** (2009).

[74] M. Cacciari, G. P. Salam, and G. Soyez, "The Anti-k(t) jet clustering algorithm", *JHEP* **04** (2008) 063, `doi:10.1088/1126-6708/2008/04/063`, `arXiv:0802.1189`.

[75] M. Cacciari and G. P. Salam, "Dispelling the N^3 myth for the k_t jet-finder", *Phys.Lett.* **B641** (2006) 57–61, `doi:10.1016/j.physletb.2006.08.037`, `arXiv:hep-ph/0512210`.

[76] M. Cacciari, G. P. Salam, and G. Soyez, "FastJet user manual", *Eur.Phys.J.* **C72** (2012) 1896, `arXiv:1111.6097`.

[77] CMS Collaboration, "Search for Randall-Sundrum Gravitons Decaying into a Jet plus Missing $\mathrm{E_T}$ at CMS", *CMS EXO-AN-11-061* (2011).

[78] CMS Collaboration, "Search for New Physics in the Dijet Mass Spectrum", *CMS EXO-AN-11-094* (2011).

[79] CMS Collaboration, "Search for H → 2l 2jet", *CMS HIG-AN-11-017* (2011).

[80] CMS Collaboration, "Absolute Calibration of Luminosity Measurement at CMS: Winter 2012 Update", *CMS Physics Analysis Summary* **CMS-PAS-SMP-12-008** (2012).

[81] M. R. Whalley, D. Bourilkov, and R. C. Group, "The Les Houches Accord PDFs (LHAPDF) and Lhaglue", *HEP-PH/0508110* (2005) `arXiv:hep-ph/0508110`.

[82] M. Botje et al., "The PDF4LHC Working Group Interim Recommendations", `arXiv:1101.0538`.

[83] CMS Collaboration, "PDF Uncertainties and K-factor for the W' search", *CMS AN-11-273* (2011).

[84] CMS Collaboration, "Measurements of Inclusive W and Z Cross Sections in pp collisions at $\sqrt{s} = 7$ TeV", *JHEP* **2011** (2011) 80, `doi:10.1007/JHEP01(2011)080`, `arXiv:1012.2466`.

[85] A. L. Read, "Presentation of search results: The CL(s) technique", *J. Phys.* **G28** (2002) 2693–2704, `doi:10.1088/0954-3899/28/10/313`.

[86] T. Junk, "Confidence level computation for combining searches with small statistics", *Nuclear Instruments and Methods in Physics Research Section A: Accelerators, Spectrometers, Detectors and Associated Equipment* **434** (1999) 435 – 443, `doi:10.1016/S0168-9002(99)00498-2`.

[87] CMS Collaboration, "Search for W' (or techni-rho) to WZ", *CMS Physics Analysis Summary* **CMS-PAS-EXO-11-041** (2011).

[88] CMS Collaboration, "Search for anomalous t t-bar production in the highly-boosted all-hadronic final state", *JHEP* **1209** (2012) 029, `doi:10.1007/JHEP09(2012)029`, `arXiv:1204.2488`.

[89] S. Hoeche, F. Krauss, S. Schumann et al., "QCD matrix elements and truncated showers", *JHEP* **0905** (2009) 053, `doi:10.1088/1126-6708/2009/05/053`, `arXiv:0903.1219`.

[90] T. Gleisberg, S. Hoeche, F. Krauss et al., "Event generation with SHERPA 1.1", *JHEP* **0902** (2009) 007, `doi:10.1088/1126-6708/2009/02/007`, `arXiv:0811.4622`.

[91] M. Bahr, S. Gieseke, M. Gigg et al., "Herwig++ Physics and Manual", *Eur.Phys.J.* **C58** (2008) 639–707, `doi:10.1140/epjc/s10052-008-0798-9`, `arXiv:0803.0883`.

[92] M. H. Seymour, "Matrix element corrections to parton shower algorithms", *Comput.Phys.Commun.* **90** (1995) 95–101, `doi:10.1016/0010-4655(95)00064-M`, `arXiv:hep-ph/9410414`.

[93] S. Frixione, P. Nason, and C. Oleari, "Matching NLO QCD computations with Parton Shower simulations: the POWHEG method", *JHEP* **0711** (2007) 070, `doi:10.1088/1126-6708/2007/11/070`, `arXiv:0709.2092`.

[94] A. Buckley, J. Butterworth, L. Lonnblad et al., "Rivet user manual", `arXiv:1003.0694`.

[95] CDF Collaboration Collaboration, "The transverse momentum and total cross section of e^+e^- pairs in the Z boson region from $p\bar{p}$ collisions at $\sqrt{s} = 1.8$ TeV", *Phys.Rev.Lett.* **84** (2000) 845–850, `doi:10.1103/PhysRevLett.84.845`, `arXiv:hep-ex/0001021`.

[96] D0 Collaboration Collaboration, "Measurement of the shape of the boson transverse momentum distribution in $p\bar{p} \to Z/\gamma^* \to e^+e^- + X$ events produced at $\sqrt{s}$=1.96-TeV", *Phys.Rev.Lett.* **100** (2008) 102002, `doi:10.1103/PhysRevLett.100.102002`, `arXiv:0712.0803`.

[97] D0 Collaboration Collaboration, "Measurement of the normalized $Z/\gamma^* \to \mu^+\mu^-$ transverse momentum distribution in $p\bar{p}$ collisions at $\sqrt{s} = 1.96$ TeV", *Phys.Lett.* **B693** (2010) 522–530, `doi:10.1016/j.physletb.2010.09.012`, `arXiv:1006.0618`.

[98] A. Martin, W. Stirling, R. Thorne et al., "Parton distributions for the LHC", *Eur.Phys.J.* **C63** (2009) 189–285, `doi:10.1140/epjc/s10052-009-1072-5`, `arXiv:0901.0002`.

[99] A. Martin, R. Roberts, W. Stirling et al., "Physical gluons and high E(T) jets", *Phys.Lett.* **B604** (2004) 61–68, `doi:10.1016/j.physletb.2004.10.040`, `arXiv:hep-ph/0410230`.

[100] CDF Collaboration, "Charged jet evolution and the underlying event in proton-antiproton collisions at 1.8 TeV", *Phys. Rev. D* **65** (2002) 092002, `doi:10.1103/PhysRevD.65.092002`.

[101] T. Sjöstrand and M. van Zijl, "A multiple-interaction model for the event structure in hadron collisions", *Phys. Rev. D* **36** (1987) 2019–2041, `doi:10.1103/PhysRevD.36.2019`.

[102] CDF Collaboration Collaboration, "Measurement of $d\sigma/dy$ of Drell-Yan e^+e^- pairs in the Z Mass Region from $p\bar{p}$ Collisions at $\sqrt{s} = 1.96$ TeV", *Phys.Lett.* **B692** (2010) 232–239, `doi:10.1016/j.physletb.2010.06.043`, `arXiv:0908.3914`.

[103] P. Lenzi and J. Butterworth, "A Study on Matrix Element corrections in inclusive Z/ gamma* production at LHC as implemented in PYTHIA,

HERWIG, ALPGEN and SHERPA", *MCNET-09-06* (2009) arXiv:0903.3918.

[104] D0 Collaboration Collaboration, "Measurement of the shape of the boson rapidity distribution for $p\bar{p} \to Z/gamma^* \to e^+e^- + X$ events produced at $\sqrt{s}$ of 1.96-TeV", *Phys.Rev.* **D76** (2007) 012003, doi:10.1103/PhysRevD.76.012003, arXiv:hep-ex/0702025.

[105] D0 Collaboration Collaboration, "Measurement of the ratios of the Z/gamma* + n jet production cross sections to the total inclusive Z/gamma* cross section in p anti-p collisions at s**(1/2) = 1.96-TeV", *Phys.Lett.* **B658** (2008) 112–119, doi:10.1016/j.physletb.2007.10.046, arXiv:hep-ex/0608052.

[106] D0 Collaboration Collaboration, "Measurements of differential cross sections of Z/gamma*+jets+X events in proton anti-proton collisions at s**(1/2) = 1.96-TeV", *Phys.Lett.* **B678** (2009) 45–54, doi:10.1016/j.physletb.2009.05.058, arXiv:0903.1748.

[107] D0 Collaboration Collaboration, "Measurement of differential Z/γ^* + jet + X cross sections in $p\bar{p}$ collisions at $\sqrt{s}$ = 1.96-TeV", *Phys.Lett.* **B669** (2008) 278–286, doi:10.1016/j.physletb.2008.09.060, arXiv:0808.1296.

[108] J. M. Campbell, R. K. Ellis, and D. L. Rainwater, "Next-to-leading order QCD predictions for W + 2 jet and Z + 2 jet production at the CERN LHC", *Phys.Rev.* **D68** (2003) 094021, doi:10.1103/PhysRevD.68.094021, arXiv:hep-ph/0308195.

[109] M. L. Mangano, M. Moretti, F. Piccinini et al., "ALPGEN, a generator for hard multiparton processes in hadronic collisions", *JHEP* **07** (2003) 001, arXiv:hep-ph/0206293.

[110] M. Bahr, S. Gieseke, M. A. Gigg et al., "Herwig++ Physics and Manual", *Eur. Phys. J.* **C58** (2008) 639–707, doi:10.1140/epjc/s10052-008-0798-9, arXiv:0803.0883.